Synthesis of PdO-USPION via Spark Ablation: For Thermal Ablation and Contrast Enhancement

Meghana Amaregouda

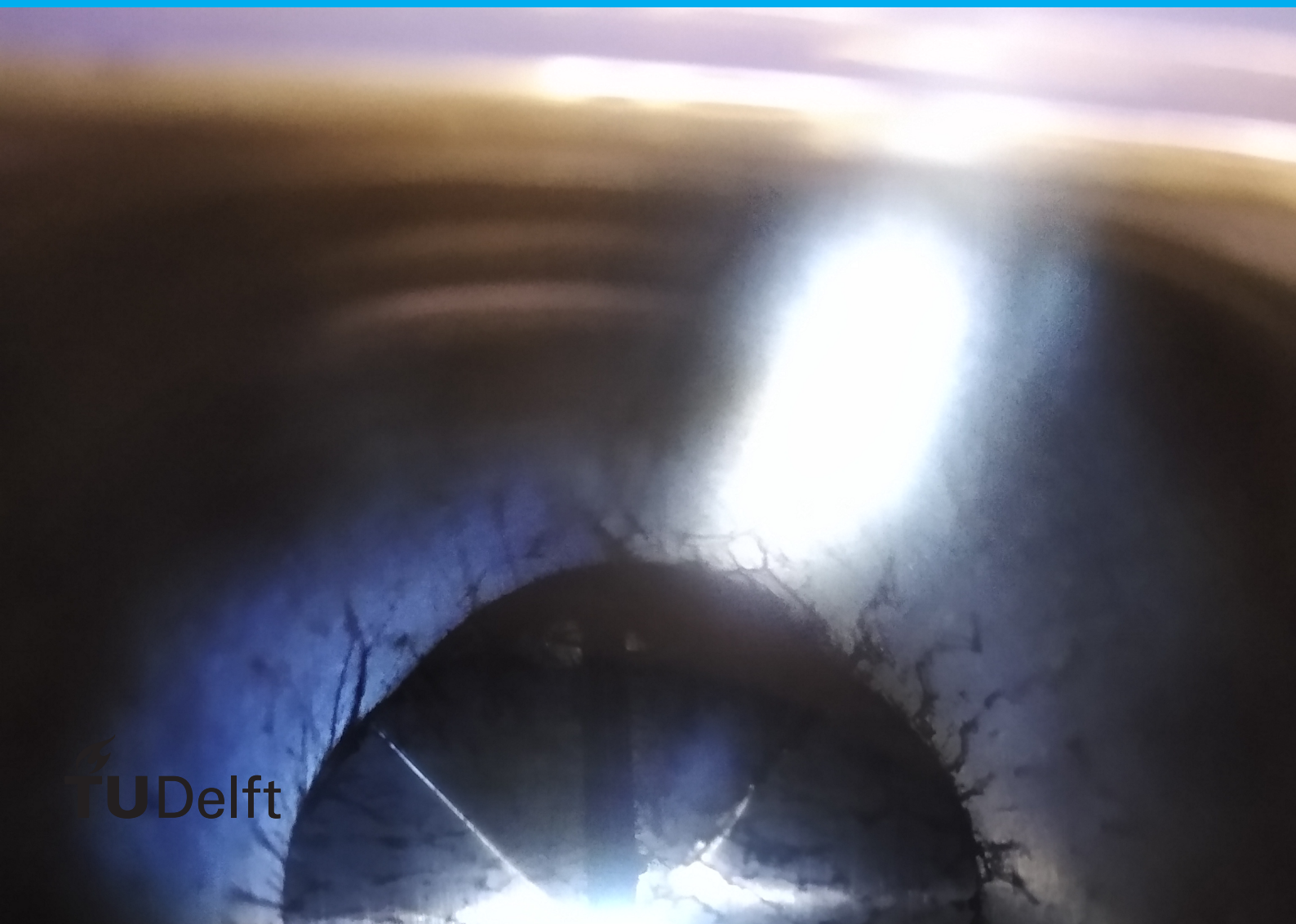

TU Delft

Synthesis of PdO-USPION via Spark Ablation: For Thermal Ablation and Contrast Enhancement

by

Meghana Amaregouda

to obtain the degree of Master of Science
at the Delft University of Technology,
to be defended publicly on Monday January 26, 2021 at 1:00 pm.

Student number:	4851889	
Project duration:	February, 2020– January, 2021	
Thesis Supervisor:	Dr. Kristina Djanashvili	TU Delft
Thesis committee:	Dr. Kristina Djanashvili	TU Delft
	Dr. Antonia Denkova	TU Delft
	Dr. Bert Wolterbeek	TU Delft

This thesis is confidential and cannot be made public until January 23, 2023.

TU Delft

Abstract

Conventional early-stage breast cancer treatments such as surgery, chemotherapy and external radiotherapy despite their proven short-term efficacy tend to have adverse long-term physiological and psychological implications on the patients. This is primarily due to their inability to spare healthy tissue surrounding the tumor. Use of radioactive palladium (^{103}Pd) seeds for producing localized effect with brachytherapy is already in practice. However, they are known to result in uneven dose distribution with creation of "hot spots" in the vicinity of seed implants. Alternatively, conventional thermal ablation or hyperthermia treatments using mechanical or electromagnetic systems also have difficulties with localizing the thermal effect to the target region. Composite and biocompatible palladium- (Ultra-small) superparamagnetic iron oxide nanoparticles (PdO-USPION) on the other hand have the potential to diffuse throughout the tumor ensuring relatively more uniform dose distribution and improve the ease of clearance from the biological system without causing long-term side effects. Magnetic property of (Ultra-small) superparamagnetic iron oxide nanoparticles can be exploited to induce and deliver heat energy to kill cancerous cells upon exposure to Alternating magnetic field (AMF) and generate contrast enhanced magnetic resonance images (MRI) by subjecting them to static magnetic fields.

Heating and contrast enhancement ability depends on the physical, chemical and magnetic properties of nanoparticles which in turn rely on the synthesis method. In this research, spark ablation technology is employed to produce the nanoparticles from metallic electrodes. Although, for the purpose of the current research, inactive palladium is used to reduce complexity given that the synthesis of PdO-USPIONs with this synthesis method is employed for the first time through this research. Inter-metallic Pd-Fe are generated in the spark discharge system and captured in an aqueous media resulting in (oxidised intermetallic palladium-ultrasmall superparamagnetic iron oxide nanoaprticles) PdO-USPIONs. Since the synthesis method is relatively new, major component of the research deals with investigating the influence of system parameters on production of nanoparticles. Characterization results associated with USPIONs and PdO-USPIONs are thoroughly analyzed to optimize the setup to generate tunable PdO-USPIONs and to evaluate their performance as thermal and contrast agents. Use of citric acid as surfactant to lower agglomeration resulting in improved T_1 relaxation behavior is also studied.

Acknowledgements

This master thesis marks the completion of my Master study in Biomedical Engineering at Delft University of Technology. The project was completed within Applied Radiation and Isotopes (ARI) research group of the Radiation, Science and Technology department at Reactor Institute Delft and in collaboration with VS Particle, Delft.

First of all, I would like to thank my supervisor Kristina Djanashvili for giving me the opportunity to work on this interesting thesis. I gained new skills and invaluable knowledge because of this research. I am extremely grateful to Kristina for her immense patience and guidance that she offered through both good and bad phases of the project. I would like to express my gratitude to professor Antonia for her excellent recommendations during my thesis that helped me understand some of the problems associated with the system from a different perspective. I would also like to thank Rogier for providing training on VS Particle generator, for all his suggestions and helping me with heating measurements. I would like to express my appreciation to Alexandra for taking time out of her doctoral work to perform TEM images and with whom I could always discuss my doubts. I had the best learning experience working alongside Thijs on VSP particle system. I am grateful for all the brainstorming sessions we had. I would like to particularly thank Astrid for running back and forth countless number of times with me to get DLS measurements, TEM and SEM imaging done. I would like to thank Baukje for ICP measurements, Stephen for NMR measurements, Iulian for Mossbauer spectroscopy, Robert for XRD and Anton for Magnetization measurements. A huge shout out to the most helpful and cordial research group who made it easy even with all the hurdles due to pandemic and to which I consider myself to be lucky having been a part of. Also, I would like to thank Wilbert and Bernardus from VS Particle for their quick responses in case of issues with VSP-G1 generator and for all the meetings we had to gain better understanding of the system and particles.

I would like to thank all my cousins and friends for being the support system I could fall back onto. Finally, I am blessed and eternally indebted to have parents who never stopped believing in me and sacrificed all they have to be where I am today. I dedicate my work and degree to them.

Meghana Amaregouda
Delft, January 2021

Contents

List of Figures ix

List of Tables xiii

1 Introduction 1
1.1 Research Question . . . 2

2 Background 3
2.1 Background on Spark Discharge Generation . . . 3
2.1.1 Synthesis . . . 3
2.1.2 Nanoparticle Formation Mechanism . . . 4
2.1.3 Factors influencing Nanoparticle formation . . . 6
2.1.4 Generation of Composite Nanoparticles . . . 10
2.1.5 Nanoparticle capture in solution . . . 11
2.2 Background in Magnetism . . . 12
2.2.1 Superparamagnetism . . . 12
2.3 Magnetic Nanoparticle Heating Mechanism . . . 13
2.3.1 Relaxation Loss . . . 13
2.3.2 Factors influencing MNP heating . . . 14
2.4 Magnetic Resonance Imaging . . . 16
2.4.1 Contrast Agents . . . 17
2.4.2 USPION as T_1 contrast agent . . . 18
2.5 Takeaways . . . 20

3 Generation and Optimization Methods 21
3.1 Experimental Setup . . . 21
3.2 Synthesis of USPION . . . 22
3.2.1 Effect of Isoelectric Point (IEP) and Ultra-sonication . . . 23
3.2.2 Setup-modifications to improve absorption efficiency in bubbling column . . . 26
3.3 Synthesis of PdO . . . 28
3.4 Synthesis of PdO-USPION . . . 29
3.4.1 Addition of citric acid . . . 29

4 Characterization Methods 33
4.1 Morphology . . . 33
4.1.1 Dynamic Light Scattering (DLS) . . . 33
4.1.2 Transmission Electron Microscopy (TEM) . . . 34
4.2 Composition . . . 35
4.2.1 Inductive Coupled Plasma-Optical Emission Spectroscopy (ICP-OES) . . . 35
4.2.2 X-ray Diffraction (XRD) . . . 36
4.2.3 Scanning Electron Microscopy- Energy-Dispersive X-ray spectroscopy (SEM-EDS) . . . 36

4.3 Heating Power measurement . . . 37
4.4 Magnetization . . . 37
4.4.1 Vibrating Sample Magnetometer (VSM) . . . 37
4.4.2 Mössbauer Spectroscopy. . . . 38
4.5 Relaxation Measurements. . . . 38

5 Results and Discussion 41
5.1 Morphology. . . . 41
5.1.1 Dynamic Light Scattering (DLS) . . . 41
5.1.2 Transmission Electron Microscopy (TEM) . . . 42
5.2 Composition . . . 44
5.2.1 Inductive Coupled Plasma-Optical Emission Spectroscopy (ICP-OES) . . . 44
5.2.2 X-ray Diffraction (XRD) . . . 45
5.2.3 Scanning Electron Microscopy- Energy-Dispersive X-ray spectroscopy (SEM-EDS) . . . 45
5.3 Heating Power Measurement . . . 47
5.4 Magnetic Measurements . . . 48
5.4.1 Vibrating Sample Magnetometer (VSM) . . . 48
5.4.2 Relaxation Measurements . . . 49
5.4.3 Mössbauer Spectroscopy. . . . 49

6 Conclusions 53
6.1 Future Work. . . . 55

Bibliography 57

A Calibrations and Calculations 63
A.1 Calibration lines of Fe (All emission wavelengths). . . . 63
A.2 Calibration lines of Pd (All emission wavelengths) . . . 67
A.3 Concentration and pH Calculations of Citric Acid. . . . 69
A.3.1 Citric acid solution for experiment 32 . . . 69
A.3.2 Citric acid solution for experiment 33 . . . 69
A.4 NMR Calculations. . . . 70
A.4.1 Controls . . . 70
A.4.2 Relaxation measurements of E30. . . . 71
A.4.3 Relaxation measurements of E31. . . . 72
A.4.4 Relaxation measurements of E32. . . . 73
A.4.5 Relaxation measurements of E33. . . . 74

List of Figures

2.1 Schematic of a typical Spark Discharge Generator circuit (Modified version of circuit from S Tabrizi et.al., 2012) [7] . . . 4
2.2 Stages of Nanoparticle Formation [13] . . . 4
2.3 Influence of Coalescence, collision and cooling on generation of nanoparticles [20] . . . 5
2.4 Particle morphology evolution during coalescence as a function of temperature[21] . . . 6
2.5 Voltage discharge as a function of time [13] . . . 7
2.6 Nanoparticle yield as a function of energy per spark (C=20nF, d=1 mm, Q=0.8 L/min [Ar gas]) [13] . . . 7
2.7 Energy per spark (left) and Nanoparticle yield (Right) as a function of spark gap (C=20 nF, f_{SRR}=150 Hz, Q=0.8 L/min [Ar gas]) [24] . . . 7
2.8 Size distribution as a function of spark gap (C=5nF, f_{SRR}=10Hz, Q=10 L/min [Ar]) [24] . . . 8
2.9 Nanoparticle production rate as a function of spark frequency (C=20nF, d=1 mm, Q=0.8 L/min [Ar gas]) [13] . . . 8
2.10 Discharge voltage at high spark repetition rate [13] . . . 8
2.11 Nanoparticle size as a function of carrier gas flow rate [24] . . . 9
2.12 Generation of composite nanoparticles with the use of different electrode material [33] . . . 10
2.13 Nanoparticle collection in liquid . . . 11
2.14 (A) Neel Relaxation and (B) Brownian Relaxation [40] . . . 13
2.15 Simulated and experimental SAR values corresponding to SPIONs [42] . . . 15
2.16 Spin disorder distribution based on the shape of the nanopartcles [42] . . . 15
2.17 SAR enhancement with improvement in magnetic anisotropy in accordance with the shape [42] 16
2.18 T1 and T2 relaxation [58] . . . 17
2.19 Difference in T1 and T2 between tissues (Dark blue: tissue 1, Light blue: tissue 2) [60] . . . 17
2.20 Nanoparticle size dependent magnetization curves [63] . . . 19
2.21 (a) T_1 weighted images of 3 nm-sized USION contrast agent. (b) Relaxation rate and corresponding relaxivity vs Fe concentration of iron oxide nanoparticles at varying diameters. (c,d) T1 weighted images of MCF-7 cell pellets containing IONP with sizes of (c) 3 nm and (d) 12 nm (after 24 hour incubation). [63] . . . 19
2.22 T_1 weighted images depicting temporal progression of CA through the body of rat[66] . . . 20

3.1 Experimental Setup (Updated version of setup from Tijn)[67] . . . 21
3.2 Schematic of IONP surface in water[68] . . . 24
3.3 Schematic of Electric Double Layer[70] . . . 25
3.4 Total Electric Potential w.r.t particle separation (DLVO theory)[68] . . . 26
3.5 a) Capture of nanoparticles in metal mesh (Left) b) Low concentration resulting from use of mesh (Right) . . . 27
3.6 Capture of nanoparticles in stacked meshes . . . 27

3.7 Difference in Bubble formation with mesh (Left) and with Bronze tablet (Right) (Reproduced from Striekwold) . . . 27
3.8 Increase in USPION concentration with the use of Bronze porous tablet . . . 28
3.9 Adhesion of Palladium Oxide Nanoparticles to surface of bubbling column . . . 28
3.10 Difference in bubble formation without (Left) and with citric acid (Right) . . . 30
3.11 Highest concentration of CA capped USPION . . . 30
3.12 Variation in surface charge and ζ potential of IONP w.r.t. pH [68] . . . 31
3.13 CA functionalization over PdO-USPION [73] . . . 31
3.14 Difference in NP retention in porous tablet without (Left) and with citric acid (Right) . . . 32

4.1 Schematic of DLS set-up [78] . . . 34
4.2 Schematic of TEM [79] . . . 35
4.3 Schematic of ICP-OES instrument [80] . . . 35
4.4 Schematic of SEM [81] . . . 37
4.5 T1 inversion recovery pulse sequence . . . 38
4.6 CPMG sequence . . . 39

5.1 DLS measurement of a) PdO Nanoparticles (Left) and b) USPION (Right) [V=1.3kV, I=10mA, Q=1L/min] . . . 41
5.2 Agglomeration of USPIONs in 4 days [V=1kV, I=7mA, Q=2L/min] . . . 42
5.3 DLS measurement of a)Naked PdO-USPIONs and b) CA capped PdO-USPIONs [V=1.3kV, I=10mA, Q=1L/min] . . . 42
5.4 Difference in Nanoparticle capture on 400nm filter a) without and b) with CA . . . 42
5.5 TEM image of a) PdO nanoparticles of 4nm (Left) and b) USPION of 5nm (Right) . . . 43
5.6 TEM image of a) Naked PdO-USPION (Left) and b) CA coated PdO-USPION (Right) . . . 43
5.7 Splashed bulk particles a) 263 nm (Left) and b) 175,100,75,25 nm (Right) . . . 44
5.8 Mechanism of Bulk material formation [20] . . . 44
5.9 XRD Measurement of Iron Nanopowder from generator . . . 46
5.10 XRD Measurement of Palladium-Iron Nanopowder from generator . . . 46
5.11 SEM-EDS of Pd) USPION sample . . . 47
5.12 Heating performance of PdO-USPIONs when subjected to AMF . . . 48
5.13 Mass Magnetization of Fe and Pd-Fe Nanoparticles . . . 48
5.14 Mössbauer Measurements . . . 50

A.1 Fe234.349 calibration . . . 63
A.2 Fe234.830 calibration . . . 64
A.3 Fe238.204 calibration . . . 64
A.4 Fe239.562 calibration . . . 65
A.5 Fe259.939 calibration . . . 65
A.6 Fe273.955 calibration . . . 66
A.7 Pd248.892 calibration . . . 67
A.8 Pd324.270 calibration . . . 67
A.9 Pd340.458 calibration . . . 68
A.10 Pd363.470 calibration . . . 68
A.11 T_1 relaxation of water . . . 70
A.12 T_2 relaxation of water . . . 70

A.13 T_1 relaxation of Xanthan 70
A.14 T_2 relaxation of Xanthan 71
A.15 E30-T_1 71
A.16 E30-T_2 71
A.17 E31-T_1 72
A.18 E31-T_2 72
A.19 E32-T_1 73
A.20 E32-T_2 73
A.21 E33-T_1 74
A.22 E33-T_2 74

List of Tables

2.1 Properties of commonly used gases in SDGs [27] 9
2.2 Thermal properties of Palladium and Iron Electrodes [30][31] 10

3.1 Selected Set-points and results of Sharaf's Experiments [34] 22
3.2 Difference in DLS measurement of Un-sonicated and Sonicated sample 24
3.3 ICP results 26

4.1 Characterization Methods 33

5.1 ICP results of PdO-USPION 45
5.2 SEM-EDS measurements of Mass % of Constituent Elements 47
5.3 NMR Measurements 49

1

Introduction

Breast cancer is the most prevalent cancer among women in the world. One in eight women are prone to breast cancer in The Netherlands [1]. Increased awareness among women, access to medical care, frequent screening and progressive technology have enabled the detection of cancer at an early stage. Most commonly employed treatment procedures are surgery, chemotherapy and radiotherapy. Surgical treatments result in scarring and have adverse psychological effects on the patient [2]. Numerous research and clinical studies have shown that chemotherapy or external radiotherapy suffer from low drug/radiation availability, low penetration at target site and difficulty in sparing of healthy tissue surrounding the tumour. Brachytherapy (BT) which involves placing of sealed radioactive seeds at the target site via catheters offer a more localized cancer treatment compared to external therapies and relatively less side effects due to increased probability of sparing normal tissue. However, BT is known to cause radiation "hot spots" in the vicinity of the implant which results in uneven dose distribution in total volume of tumor.

Alternatively, heat treatments such as Thermal ablation and hyperthermia have also been explored. Thermal ablation technique involves the temperature attainment of 50^{o}C or higher that leads to complete cancer cell annihilation in response to heat shock [3]. This treatment procedure has an upper-hand over other conventional methods since it does not exhibit any carcinogenic or scarring issues. Thermoablation however can severely damage healthy tissue if the treatment is not precisely localized. On the other hand, hyperthermia procedure involves elevating cells/tissue temperature in the range of 42-45^{o}C [3]. Unlike thermoablation, hyperthermia does not necessarily always lead to complete cell death. It is particularly used as an add on treatment to conventional therapies. It is reported to improve treatment efficiency of ionizing radiation by increasing oxygen concentration in tumour that causes permanent DNA damage and also aid in higher anticancer drug uptake. Numerous mechanical and electromagnetic strategies have been employed to harness and deliver heat to the tumour but the key drawback of all these approaches is that they do not produce localized effect [4].

In search of a therapeutic method that improves treatment efficiency while simultaneously lowering the possibility of adverse long term toxicity and side effects, researchers of Applied Radiation and Isotopes (ARI) Group at Reactor Institute Delft (RID) turned their attention towards use of magnetic nanoparticles for image-guided thermo -brachytherapy.(Ultra-small)-/Superparamagnetic Iron oxide nanoparticles (U-/SPIONs) or substituted U-/SPIONs have been extensively studied for the application of Thermal ablation/ Hyperthermia and as contrast agents over the past decades. (Substituted) Iron oxide nanoparticles (IONPs) smaller than

25nm have been reported to exhibit superparamagnetism, a magnetic property described in section 2.2.1. IONPs smaller that 10nm are said to be Ultra-small Superparamagnetic Iron Oxide nanoparticles (USPION) [5]. Owing to their superparamagnetic behavior, iron oxide nanoparticles tend to generate heat when exposed to Alternating Magnetic Field (AMF) and serve as contrast agents when exposed to static magnetic field for Magnetic Resonance Imaging (MRI).The magnetic properties and biocompatibility features of these magnetic nanoparticles (MNP) provide an edge for their use in this theranostic application.

Use of ^{103}Pd as permanently implantable radioactive seed to treat breast cancer via brachytherapy is already in practice. However, as mentioned earlier, they result in non-uniform dose distribution [6]. Thus, composite Pd-(U)-/SPIONs which can be injected directly at the tumor site that diffuses within the region ensuring a better penetration and dose distribution along with heating and imaging ability appears to be a right fit for a minimally invasive early-stage breast cancer treatment.

Ability of the Pd-(U)-/SPIONs to function as effective theranostic agents largely depends on their magnetic, chemical and morphological properties which in turn are dictated by the method of synthesis. Various synthesis techniques have been experimented with, although, chemical synthesis methods have been predominantly used because of their ability to produce large quantities of nanoparticles with properties tailored as per application. The major challenges with the existing procedures are that they are complicated due to large number of variables involved in synthesis procedure and have high probability of contamination. Synthesis gets even more challenging when composite nanomaterials are to be developed. Thus, a relatively new gas phase synthesis method called spark ablation that relies on generation of spark discharge across electrodes to vaporize material and generate nanoparticles upon condensation to overcome these hurdles is discussed in section 2.1.1. Nanoparticles produced in the spark discharge generator is transported and collected in an aqueous media which results in oxidation of both Palladium (Pd) and Iron (Fe) nanoparticles.

The present research deals with the synthesis of PdO-USPION via spark ablation and subsequent characterization of the generated nanoparticles to determine their suitability as theranostic agents. This method of PdO-USPIONs synthesis has never been attempted before. Thus, first part of this thesis work involves understanding and exploiting the influence of system parameters i.e., voltage, current and flow rate to produce PdO-USPIONs with desired properties. Second part of the research is dedicated to gain knowledge about their heating and contrast agent performance. Another key aspect to bear in mind is that inactive palladium is used in this work.

1.1. Research Question

Can PdO-USPIONs with tailored magnetic and morphological properties be produced via spark ablation for the purpose of thermal ablation and contrast enhancement?

Sub-research questions that will be answered as a part of this work are:

1) What operating conditions with respect to spark energy, frequency, gas flow rate are optimum for the generation of USPION & (oxidized)Pd-USPION nanoparticles?

2) How do the parameters influence size, shape and magnetic properties of PdO, USPION and PdO-USPION alloy nanoparticles?

3) Can the nanoparticles generated by spark ablation mechanism be used for Magnetic thermal ablation application?

4) What is effect of surfactant over the aggregation behaviour of the generated nanoparticles? Can it improve the magnetic properties leading to improved heating and imaging performance?

5) Can PdO-USPIONs generated be used as T1 contrast agent?

2

Background

This chapter is divided into two parts: Section 2.1 introduces key theoretical concepts and experimental studies associated with generation of nanoparticles via spark ablation. Section 2.2 deals with the study of influence of size, shape and composition over magnetic properties that dictate heating and contrast enhancement ability of superparamagnetic (Substituted)Iron oxide nanoparticles. This is a short version of the literature study conducted as a part of the master thesis. Results from experimental and characterization studies are used as a framework for the development of suitable PdO-USPIONs.

2.1. Background on Spark Discharge Generation

2.1.1. Synthesis

A typical spark discharge generator (SDG) consists of a leak-proof reactor chamber housing a pair of opposing metallic or semiconductive electrodes separated by a small gap, an inlet nozzle and an exhaust nozzle. Electrical circuit for such a set up is shown in figure 2.1 [7]. Inert gas flowing through the inlet nozzle is directed towards the gap between electrodes. A high power DC source intermittently charges the shunted capacitor and thus a high voltage difference is applied across the electrode gap. The electrode that is initially connected to the negative terminal acts as a cathode whereas the electrode connected to the positive terminal acts as an anode. When the capacitor attains a sufficient voltage known as "Breakdown voltage", electrical discharge occurs over the gap. This breakdown mechanism works in accordance with the Paschen's law which states that the voltage at which the gaseous dielectric medium will start to become conductive is directly proportional to the gaseous pressure in the gap and the distance between the electrodes [7][8] . The breakdown is initiated by the pre-existing charge carriers in the gas which accelerate in the electric field and eject more electrons from neutral atoms resulting in an avalanche. The electrons and positive ions migrate towards the electrodes of opposing polarity. The electrons have much higher mobility compared to positive ions and get absorbed in the anode. However, owing to their mass, positive ions cause secondary electron emissions from cathode on impact thus, establishing a self-sustaining plasma channel or arc across the electrodes. Due to high current, discharge arc attains a temperature as high as 20,000 - 30,000 K [9]. This thermal energy is applied over a small area of electrode which results in evaporation of electrode material after being heated far above its boiling point. It is important to note that arc plasma is microsecond long, damping oscillatory discharge. This oscillation of spark between electrodes is due to inductive nature of the RLC circuit and it is

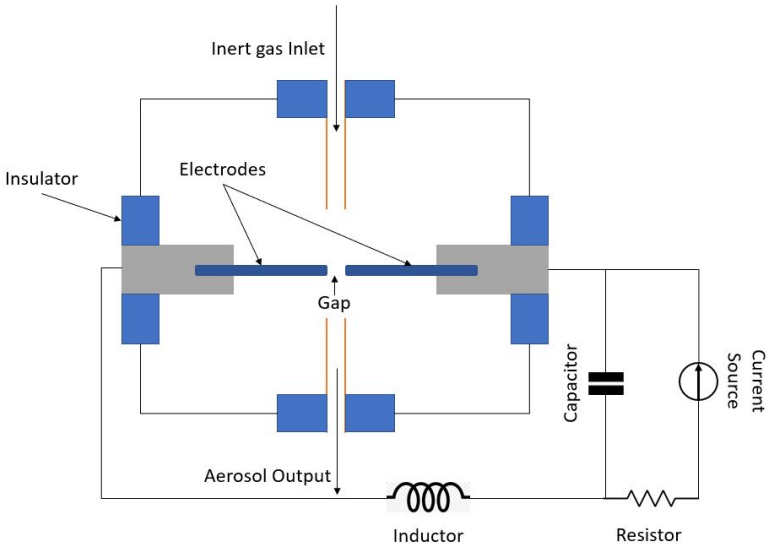

Figure 2.1: Schematic of a typical Spark Discharge Generator circuit (Modified version of circuit from S Tabrizi et.al., 2012) [7]

essential for erosion of both the electrodes. Although, more material is eroded from cathode than the anode because of positive ion bombardment at the onset of discharge and the damping behaviour of spark lowers the contribution from anode [10].

The plasma plume containing the species of the inert gas and the electrode material is released between the electrodes and in the vicinity of the electrode setup. This adiabatic expansion and diffusion results in the condensation of metal vapour when mixed with the surrounding inert gas [8]. The condensation is followed by clustering, nucleation and growth of nanoparticles whose mechanism is expounded in the following section. The aerosol containing nanoparticles formed at the gap is carried by the inert gas out of the system for collection. The design and use of SDG was first proposed by Burtscher and Schmidt-Ott in 1984 [11][12].

2.1.2. Nanoparticle Formation Mechanism

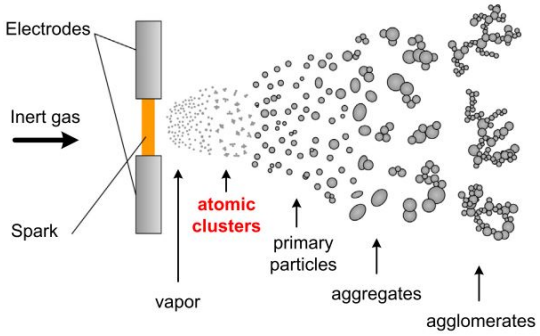

Figure 2.2: Stages of Nanoparticle Formation [13]

The stages involved in the nanoparticle formation is shown in figure 2.2 [13]. Inert carrier gas facilitates the quenching i.e, rapid cooling of the hot atomic plasma plume. As a result of quenching, supersaturated vapour exhibiting excess (Gibbs) free energy is observed in the system [14] [15]. The atomic clusters are formed during the condensation process. When the atomic clusters have attained a certain critical size, nucleation process sets in. There are two ways of nucleation namely Heterogeneous and Homogeneous nucleation [16][17]. Heterogeneous nucleation occurs with the aid of foreign particles or surfaces. In the SDG sys-

tem, only means of heterogeneous nucleation is the electrode surface upon which the formation of nuclei can be observed which is less often because of the extreme temperature of the surface that evaporates the formed particles immediately. If there are impurities present in the gas, that could also result in the nucleation. Heterogeneous nucleation is a low energy process as it utilizes the surface of impurities to coalesce atomic clusters. This however, is not a favourable product outcome. Thus, the purity of the produced nanoparticles depend on the purity of the electrodes and quenching carrier gas. Synthesis of nanoparticles in SDG is primarily by homogeneous nucleation. It requires high activation energy to create nucleus. Driving force for the homogeneous nucleation is the thermodynamically unfavourable positive free energy in the system owing to high surface energy. Hence, atomic clusters with a critical size at which the bulk energy is slightly higher than the surface energy is a pre-requisite for nucleus formation via homogeneous method [15]-[18]. These atomic clusters become the nucleation sites. The critical size where stable clusters are formed varies for different metals. Energetically suitable spherical nuclei result from this method and thereby reducing the free energy of the system. Depending on the number of atomic clusters, size, proximity, temperature and cooling rate, average primary particle size is obtained. The factors that influences the aforementioned parameters and thereby controlling size and morphology of the produced nanoparticles are discussed in section 2.1.3. The primary nanoparticle size for numerous semi-/conductive materials is noted to be in the range of 1-10nm [19][20].

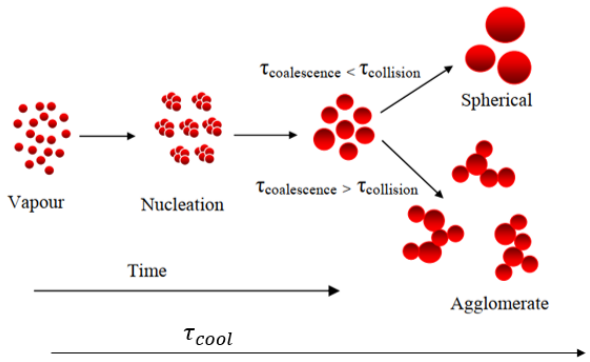

Figure 2.3: Influence of Coalescence, collision and cooling on generation of nanoparticles [20]

The temporal growth of the nanoparticles based on the coalescence and collision rate is shown in figure 2.3 [20]. Coalescence time (τ_f) is the amount of time taken by the particles to fuse to form particles of higher concentration and size. Collision time (τ_c) is the time between two successive particle collisions. Amount of time needed for the particle to cool is known as cooling time (τ_{cool}) which depends on the temperature and rate of carrier gas flow. It has also been observed that the particle temperature increases as a result of coalescence or fusion which is depicted in figure 2.4 [21]. This happens due to high vibration and motion of atoms during solid state diffusion. Most atoms tend to be on surface where as the interior atoms tend to migrate to occupy the voids during fusion of two clusters. On fusion of the atomic clusters, surface energy of the formed particle is lower than the source clusters. This reduction in energy combined with the motion of atoms result in the liberation of thermal energy (conservation of energy holds). This rise in particle temperature is beneficial for efficient fusion which would result in larger spherical structures. However, this occurs only when $(\tau_f) < (\tau_c)$. If $(\tau_f) > (\tau_c)$, probability of collision with the subsequent cluster is much higher compared to fusion rate, then the source clusters do not get sufficient time to sinter completely and would result in non-spherical aggregates or dendritic agglomerates containing multiple small particles which would be held together by weak van waal forces. Increasing quenching gas flow rate increases the cooling rate (τ_{cool}) of particles and the amount of time spent by the clusters in the high volume loading region is lowered where

larger percentage of nucleation and growth occurs. This leads to smaller sized particles [21][22].

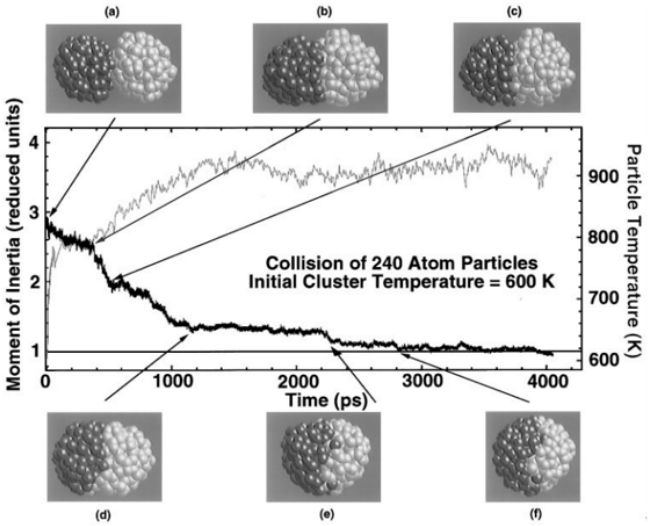

Figure 2.4: Particle morphology evolution during coalescence as a function of temperature[21]

2.1.3. Factors influencing Nanoparticle formation

The quantity and the properties of the nanoparticles generated from spark discharge system is dependent on three major parameters - energy of the spark (E_{spark}), the spark repetition frequency (f_{SRR}) and gas flow rate (Q). In this section, all the factors influencing the produced nanoparticles are discussed.

Influence of Spark Energy

The amount of nanoparticles produced is directly proportional to the energy dissipated per spark which depends on the capacitance of the capacitor (C) and discharge voltage V_d given by equation 2.1.

$$E_{spark} = \frac{1}{2} C {V_d}^2 \tag{2.1}$$

The voltage at which the discharge takes place is according to:

$$V_B = \frac{Bpd}{\ln(Apd) - \ln[\ln(1 + \frac{1}{\gamma_{se}})]} \tag{2.2}$$

where V_B is the breakdown voltage, p is the gas pressure, d is the electrode gap, A & B are excitation and ionization coefficients and γ_{se} is the coefficient associated with secondary emission of electrons from cathode. Generally the pressure of the gas is kept constant so as to run the system efficiently at atmospheric pressure. However, the gap between the electrodes can be varied to alter V_B. The discharge hardly ever occurs exactly at the breakdown voltage. Charging and discharging of the capacitor is not an instantaneous process. If the spark repetition rate were to be increased, the gradual increment of voltage to attain breakdown cannot be achieved. Thus there is nearly always an added voltage V_0 as expressed by equation 2.3. The discharge voltage behaviour across the gap as a function of time can be seen in figure 2.5 [13][23].

$$V_d = V_B + V_0 \tag{2.3}$$

Amount of eroded material from electrode as a function of energy was investigated by T V Pfeiffer et. al. [13],

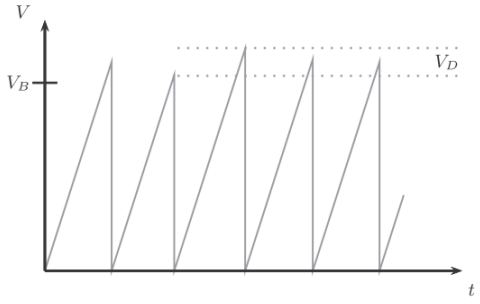

Figure 2.5: Voltage discharge as a function of time [13]

which is depicted in the graph 2.6. Clearly, a linear relation exists between spark energy and ablated electrode mass. This results in high volume loading and supersaturation. Atomic clusters containing higher number of atoms are formed which implies a high nanoparticle yield and size. Since, V_d can be varied by changing spark

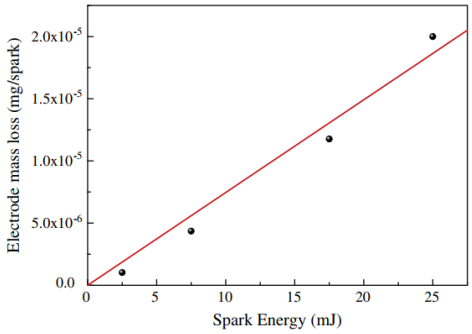

Figure 2.6: Nanoparticle yield as a function of energy per spark (C=20nF, d=1 mm, Q=0.8 L/min [Ar gas]) [13]

gap, S Tabrizi et. al., [24] showed that electrode mass loss linearly increases as the gap is increased as seen in graph 2.7 and the size distribution of the synthesized nanoparticles tend to be broader shown in graph 2.8.

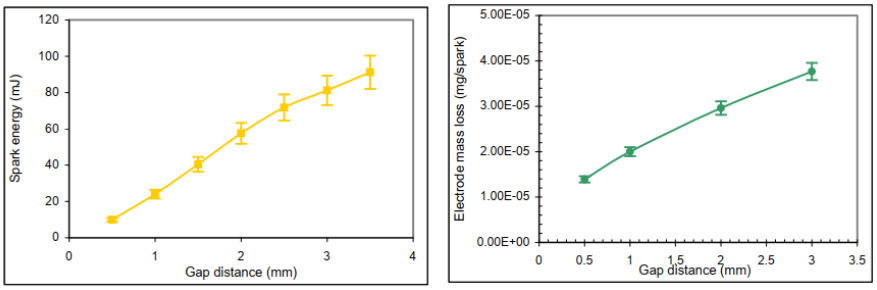

Figure 2.7: Energy per spark (left) and Nanoparticle yield (Right) as a function of spark gap (C=20 nF, f_{SRR}=150 Hz, Q=0.8 L/min [Ar gas]) [24]

Influence of Spark Repetition Rate

Having kept the capacitance and spark gap constant, spark repetition rate (f_{SRR}) can be varied by changing the current (I). Frequency at which the spark occurs is given by:

$$f_{SRR} = \frac{I}{CV_d} \tag{2.4}$$

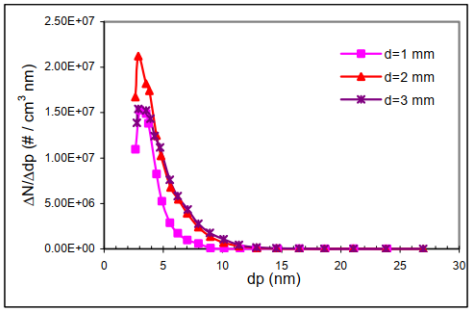

Figure 2.8: Size distribution as a function of spark gap (C=5nF, f_{SRR}=10Hz, Q=10 L/min [Ar]) [24]

The ablation rate exhibits a positive linear relation with frequency of spark as shown in figure 2.9. The re-

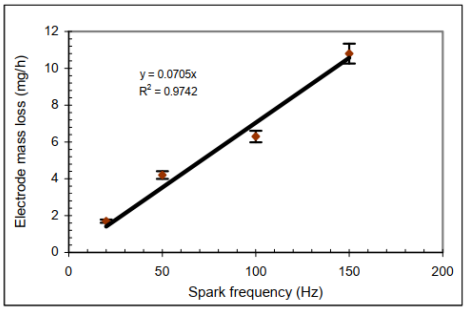

Figure 2.9: Nanoparticle production rate as a function of spark frequency (C=20nF, d=1 mm, Q=0.8 L/min [Ar gas]) [13]

lation is holds only until f_{SRR} reaches 500 Hz [23]. When the frequency is increased above this threshold by increasing current, the breakdown voltage is observed to go down and fluctuate rapidly as shown in figure 2.10. This instability arises due to incomplete flush out of the charge carriers residing in the electrode gap prior to the consecutive discharge event. Drastic drop in breakdown voltage at high f_{SRR} results in low energy dissipation per spark which in turn reduces the particle concentration and erratic particle size distribution. This is one of the key drawbacks with the spark ablation technique which poses a restriction on the range of usable voltage and current values [25][26].

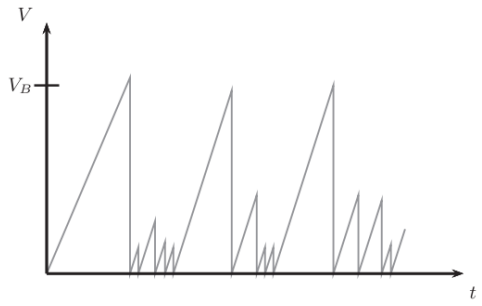

Figure 2.10: Discharge voltage at high spark repetition rate [13]

Influence of the Gas type and Gas flow rate

The type of gas used determines the composition, size and quantity of nanoparticles. For instance, if H_2 were to be used, metal hydride nanoparticles would be obtained. Presence of oxygen will lead to formation of oxidative layer over the particles. Breakdown voltage, heat transfer efficiency and cooling rate is also influenced by the type of gas used in the system. If the goal is to produce pure metallic nanoparticles, an inert gas such as

N_2 or Ar would be an apt choice. However, we can see from table 2.1 that the even through molecular nitrogen has comparable ionization energy to that of argon, N_2 has lower mean free path and higher thermal conductivity. This leads to high charge carrier formation, thus, a better conductive channel and efficient transfer of thermal energy to electrodes resulting in high ablation of electrode mass. It is precisely because of this reason that the primary particles generated in the SDG with N_2 as quenching gas tend to have larger size compared to other gases. Due to low mean free path, the nanoparticles tend to collide with the gaseous molecule with much higher probability, thus increasing the cooling rate as well when it functions as a carrier gas [20] [27]. Flow rate of the carrier gas strongly influences the cooling rate and the extent of dilution. At high flow rates,

Table 2.1: Properties of commonly used gases in SDGs [27]

Gas	Atomic Mass (emu)	Ionization energy (kJ mol^{-1})	Mean free path (nm)	Thermal conductivity (W $m^{-1}K^{-1}$)
N_2	14	1503	59	$2.59x10^{-2}$
Ar	40	1521	62.6	$1.77x10^{-2}$
He	4	2372	173.6	$15.1x10^{-2}$

particles do not reside in the high loading region for a longer time. Increased dilution also lowers the collision rate and due to increased cooling rate, particles do not sinter thoroughly. Hence, increased carrier gas flow rate reduces the size of the nanoparticles. Research done by J. Feng et.al., [14] showed that particle size at flow rates beyond 5lpm did not exhibit much variation in the primary particle size as shown in figure2.11.

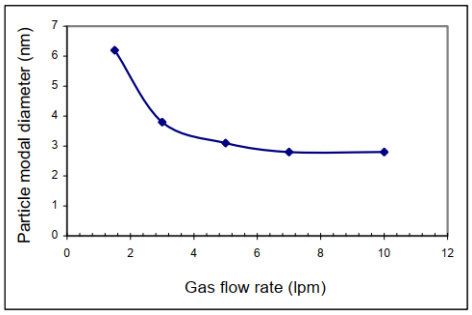

Figure 2.11: Nanoparticle size as a function of carrier gas flow rate [24]

Influence of the Material

Ability of the Spark discharge technology to generate numerous metal and semiconductor nanoparticles without having the need to alter design and components except for the electrode material is the prime advantage compared to chemical means of synthesis. It is clear that the properties of source material significantly affects the nanoparticle generation process [28]. Apart from system parameters such as energy per spark (E_{spark}), duration of spark (τ), thermal conductivity of carrier gas (k_g) and temperature of the gas (T), the ablated mass depends on properties specific to material such as the boiling point (T_b), melting point (T_m), heat capacities C_s and C_l of solid and molten/liquid material state respectively, enthalpy of vaporization (H_v) and fusion (H_f) and thermal conductivity of electrode material (k_e) as per Llewellyn Jones model [29] which is denoted by the following equation:

$$\Delta m = \frac{\alpha E_{spark} - 2\pi r^2 \sigma \tau ({T_b}^4 - T^4) - 2\pi r \sigma \tau k_e (T_b - T) - 2\pi r \sigma \tau k_g (T_b - T)}{C_s(T_m - T) - C_l(T_m - T) + H_f + H_v} \tag{2.5}$$

σ is the Stefan-Boltzmann constant, α is the fraction of spark energy utilized for nanoparticle generation since a large portion of the spark energy is converted to sound and light energy and r is the spark radius. It can be clearly seen that metals with high enthalpy of fusion and vaporization will tend to be more resistant towards spark erosion. Higher thermal conductivity of quenching gas leads to elevated supersaturation. High average heat capacities require large amount of heat energy to be able to rise the temperature of the material [8]. Further, the tendency of the material to form oxides also affect the size and agglomeration rate of the generated nanoparticles. Oxide layer over the surface hinders the coalesce process and leads to neck formations or larger agglomerates held together by weak bonds. Thus, to produce pure metal nanoparticles, quenching gas must be devoid of the slightest trace of oxygen. Tabrizi [20] reported primary particle size of Pd to be around

Table 2.2: Thermal properties of Palladium and Iron Electrodes [30][31]

Electrode material properties	Palladium (Pd)	Iron (Fe)
Boiling Point (T_b) [^{0}C]	2963	2862
Melting Point (T_m) [^{0}C]	1555	1538
Enthalpy of Vaporization (H_v) [kJ/mol]	357	354.1
Enthalpy of fusion (H_f) [kJ/mol]	17.6	11.7
Thermal conductivity (k_e) [W/m K]	72	79.5

4nm based on Transmission Electron Microscopy (TEM) images. Ullmann et.al., [32] observed a primary particle size of 8nm in case of Iron oxide nanoparticles which were produced by laser ablation technique. As per the findings of Ullmann, nanoparticles generated by laser ablation and spark ablation tend to exhibit comparable size distributions. Thus, we can expect primary particle size of Iron oxide nanoparticle to be similar as to the one reported by Ullmann. It can be deduced from table 2.2, that amount of palladium produced will be slightly less than iron due to high enthalpy of vaporization, fusion, boiling and melting point. Thermal conductivity on the other hand is lower in case of palladium which indicates less efficient heat transfer and lower electrode erosion. Thus, the palladium nanoparticles can be expected to have smaller primary size compared to iron.

2.1.4. Generation of Composite Nanoparticles

As mentioned in section 2.1, the discharging current is oscillatory in nature due to the electrical properties of the RLC network. This oscillation is responsible for the vaporization of the electrode material. Each of the electrodes are subjected to strong ablation depending on the polarity of the oscillating discharge current resulting in internally mixed nanoparticles as shown in figure 2.12 [33]. Due to reasons mentioned in section 2.1, the cathode material tends to ablate more than the anode. This leads to disproportion in the contribution from the two electrodes. The ratio in which the material from each of these electrodes is eroded is given by:

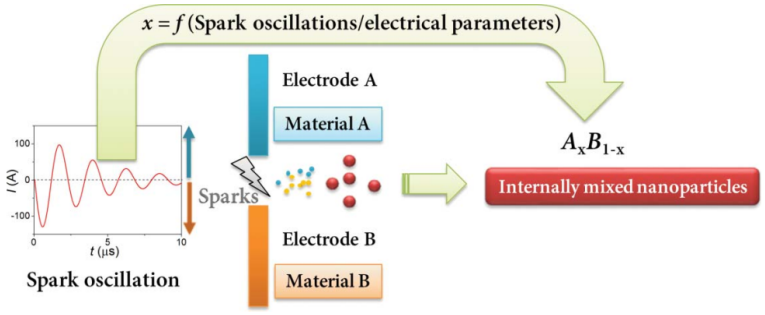

Figure 2.12: Generation of composite nanoparticles with the use of different electrode material [33]

$$R = \frac{E\alpha_C}{E\alpha_A} = \frac{\int_0^\tau I^2 dt(I<0)}{\int_0^\tau I^2 dt(I>0)} \tag{2.6}$$

where R is the ablation ratio, $E\alpha_C$ is the energy discharge at the cathode, $E\alpha_A$ is the energy discharge at the anode, I is the oscillating current and τ is the duration of oscillation. Thus, electrode mass loss is proportional to the amount of energy discharged at each of the electrode. The amount of heat energy released is proportional to I^2Rt. The material's ability to absorb the energy per spark must also be taken in to account which is given by the material specific constant C_C for the cathode material and C_A for the anode material. This leads us to the following expression for the total mass of composite material [33]:

$$\frac{\Delta m_C}{\Delta m_A} \approx R\frac{C_C}{C_A} \tag{2.7}$$

Tabrizi [20] performed extensive research on the generation of bimetallic composites with different materials such as Co-Cr, Cu-W, Au-Pd and Ag-Pd. Effect of different system settings such as capacitance, spark gap, electrode reversal and spark repetition rate was investigated. No significant difference in the weight ratio was observed with the variation in capacitance, flow rate and frequency.

2.1.5. Nanoparticle capture in solution

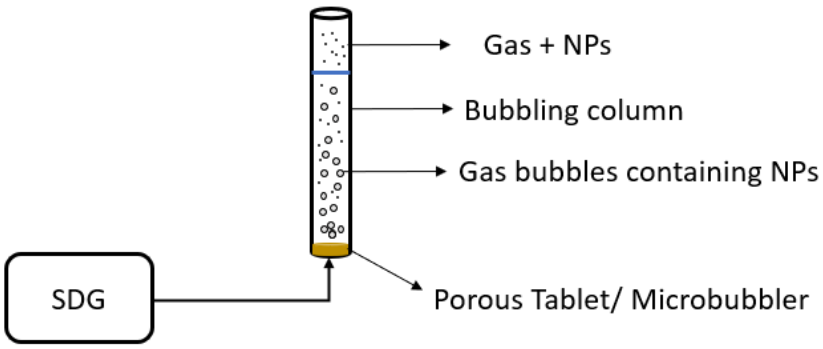

Figure 2.13: Nanoparticle collection in liquid

Nanoparticles are generally coated and suspended in solvents before being injected into the body. Typically solvents that emulate the internal environment or body fluids are used to ensure biocompatibility. Thus, keeping the end use in mind, nanoparticles produced in particle generator are carried by a carrier gas that is bubbled through a deionized water or water-based liquid as shown in figure 2.13. The aerosol carried by the carrier gas is bubbled through the liquid column in which the nanoparticles are deposited. This deposition is a result of diffusion of the nanoparticles from the bubble into the deionized water. Effectiveness of nanoparticle collection in the liquid column depends on the coefficient of absorption for diffusion process and the height of the liquid column which is given by equation 2.8 [34].

$$C_p = C_0 \exp^{-ah} \tag{2.8}$$

where C_p is the concentration of nanoparticles remaining in the gas bubble, C_0 is the concentration of nanoparticles prior to the onset of diffusion within the gas bubble, a is the absorption coefficient and h is the height of the liquid column. The absorption efficiency in turn varies depends on the diffusion coefficient (D), bubble

rise velocity U_b and the radius of the aerosol bubbles (r) which is expressed as:

$$a = 1.8(\sqrt{\frac{D}{U_b r^3}}) \tag{2.9}$$

Larger the bubble radius, longer will the nanoparticles reside in the gas bubble. The diffusion rate can be altered significantly by controlling the bubble radius. The radius of the generated aerosol bubble depends on the aperture size of the perforated plate or microbubbler or a porous tablet used (O_d), carrier gas flow rate (Q), viscosity (ν) and surface tension (σ_t) of the liquid. This relation was postulated by Gaddis et.al., [35] which is represented as:

$$r = 0.5[(\frac{6O_d\sigma_t}{\rho g})^{\frac{4}{3}} + (\frac{81\nu Q}{\pi g}) + (\frac{135Q^2}{4\pi^2 g})^{\frac{4}{5}}]^{\frac{1}{4}} \tag{2.10}$$

It can be concluded from equation 2.10, that the radius of the aerosol bubble increases with increase in quenching gas flow rate and the aperture size. Thus, low-moderate flow rate will be more suitable for improving the diffusion rate of the nanoparticles from the aerosol bubbles as the radius is lowered. Charvet et.al., [36] however noticed an improved collection efficiency when the flow rate is quite high. This behaviour is reasoned to be due to formation of large quantity of microbubbles at extremely turbulent flows at the base of the liquid column. This is observed at flow rates above 12-15 lpm. This generally is not applicable for practical purposes as it would require bubbling columns with large height so as to avoid overflow of the liquid and thus result in loss of nanoparticles. Nanoparticle absorption probability in the liquid column can be raised even by increasing the height of the liquid column keeping the practical limits in mind. This is due to the fact that the bubbles reside in the column for a longer duration and thus the concentration of nanoparticles in collection liquid will increase due to higher diffusion. Aperture size of the holes through which the aerosol is bubbled can be decreased in size so as to reduce the radius of the formed bubble. Increase in density reduces the size of nanoparticles. Reduction in surface tension and viscosity lowers the radius of bubbles too.

The prime issue with nanoparticle capture in water is that it would result in oxide formation of both iron and palladium. Additional nanoparticle loss due to deposition in the carrier tube, on the porous tablet or microbubbler, on the surface of the glass column and diffusive escape of nanoparticles from the liquid can be observed with this method of nanoparticle capture.

2.2. Background in Magnetism

2.2.1. Superparamagnetism

Every magnetic material is known to possess an "easy axis" of magnetization which largely depends on the crystalline structure. It is the energetically favourable direction along which the saturation magnetization can be achieved with lowest magnetic field intensity. The field strength required to change the direction of magnetization with respect to the easy axis is known as Anisotropy field (H_k) and the energy corresponding to this field is known as anisotropy energy (K). As ferri-/ferromagnetic particles transition from multi- to single domain, anisotropy increases. However, with ferromagnetic particles smaller than 25 nm tend to exhibit low anisotropy energy. At this scale, if thermal energy exceeds the anistropy energy barrier, magnetic reversal is observed resulting in net zero magnetization in the absence of external field. This indicates the behavior of paramagnets. When these nanoparticles are subjected to external magnetic field, they align with in the direction of the field. Due to large magnetic susceptibility associated with these nanoparticles, the net moment is higher than a comparable paramagnet, thereby called superparamagnet. When (substituted) superparamagnetic iron oxide nanoparticles attain sizes below 10nm, the net magnetization decreases because large number of atoms with incomplete bonds tend to occupy surface than at the core and undergo random fluctu-

ations. These atoms on the surface cancel each other's magnetic moment also known as spin disorder effect. Superparamagentic iron oxide nanoparticles in this size range are called Ultra-small superparamagnetic Iron oxide Nanoparticles (USPIONs). Therefore, USPIONs tend to exhibit lower magnetic saturation compared to superparamagnets [37][38].

2.3. Magnetic Nanoparticle Heating Mechanism

When (U-)/SPIONs are exposed to the alternating magnetic field (AMF), they tend to experience two forms of relaxation losses. Type of magnetic loss varies in accordance with the size and relaxation behaviour of the nanoparticles and are subsequently converted to heat energy when subjected to AMF. These nanoparticles when injected in the tumour location and subjected to AMF, tend to transfer the heat to the surrounding tissue or cells resulting in thermal ablation or hyperthermia condition based on the temperature level and response of the diseased cells towards the thermal energy transfer. These mechanisms are explained in the following section.

2.3.1. Relaxation Loss

Magnetic nanoparticles in superparamagnetic regime do not exhibit any hysteresis losses owing to the lack of remnance and coercivity. However, two relaxation mechanisms pertaining to rotation of magnetic moment and the nanoparticle rotation are responsible for heat generation. Neel relaxation is associated with the rotation of the magnetic moment where as the brownian relaxation is associated with the complete rotation of the nanoparticle. The time taken by the magnetic moment to flip as a result of the thermal fluctuation is known as the Neel time. The flipping of spins are observed above a temperature thershold called blocking temperature (T_B) [37][39]. Neel relaxation time is expressed as [40]:

$$\tau_N = \tau_0 \exp^{\frac{E_{ka}}{k_b t}} \tag{2.11}$$

It can be seen that neel relaxation is strongly affected by the volume of the particle (V) and the anisotropy

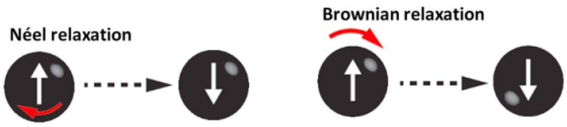

Figure 2.14: (A) Neel Relaxation and (B) Brownian Relaxation [40]

(K). At high anisotropy and when the size is under 25 nm, neel relaxation is predominant provided that the viscosity is low. When the hydrodynamic volume (V_H) increases and the viscosity (ν) of the surrounding medium rises, brownian relxation kicks in and the heating process is denoted by[37]-[40]:

$$\tau_B = \frac{3\nu V_H}{k_B T} \tag{2.12}$$

The total relaxation is always a combination of the relaxation processes given by the following equation:

$$\frac{1}{\tau} = \frac{1}{\tau_N} + \frac{1}{\tau_B} \tag{2.13}$$

For superparamagnetic nanoparticles, τ is determined mainly by τ_N because it reduces exponentially with reducing nanoparticles volume, while the decrease of τ_B is directly proportional to V_H. Power loss which is a quantitative expression of the liberated heat associated with susceptibility losses is given by Specific Absorp-

tion Rate (SAR) as per the expression [41]:

$$SAR = C_s \frac{m_s}{m_{NP}} (\frac{\Delta T}{\Delta t}) \tag{2.14}$$

where C_f is the heat capacity of the solvent, m_s is the mass of solvent, m_{NP} is the mass of nanoparticles and $\Delta T/\Delta t$ is the rate of change in temperature [41]. Power loss associated with the relaxation mechanism is given by [37]:

$$P = \frac{\pi {\mu_0}^2 \mu^2 {H_{ac}}^2}{3\rho k_B T} \frac{2\pi f^2 \tau}{[1 + (2\pi f t)^2]} \tag{2.15}$$

It can be concluded from the above expression that the power loss increases with increase in magnetic moment thus larger the volume of primary particle and anisotropy, higher is the heating ability. Higher the magnitude of the magnetic field, larger will be the power loss and so is the case with the frequency. However, increasing frequency guarantees higher power loss only up to the resonance condition is attained which follows $\omega = \tau^{-1}$ where $\omega = 2\pi f$. This is the basis for the Linear Response theory model for power loss estimation using particles of superparamagnetic regime. Thus, the highest SARs reported in the literature correspond to the size of the nanoparticles such that their relaxation time resonates with the frequency of the applied magnetic field. This increment in the power loss by square of the frequency is applicable only in the superparamagnetic regime and exhibits a direct proportionality as per equation 2.15 [42] [40] .

2.3.2. Factors influencing MNP heating

Nanoparticle heating and behaviour in biological ecosystems is affected by size, interface effects, shape, oxidant generation, surface charge, solubility, surface coating and chemical composition and magnetic behavior. In case of Substituted (U-)SPIONs, magnetic properties such as coercivity, magnetic saturation, anisotropy and so on are primarily dependent on size, shape and composition which is discussed in detail in the following section.

Size

As mentioned in section 3, superparamagnetic iron oxide nanoparticles (SPION) smaller than 25 nm exhibit zero remnance and coercivity which enhances stability and thus lower aggregation behavior. In the presence of external field, superparmagnetic NPs display paramagnetic behaviour with an exception of high magnetic susceptibility provided they are above the lower limit under which surface spin disorder effects are dominant. High surface to volume ratio and high surface energy causes (substituted) USPIONs to be chemically reactive and also increases agglomeration. In order to minimize the surface energy, USPION take on spherical shape. It can be seen from figure 2.15, that the highest SAR is in the range of 15-22 nm. The highest SAR in superparamagnetic regime to date has been reported by Gaudia et. al., [43] at 19nm. Tong et al. have showed that with increment in nanocrystal size, a dramatic elevation of SAR by 50-fold was seen from 11 to 33 nm sized Fe_3O_4 nanoparticles[44]. The peak SAR values attained are 1026 and 2560 W/g at applied magnetic field magnitude of 9.35 and 20.7 kA/m for 40 nm Fe_3O_4 nanoparticles[45]. A similar trend in the SAR values corresponding to increase in size was observed by Mohapatra et. al. [46], and Nemati et. al.,[41]. It can be clearly concluded that the heating capacity increases as the particles move into single domain ferromagnetic regime and particles lower than 10 nm do not generally exhibit significant heating effect due to spin disorder. If the produced SPIONs are to be suitable for theranostic application, a trade off must be performed with regards to SAR value so that it can be used both for the purposes of heating and imaging. [47][48]. However , Jordan et al., showed that the highly monodispersed maghemite nanoparticles with core size 3,5 and 7 nm coated with Dextran reported SAR values of 106,524,625 W/g respectively . Santiago showed that USPIONs can generate 323.22W/g

when subjected to AMF of 25mT and 835kHz and function as dual T1-T2 contrast agents[49]. In another study by Xiao Li Liu et. al., 9nm magnetite nanoparticles coated with polyethylene glycol (mPEG@2000) exhibited M_s of 51 emu/g and SAR of 370 W/g and attained a temperature of 42^oC in 6mins[50]. These USPIONs exhibit high monodispersity and very low aggregation due to coating which reduces the influence they have over each other's magnetic behavior when dispersed in the solvent.

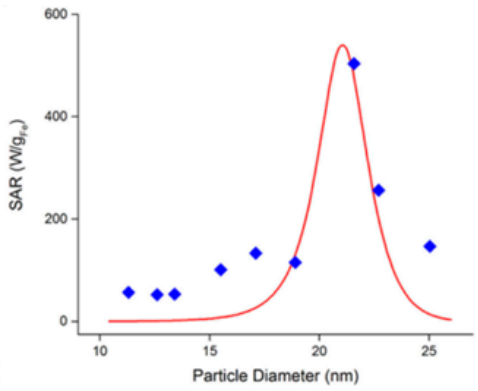

Figure 2.15: Simulated and experimental SAR values corresponding to SPIONs [42]

Shape

Shape anisotropy is due to the presence of the atoms on the surface of the nanoparticles that are not bonded due to lack of atoms in one or many neighbouring sites. Depending on the shape of the nanoparticle, the anisotropy varies. Magnetic anisotropy has shown to be strongly influenced by the shape of the nanoparticles. Depending on the improved magnetic properties, SPIONs of cubic structure performed as better heating candidates compared to the spherical structures as shown in figure 2.16. It can be seen from the figure that the magnetic moments align parallel in the cubic structures and spin disorder is noticed only at the corners where in case of the sphere due to its curvature, spins are oriented in direction with varying angles. This results in higher disorder so lower anisotropy and thus less heating ability [42] . Considerably high SARs has been published for rods as a consequence of the enhanced magnetocrystallline anisotropy. Fe3O4 nanorods with aspect ratio ranging from 6 up to 11 has been reported to exhibit SAR ranging from 300-840 W/g by Das et.al [51]. Nemati et. al., showed an increase in the SAR of 650 W/g for 52 nm sphere to 800 W/g for 30nm cube [41]. Particles produced via spark ablation are going to be spherical due to homogeneous nucleation and are of ultra small size. We can expect lower SAR values when USPIONs are subjected to alternating magnetic field.

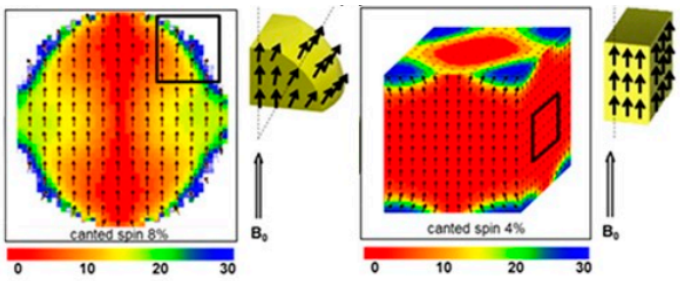

Figure 2.16: Spin disorder distribution based on the shape of the nanopartcles [42]

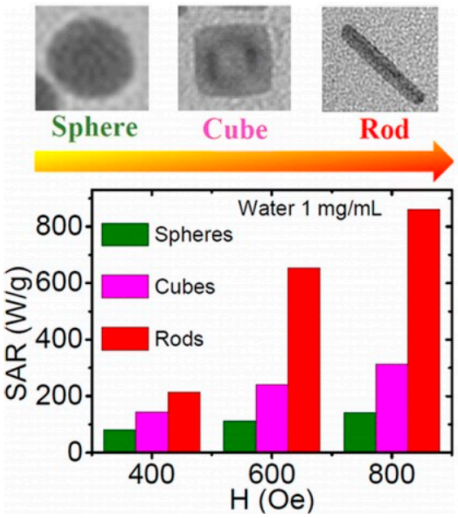

Figure 2.17: SAR enhancement with improvement in magnetic anisotropy in accordance with the shape [42]

Composition

Increase in magnetocrystalline anisotropy increases the heating ability by substituting the cations with higher number of unpaired electrons. This increases the net magnetic moment. Some of the cations that can be substituted in iron ocide nanoparticles are manganese with 5 unpaired electrons, iron with 4 unpaired electrons, cobalt with 3 excess spins and nickle with 2 spins [52]. Sathya et al. [53], observed an SAR value of 132 W/g for pure Fe3O4 nanoparticles at 265 kHz with an ACMF amplitude of 491 Oe and after doping Co^{2+} ions, the power loss improved to 534 W/g. Even though cobalt has lesser number of spins compared to iron, the solid state diffusion in to the voids and interaction with neighbouring atoms resulted in increased magnetocrystalline anisotropy. Thus, improving the heating ability. Spaldin [54] reported M_s of 110 emu/g ($MnFe_2O_4$), 101 emu/g ($FeFe_2O_4$), 99 emu/g ($CoFe_2O_4$)and 85 emu/g ($NiFe_2O_4$). M_s values of 6 nm size $MnFe_2O_4$ nanoparticles was 71 emu/g. Mahopatra [55] reported an SAR increment from 132 to 534 W/g when pure magnetite nanoparticles were doped with $Co_{0.5}Fe_2O_4$. Yang et.al., [56] showed that increasing Zinc content up to 0.6 lead $Zn_{0.6}Fe_2O_4$to exhibit M_s of 91 emu/g which is close to bulk M_s value of iron. Jang et. al [57] $Zn_{0.4}Fe_{0.6}$ Fe_2O_4 showed four-fold enhancement in hyperthermia effect of 15nm composite nanoparticles. Just as Zinc, palladium is also a diamagnetic material. It must be investigated whether palladium substitution leads to similar magnetocrystalline anisotropy in which case, it could potentially improve magnetic saturation and heating ability.

2.4. Magnetic Resonance Imaging

Magnetic Resonance Imaging (MRI) is a non-invasive and non-ionizing soft tissue imaging modality. MRI technique relies on manipulation of water protons (^1H) of the body. Image generation is initiated by immersing the protons or spins in a homogeneous magnetic field also known as main magnetic field (B_0). Despite the constant molecular interactions and Brownian motion, majority of the spins align in the longitudinal direction (z-axis) i.e., direction parallel to B_0 resulting in net magnetization (M_0). Further a radiofrequency (RF) pulse is applied to flip the spins on to transverse plane (XY plane). Spins can be efficiently pushed on to the XY plane only when the frequency of RF pulse is in resonance with the frequency with which the spins precess around the longitudinal axis. Upon removal of RF pulse, spins attempt to revert back to equilibrium state which is facilitated by two relaxation processes namely T_1 and T_2 relaxation as shown in figure 2.18. T_1 relaxation is associated with the time taken by the spins to recover magnetization along longitudinal axis

and T_2 relaxation time is based on the disappearance of spins from the transverse plane as a consequence of dephasing of spins. Dephasing occurs due to variation in the precession speed among spins. Deformation or bending of magnetic field is observed when the object is placed inside the scanner which leads to additional dephasing of spins. Thus, magnetization decay in XY plane occurs at a much faster rate which is given by T_2^* relaxation. The change in magnetization and decay in the transverse plane induces an oscillating current signal in an RF coil which is measured by the detectors [58] [59].

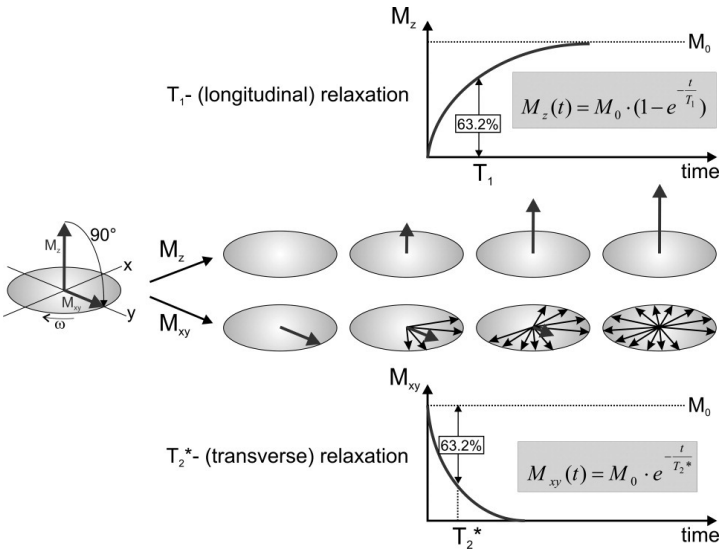

Figure 2.18: T1 and T2 relaxation [58]

Time constant T_1 indicates the time at which 63.2% of M_0 is recovered along z axis and T_2 constant is a time at which 36.8% of M_0 is still precessing in transverse plane [58]. Relaxation time associated with different tissues are characterized by T_1 and T_2 constants as shown in figure 2.19. It is precisely the variation in rate of relaxation that leads to generation of images with contrast which helps us to distinguish among tissues. The signal strength and intensity variation among tissues also depend on field strength, proton density in each tissue and diffusion.

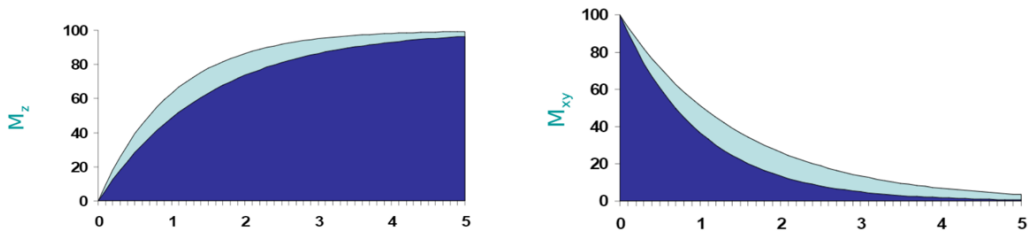

Figure 2.19: Difference in T1 and T2 between tissues (Dark blue: tissue 1, Light blue: tissue 2) [60]

2.4.1. Contrast Agents

Despite the inherent contrast in MRI, visibility of object of interest can be enormously improved through the application of contrast agents (CA). Contrast agents generally lower both T_1 and T_2 relaxation processes. However, one process dominates the other depending on the type of contrast agent. T_1 CA which are paramagnetic compounds primarily influence T_1 relaxation time. If T_2 process is significantly affected, it is said to be T_2 CA. Superparamagnetic iron oxide nanoparticles have been reported to perform as T_2 CA. Magnitude

and ratio of relaxivities, r_1 and r_2 are used for the classification and performance evaluation of CA agents which is estimated as [59][61]:

$$r_i = \frac{1}{\Delta T_i C}; for\, i = 1\&2 \tag{2.16}$$

where $1/\Delta$ T is the change in relaxation rate and C is concentration of CA. If the ratio of $r_2/r_1 \approx$ 1-2, it functions as a positive (T_1) contrast agent and $r_2/r_1 > 10$ is an indication of negative (T_2) contrast agent. T_1 CAs improve the efficiency of energy dissipation of spins to the environment and subsequent de-excitation to rest situation which produce bright images. On the other hand, T_2 CAs increase the rate of dephasing of magnetic moments resulting in darker images [61].

Gadolinium (Gd^{3+}) and Manganese (Mn^{2+}) based complex paramagnetic compounds have 7 and 5 unpaired electrons respectively which exhibit high magnetic moment and long spin relaxation time i.e., close to larmor or precession frequency. This is highly beneficial for efficient relaxation of surrounding water protons. Enhanced relaxation rate with the use of T_1 CAs can be explained by two mechanisms namely inner-sphere and outer-sphere relaxation. When water protons diffuse towards the metallic core, a strong dipole-dipole interaction is witnessed. Depending on the number of hydration sites on compound and proximity to core, chemical exchange of water molecules occur. This process is called inner-sphere relaxation. Outer-sphere relaxation involves spins that are further away from the core to undergo relaxation due to local magnetic field fluctuations induced by the CA. However, inner-sphere relaxation is dominant with T_1 CAs. Gd and Mn based CAs have been reported to cause lesions due to unwanted accumulation and toxic nature of metal ions [62].

Superparamagnetic iron oxide nanoparticles (SPION) on the other hand are favourable due to their biocompability and acts as T_2 CA. To avoid aggregation, improve magnetic properties, biocompatibility and lower hydrophobic nature of nanoparticles T_2 CA are generally coated with hydrophilic coating agents such as dextran or polyethylene glycol (PEG). Due to their high anisotropy and magnetic susceptibility, T_2 CA induce strong local magnetic field that increases dephasing of water protons that diffuse through the field. Thus, Outer-sphere relaxation is dominant in case of T_2 CA. T_2 relaxation strongly increases with increase in magnetic saturation of CA [59] [62].

2.4.2. USPION as T_1 contrast agent

As mentioned in section 4.3.2, Iron oxide nanoparticles smaller than 10nm are called Ultrasmall Superparamagnetic Iron Oxide Nanoparticles (USPION). Large number of ordered spins are necessary to induce stronger fields that increase T_2 performance. However, surface disorder effects are most evident in USPION due to their extremely small size which lowers the number of ordered spins at the core and leads to low magnetic saturation. These particles when subjected to external field, exhibit magnetic behavior as shown in figure 2.20 [63]. Higher percentage of metal ions at the surface increase the number and probability of water proton attachment at binding sites which enhances T_1 process. As mentioned in section 2.3.4, iron oxide nanoparticles generated via spark ablation can be expected to be in the range of 5-8nm. Thus, USPION have great potential to function as T_1 CA. Particles ≤ to 5nm are purely T_1 CA where as particles in the range of 6-10nm have shown to work as dual T_1-T_2 CA [64] [63] [65]. Kim et al [63] showed that USPIO with core size of 3nm and 3.7nm with PEG coating displayed r_1 relaxivity of $4.8 mM^{-1}s^{-1}$ and a low r_2/r_1 in 1.5T MR system. T_1 weighted MR images of rat with CA in its blood vessels showed a bright signal for a duration of 1 hour which is longer than Gd based CA and also showed an effective renal clearance. No toxic effects were observed even at a concentration level of 100μg/ml. In another study by Iqbal et. al, [66] r_2/r_1 of 6.5 was reported with the use of highly monodisperse silica coated iron oxide nanospheres of 5nm. To investigate biocompatibility, fetal bovine serum at different concentrations containing 0.7 mg/ml of USPION were analyzed over 24 hour duration to study the interaction of USPION with protein corona. Protein corona is essentially proteins from

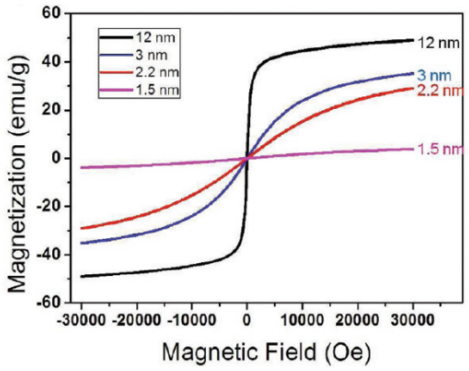

Figure 2.20: Nanoparticle size dependent magnetization curves [63]

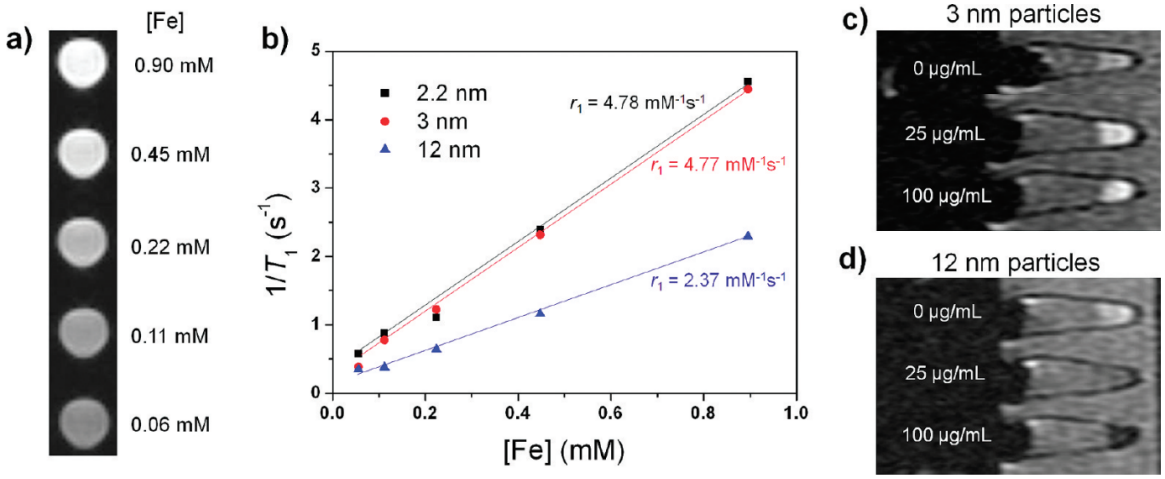

Figure 2.21: (a) T_1 weighted images of 3 nm-sized USION contrast agent. (b) Relaxation rate and corresponding relaxivity vs Fe concentration of iron oxide nanoparticles at varying diameters. (c,d) T1 weighted images of MCF-7 cell pellets containing IONP with sizes of (c) 3 nm and (d) 12 nm (after 24 hour incubation). [63]

interstitial fluid that are absorbed by nanoparticles when injected into the biological environment. It was reported that there was hardly any difference in the absorption behavior between serum with and without USPION. Cell viability >90% was observed in MCF-7 cells when incubated with USPION and monitored over 24 hours. In vivo MR imaging in 3T scanner was also performed by injecting silica coated USPION into a vein in the tail of a rat. The CA reached the heart and maintained a positive signal for 40 mins before staring to accumulate in the bladder and after 135 mins, most of the CA was located in the bladder as shown in figure 2.22. Above mentioned in vitro and in vivo studies successfully prove that USPIONs as T_1 CA exhibit low toxicity, high biocompatibility, good circulation half-life and aid in producing images of high resolution.

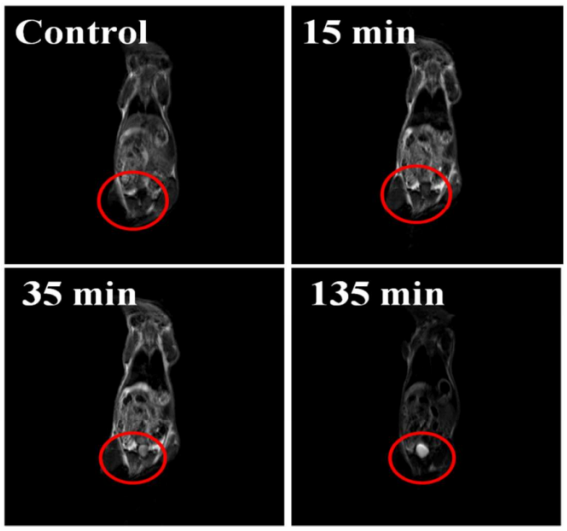

Figure 2.22: T_1 weighted images depicting temporal progression of CA through the body of rat[66]

2.5. Takeaways

For the purpose of thermal ablation, SPIONs in the range of 10-30 nm are generally preferred sizes. Ultra-small magnetic nanoparticles exhibit much lower stability because of their surface to volume ratio and low magnetic saturation due to spin canting. They have a higher tendency to agglomerate so as to reduce the surface energy. If USPIONs are to be used for the purpose of thermal ablation, high monodispersity and low agglomeration must be ensured. By doing so particles dispersed in the solvent have less influence over each other's magnetic behavior. Spark ablation is a simple yet versatile and highly scalable gas phase synthesis method suitable for production of iron and palladium nanoparticles. Despite the advantage of reproducibility, purity and simplicity that the technology holds over chemical synthesis method, spark ablation poses major challenge in terms of shape control, agglomeration and oxidation. Ultra small particles i.e, sizes < 10nm depending on the material properties can be generated with this method. Particle concentration can be increased with increase in voltage and current and by lowering flow rate. High monodispersity can be ensured at high flow rates. Production rate is limited by the frequency of operation of the system which is in turn regulated by current. Thus, a high voltage, high current setting and moderate flow rate would be most suitable. If larger particles are to be generated, tube ovens must be used to facilitate the sintering process. Lack of control over size distribution will be the key challenge during the external heat treatment process. USPION can be used as T_1 contrast agents due to low magnetic saturation and high surface to volume ratio which improves efficiency of energy dissipation into the surroundings i.e., enhanced T_1 recovery when water protons attach onto the surface. Substituted iron oxide nanoparticles have shown to improve magnetic saturation and magnetocrystalline anisotropy depending on the occupancy site of substituted cations, number of unpaired electrons, magnetic property and their interaction with the neighboring atoms.

3

Generation and Optimization Methods

This chapter describes the experimental methods employed to optimize the setup for the production of Pd-Fe inter-metallic nanoparticles via spark ablation. Ultimate goal is to be able to generate Pd doped USPION which could aid in thermal ablation and contrast enhancement.

3.1. Experimental Setup

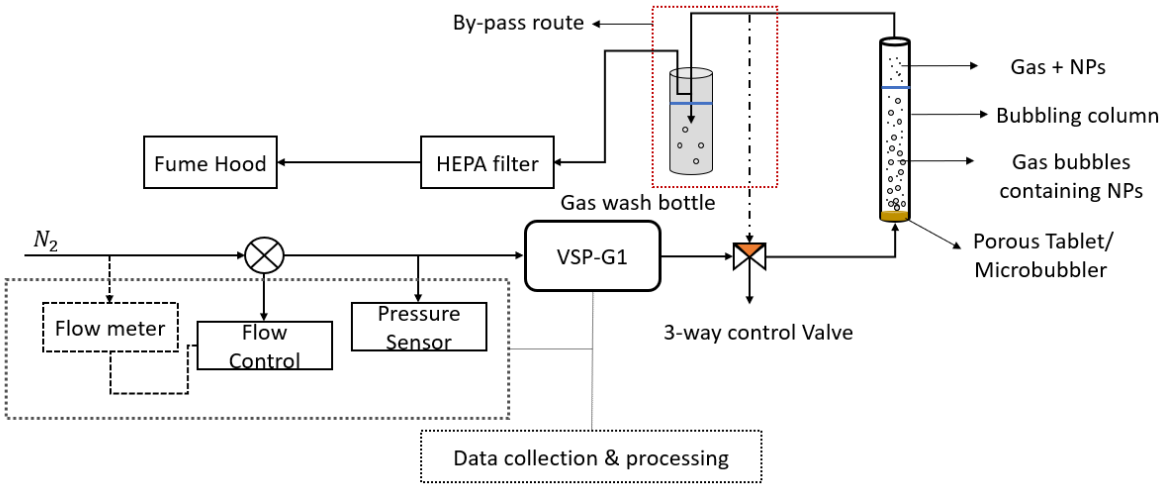

Figure 3.1: Experimental Setup (Updated version of setup from Tijn)[67]

The experimental setup remained nearly constant throughout the research period as depicted in figure 3.1. The system consists of generation, collection and exhaust unit. As mentioned in section 2.1.3, Nitrogen gas (N_2) used in this system facilitates spark generation, quenching and transportation of nanoparticles out of the generator. Flow controller is used to measure and regulate the carrier gas flow rate given in litres per minute (lpm). The gas pressure in the system is monitored with the pressure sensor. To ensure optimal performance, longevity of the device and safety, gas pressure is maintained around 1 bar. The system automatically shuts off if the pressure exceeds 1.4 bar. Synthesis of Nanoparticles in the VSParticle Generator (VSP-G1) is in accordance with the principle of spark ablation described in section 2.1.1. The current, voltage

and flow rate settings could be monitored and controlled both manually as well as through the VSP-G1 dashboard online. The carrier gas is flushed perpendicular to the electrodes and the produced NP aerosols are directed towards the bubble column containing Milli-Q water (highly pure, deionized water) for collection.

A perforated metallic disc (mesh/microbubbler/porous tablet) is placed at the bottom of the bubble column to prevent reverse flow of water into the generator and facilitate deposition of nanoparticles. Nanoparticles that do not diffuse from gas bubbles into water column get carried away to the gas-wash bottle. Gas-wash bottle containing water acts as both an additional filter to remove nanoparticles from carrier gas and a bypass route if the 3-way control valve at the base of the bubble column is closed. HEPA filter subsequently captures the nanoparticles escaped from gas-wash bottle before directing the nearly purified carrier gas to the fume hood. Further filtration of carrier gas is conducted in the fume hood prior to the discharge from the exhaust.

Primary objective of this thesis is to generate Pd-USPIONs via spark discharge generation for image-guided thermal ablation, suitability of which largely depends on the voltage, current and flow rate settings that dictate the yield and properties of nanoparticles. However, the initial set of experiments are designed to investigate the effect of system parameters only on the production of USPIONs. This process reduces the number of variables and aids in effective interpretation of the cause-effect relation during synthesis and characterization. Moreover, synthesis of inter-metallic Pd-Fe nanoparticle synthesis via spark ablation and particularly, in combination with nanoparticle capture in solution will be attempted for the first time. Thus, existing knowledge of (substituted) iron oxide nanoparticles (chemical means) and spark ablation technology combined with the optimization steps as illustrated in the following sections is used determine the most viable settings within the framework of the research and resources.

3.2. Synthesis of USPION

There are hardly any reports concerning nanoparticle production with VSP-G1 generator combined with deposition in bubbling column. Sharaf's [34] work on synthesis of gold (Au) nanoparticles with similar setup [1,2], despite the limited data, it is considered as initial benchmark to design preliminary experiments. The results of which are used to understand the production of nanoparticles with respect to generator settings and to tweak the setup and parameters accordingly.

Experiments 1 through 12 were aimed at determining the minimum production duration and set-points to generate sufficient nanoparticles to perform Dynamic Light Scattering (DLS) measurements thereby obtaining reliable hydrodynamic size and distribution. The settings similar to Sharaf's experiments in Table 3.1 were opted. Sharaf used Dynamic Mobility Analyzer (DMA) and not DLS to determine size.

Table 3.1: Selected Set-points and results of Sharaf's Experiments [34]

Voltage (kV)	Current (mA)	Gas Flow Rate (L/min)	Notes
1	5	1	Gives a moderate number of particles with a peak of 25-30 nm
1	5	2	Gives a moderate number of particles with a low peak of 15-20 nm
1	7.5	2	Gives a large number of particles with a high peak
0.7	2.5	2	Gives a relatively small number of particles with a peak of 12-15 nm

Count rate that is greater than thrice the background or preferable higher than 250 kHz but lower than

[1] Tabrizi showed that primary nanoparticle size of Au generated from SDG to be 5nm similar to Fe nanoparticles

[2] Sharaf used Ar as carrier gas which results in smaller size due to larger mean free path and lower thermal conductivity compared to N_2

950 kHz would correspond to precise reading of the sample with DLS. Key aspect to bare in mind is that a stainless steel mesh is placed at the base of the bubbling column during these experiments. Thus, the yield is specific to this setup. The relevance of which will be explained later in this section. A count rate of 275 kHz was obtained for the filtered sample after 18 hours when high voltage (V = 1kV), intermediate current (I = 5mA) and moderate flow rate (Q = 2L/min) was used. Further, Transmission Electron Microscopy (TEM) images were obtained to identify the primary particle size.

Large size distributions adversely affect the net magnetic property due to large variation in magnetic moment and stability of the collective nanoparticle system which make them unfit for thermal ablation application. Thus, at this stage, possibility of generating iron oxide nanoparticles of narrow size distribution and moderate size and quantity was being looked into. Thus, for experiments 12, 13 and 15, set-points of V=1kV, I=5mA and Q=2.2L/min that correspond to moderate yield, low peak (15-20nm) and narrow size distributions were used. Smallest peak at 17.2nm, 32.45nm and 4.795nm was obtained using DLS for the samples from each of these experiments. However, upon careful analysis and comparison of TEM images of samples, it was concluded that the primary particles remained around 5nm innall three samples.

The difference in peaks measured by DLS was assumed to be the result of aggregation over time i.e., the time between completion of the experiment and DLS measurement. To test this assumption, sample from experiment 14 was measured immediately after the experiment and after 4 days. Peaks measured at 11.65nm and 69.6 changed into one peak at 2172 nm thus, indicating aggregation of USPIONs.

To determine the largest NP size that can be generated in the system, maximum voltage (V=1.3kV), maximum current (I=10mA) and minimum flow rate (Q=0.5L/min) was chosen. Further, we know from section 2.1.3, higher flow rates result in smaller size nanoparticles. Thus, influence of flow rate varying from 0.5-2L/min retaining the highest voltage and current was examined from experiments 17 to 20. However, careful analysis and comparison of TEM images of samples from experiment 11 to 20 showed no difference in variation in primary particle size of USPIONs irrespective of settings and duration except that the agglomeration was expected to be larger at high power settings. Moreover, low flow rates resulted in excessive nanoparticle retention inside the reactor chamber thus lowering the amount of nanoparticles collected in the bubbling column.

Now that it has been established that the variation in primary particle size is negligible w.r.t settings, set-points that could result in highest yield was investigated. We have seen in section 2.1.3, moderate voltage and maximum current increases the frequency there by increasing production rate. In experiment 23, the voltage was set at 0.65 kV and current at 10 mA. High fluctuation in sparking was observed due to insufficient flush out of charges at high frequency. Thus, for the rest of the experiments from this point on wards, 1.3 kV and 10 mA was selected.

3.2.1. Effect of Isoelectric Point (IEP) and Ultra-sonication

USPION samples from experiments 17 and 18 were subjected to ultra-sonication at a frequency of 20kHz ±50Hz using Ultrasonic Processor (Cole Parmer), a probe sonicator of 750 W, at 20% amplitude and 27^{o}C for a duration of 3-5 minutes and sample 20 was placed in an ultrasound bath (nearly 300 W) as an attempt to re-disperse the aggregated particles. However, it can be seen from table 3.2 that aggregation increased further upon ultra-sonication. With increase in exposure time, aggregation and sedimentation was observed to increase further.

To understand the reason behind increased aggregation upon sonication, we should first understand the relation between Isoelectric point (IEP) of NPs and tendency to aggregate. The ultra-small iron oxide nanoparticles tend to be highly reactive and thus upon contact with water in the bubbling column, they get instantly oxidized. The surface of the iron oxide nanoparticles get covered with hydroxyl (-OH) groups as

Table 3.2: Difference in DLS measurement of Un-sonicated and Sonicated sample

Exp. No.	Un-Sonicated	Sonicated
17	21 and 71 nm	81 nm
18	8 and 62 nm	70 nm
20	9 and 80 nm	24 and 95 nm

shown in figure 3.2 resulting from chemisorption of water. Thus, a negative charge gets developed over the surface of USPIONs [68]. This also implies the presence of H^+ ions surrounding the negatively charged USPIONs. Depending on the pH of the surrounding medium, extent of positive or negative charge over surface of USPION gets established. If the combined surface charge arising from H^+/OH^- amounts to 0, then the corresponding pH value is known as Isoelectric Point (IEP) of the concerned nanoparticle [68].

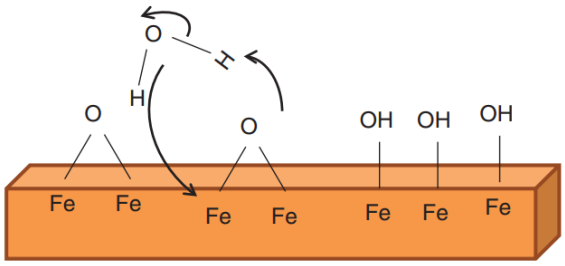

Figure 3.2: Schematic of IONP surface in water[68]

Having established that, now let us understand the mechanisms involved in aggregation of nanoparticles. Stability of colloid or suspension is based on Derjaguin-Landau-Verwey-Overbeek (DLVO) theory. According to DLVO theory, tendency of nanoparticles to coagulate is dependent on the total interaction potential energy (U_T) associated with the nanoparticles given by equation 3.1 [69].

$$U_T = U_A + U_R + U_S \tag{3.1}$$

where U_A is the attractive van der Waals force, U_R is the repulsive electrical double layer force and U_S is the solvent potential that can be generally neglected.

Particles dispersed in the aqueous medium tend to migrate towards other nanoparticles due to Brownian motion and gravity. During this process, the particles either attract, repel or exhibit a balance depending on the nature of nanoparticle, pH of the medium and distance of separation between particles. It can be seen from equation 3.2, energy associated with force of attraction goes by $1/r^2$, thus closer the particles are towards each other, higher will the U_A be and knowing that USPIONs are superparamagnetic, magnetic attraction due to dipole-dipole interactions can be neglected.

$$U_A = \frac{-A}{12\pi r^2} \tag{3.2}$$

where A is Hamaker constant and r is the distance of separation [69]

Repulsive Coulomb force that preferably counterbalance van der Waal's force is dependent on the stability of electrical double layer formed around the nanoparticle given in figure 3.3. As mentioned above, ions from the medium opposing the charge on the surface surround the nanoparticle which results in electrical double layer (EDL). When electric cloud enclosing the NPs overlap, they tend to repel each other. Multiple parameters as represented by equation 3.3 determine U_R.

$$U_R = 2\pi\varepsilon\zeta^2 \exp(-\kappa r) \tag{3.3}$$

where ε is dielectric constant of the medium, ζ is the zeta potential, κ is based on ionic strength and r is the particle separation

EDL can be divided into three regions with a potential energy associated with each layer. Primary layer is associated with potential arising from charges on the surface of NP. Next the inner stern layer consists of counterions resulting from electrostatic force with a (stern) potential related to it. Finally, relatively less firmly bound outer diffuse layer that consists of ions of different charge. The dominant charge concentration in diffuse layer is still dictated by the surface charge and the ions within this boundary are expected to be stable [70][69]. The potential energy drops with increasing distance from the surface of NP and a layer of the

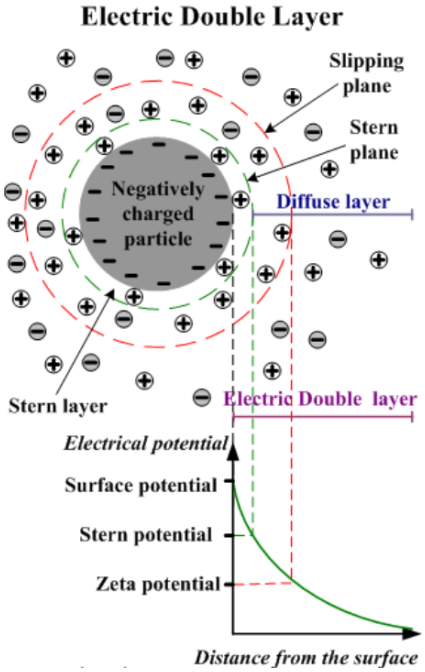

Figure 3.3: Schematic of Electric Double Layer[70]

dispersion medium attaches at the boundary which is called the slipping plane. The potential at this layer is known as zeta potential (ζ). Stability of the suspension varies with the magnitude of ζ which in turn is strongly dependent on the pH. The relation between ζ and pH is explored and exploited further in sections 3.3 and 3.4. At present, it will suffice to know that repulsive force is high when ζ is either too high or too low (above +30mV or below -30mV). Lower the ζ, higher is the aggregation tendency. Highest coagulation behavior is observed when ζ is close to 0 which corresponds to IEP value and if pH of the surrounding medium is nearly equal to IEP, then strong agglomerations can be expected [70][69].

The net potential energy at every distance of separation represented by the red curve in figure 3.4 is the sum of U_A and U_R. The positive peak is an indication of effect of repulsive force to keep the particles away from each other. However, as mentioned earlier, if the particles get further closer pushing past the energy barrier, a primary minimum given by the steepest dip in the graph is an indication of high attraction force which leads to irreversible aggregation. Ease at which the particles overcome the energy barrier can be influenced by thermal energy and collision [69]. Thus, when the sample was subjected to ultra-sonication, frequency of collision increased significantly and also resulted in increase in temperature of the solution depending on the duration of exposure. This led to increase in van der Waal's contribution. Another factor that facilitated the

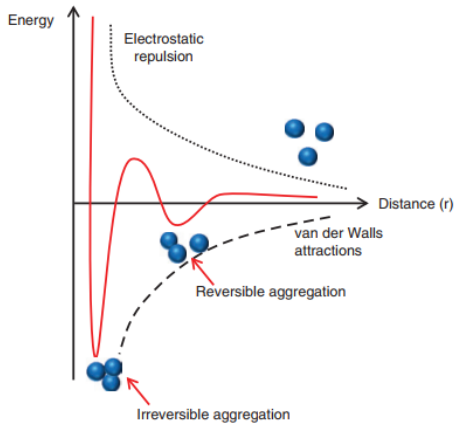

Figure 3.4: Total Electric Potential w.r.t particle separation (DLVO theory)[68]

agglomeration is the IEP of USPIONs. IEP of Iron oxide is around 6.8 which is close to the pH of the Milli-q water (pH = 7). ζ is close to 0 at this IEP and thus, increase in aggregation is observed over time [68].

3.2.2. Setup-modifications to improve absorption efficiency in bubbling column

Milli-q water volume of 100ml was used until experiment 20. From section , we know that the absorption efficiency can be improved by increasing the height of the water column. Aerosol bubbles are expected to remain longer leading to improved diffusion of nanoparticles from the gas bubbles and increase in concentration in the dispersion medium. Thus, for experiments 21-23, water level was increased to 200ml. It can be seen from the ICP results given in table 3.3 that increase in volume made no difference in concentration.

Table 3.3: ICP results

Exp. No.	Fe (mg/L)
15	5.6
21	7.5
22	4.6
23	1.2

The reason for this is because the yield of the system itself was far too low with the current setup. Also, due to the use of metal mesh as shown in figure 3.5a with larger pore size, the size of the bubbles that were formed were quite large and the number of bubbles were also less. Large bubbles lower the diffusion efficiency of nanoparticles. Majority of nanoparticles are either stuck to the mesh at the base of bubble column or carried away to the exhaust unit without diffusing into water. It can be seen from figure 3.5b that concentration is extremely low even after production duration of 48 hours (Experiment 21).

Bubble size and rise velocity can be controlled by gas flow rate. At low flow rates smaller size bubbles are expected to be formed which provides better surface to volume ratio to diffuse from but having flow rates less than 0.7 l/min results in excessive material accumulation inside the generator. At high flow rates w.r.t the current system i.e., above 3 L/min, one could expect more material to be flushed out of the generator. Then again, neither of these settings improved the concentration. At higher flow rates turbulent flow kicks in and if the water level is higher than 180 ml, the solution overflows from the bubbling column. Thus, 1L/min seems to be a suitable carrier gas flow rate despite the low concentration.

Attempts to lower the bubble size were carried out using a solid stainless steel microbubbler similar to one used by Sharaf with smaller pore size. The pressure build was far too high with the microbubbler which

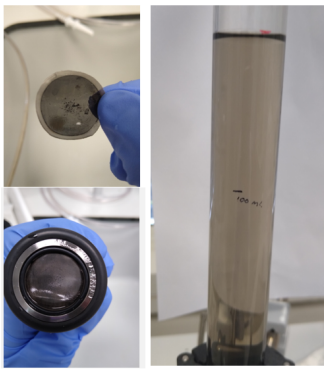

Figure 3.5: a) Capture of nanoparticles in metal mesh (Left) b) Low concentration resulting from use of mesh (Right)

shut down the device after attaining 1.4 bar. Use of multiple stacked meshes to increase number of bubbles was also studied. This lead to increased capture in the layers of 4 meshes as shown in figure 3.6 instead of water. Thus, the use of mesh had to be cast aside.

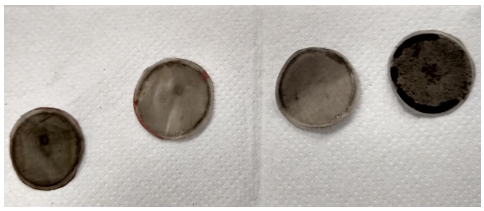

Figure 3.6: Capture of nanoparticles in stacked meshes

Sintered Bronze porous tablet with pore size varying from 4-20 μm as shown in figure was used for experiments conducted hence forth. Based on the results of Thijs Striekwold, it was seen that number and surface to volume ratio of bubbles increased significantly as shown in figure 3.7.

Figure 3.7: Difference in Bubble formation with mesh (Left) and with Bronze tablet (Right) (Reproduced from Striekwold)

No pressure build-up was observed even after continuous production for 5 days. Upon visual analysis, it was concluded that flow rate of 1 L/min produced the highest number of particles that were predominantly

spherical and no turbulence. The capture efficiency and concentration of USPION improved to a great extent just after synthesis duration of 20 hours as shown in figure 3.8. In conclusion, set-points used with the modified setup for the remaining experiments are 1.3 kV, 10 mA and 1 L/min which will henceforth be referred to as standard settings.

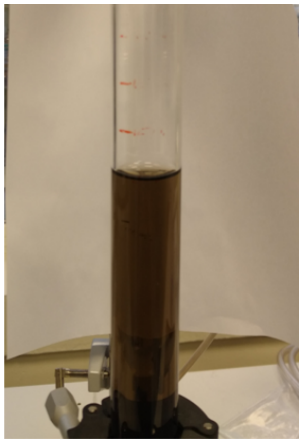

Figure 3.8: Increase in USPION concentration with the use of Bronze porous tablet

3.3. Synthesis of PdO

Before venturing into synthesis of Pd-Fe composite NPs, palladium synthesis experiments were conducted to gain knowledge about the morphology and behavior of Palladium oxide nanoparticles in aqueous media which can later be compared to inter-metallic Pd-Fe (oxide) NPs. Palladium electrodes were subjected to standard set-points for a duration of 19 hours to generate Pd nanoparticles in experiment 24. Majority of the PdO nanoparticles were adhered to glass surface of the bubbling column as shown in figure 3.9. A large amount of deposition was observed on the porous tablet and the remaining PdO NPs suspended in MQ water appeared to have formed large aggregates.

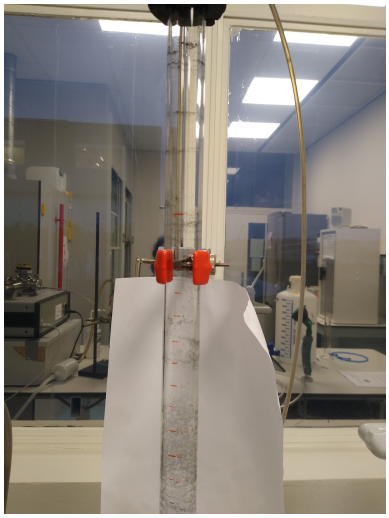

Figure 3.9: Adhesion of Palladium Oxide Nanoparticles to surface of bubbling column

This behavior seemed to be due to charge developed on the surface of PdO. However, to be sure that this phenomenon is only based on nature of PdO nanoparticles, an experiment was conducted to generate US-

PIONs with same settings. There was no deposition observed when iron oxide nanoparticles were generated. Experiments 26 and 27 were a repeat of experiment 24. PdO NPs ended up sticking to external surfaces every time thus, confirming the assumption.

We saw earlier, that if pH is marginally greater or less than IEP, high agglomeration is observed. Based on the concept of ζ potential w.r.t. pH, we know that if the NPs are negatively charged, higher pH will tend to increase the negative charge and there by a larger -ζ potential. If this value lies between 0 to -30mV, then, drastic instability is seen in the system [69]. IEP value of PdO is 4.5 [71]. This implies higher -ζ when suspended in MQ water with a pH of 7. Since the suspension is contantly agitated by the bubbles and gas flow through the bubbling column, the nanoparticles get pushed to the boundaries. Nanoparticles thus seem to get glued to surfaces as a result of electrostatic attraction.

The charge can be neutralized upon lowering the pH of the aqueous media. A 5ml HCl acidic solution of 30% w/v in 50 ml MQ water was prepared. 2-3 drops of this acid was added to the MQ water in the column to lower the pH to 4.5-5 prior to the onset of Pd synthesis in experiment 28. This effectively stopped the adhesion of PdO nanoparticles to the glass. As expected, they did aggregate over time, nevertheless remained suspended in the water. Extremely broad size distribution with peak at 1700nm was measured with DLS after having attained IEP limit. TEM images of PdO nanoparticles primary particle size was deduced to be 4nm.

3.4. Synthesis of PdO-USPION

In experiment 29, Iron electrode was used as cathode and Palladium electrode as anode because low contribution is needed for designing nanoparticles suitable for image-guided thermo-brachytherapy. Primary treatment to be achieved with this theranostic agent is thermal ablation. Thus, we need higher concentration of superparamagnetic USPIONs compared to diamagnetic ultra-small palladium oxide nanoparticles. Brachytherapy with the use of irradiated Pd103 NPs is a secondary treatment which is beyond the scope of this research.

Concentration of PdO-USPIONs appeared to be very high after a generation period of 24 hours. DLS measurements exhibit extremely high count rate reaching upto 1600 kHz. Thus, the measurement had to be stopped for safety purposes. This could mean that either the concentration or the agglomeration is extremely high. DLS measurements of unfiltered samples showed high count rate even at dilution ratios as high as 1:10. Filtering the samples using 400 nm filter lead to extensive capture in the filter and very low count rate with DLS. This proves that the coagulation is enormous with PdO-USPIONs.

3.4.1. Addition of citric acid

Surfactants have proved to lower the aggregation tendency of nanoparticles and ensure stability of the colloid. Majority of the dispersants are known to result in foam formation during functionalization. Given the process of our experiment and bubbling column, excessive foaming and overflow will be a potential issue. Thus, biocompatible citric acid (CA) was considered to be an apt choice so that minimum or no foaming can be expected along with its ability to induce hydrophilic nature into the colloid. Also, since citric acid is a weak acid, moderate concentration will not lead to dissolution of nanoparticles even if they are ultra-small as it is in this case.

Procedure for coating IONPs with citric acid has been mainly via chemical means. Hence, the technique and concentrations had to be adjusted according to the setup. Concentration of IONPs synthesized via co-precipitation are generally in the order of 10-20mg/ml. 10 ml of 0.5g/ml citric acid (50% W/V) solution was added to 50 ml of sample with Fe^{2+} and Fe^{3+} in the ratio of 1:2 and stirred continuously for a period of 60 mins maintaining the temperature at 90^{o}C [72][73]. More details about the addition of hydroxide compounds and

other reagents are omitted here.

Concentrations of Pd-Fe composite nanoparticles obtained from the current set-up is in the order of 30-60 mg/L. Since the yield of our system is far too low, concentration of citric acid was lowered to 0.5% w/v. 0.25g of (99.5%) anhydrous citric acid was added dissolved and MQ water was added gradually until 50ml mark was attained. This 26mM citric acid solution was transferred to bubbling column and same standard settings with iron as cathode and palladium as anode was used for the synthesis. Citric acid solution preparation and functionalization over surface of inter-metallic oxide nanoparticles were all performed at room temperature.

Not only did it limit the aggregation, the absorption efficiency also improved by facilitating the production of large quantity of bubbles with much smaller radius.

Figure 3.10: Difference in bubble formation without (Left) and with citric acid (Right)

10 ml solution of 0.5g/ml of citric acid solution was prepared. However, only 1.5 ml of this solution containing approximately 0.75g of citric acid was added to 50 ml of MQ water. There was a dramatic increase in the amount of small sized bubbles formed in the column as shown in the figure 3.10 and the concentration appeared to be the highest thus far as shown in figure 3.11.

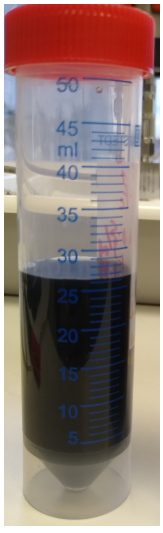

Figure 3.11: Highest concentration of CA capped USPION

At room temperature, density of citric acid (aqueous) solution at concentration of 10% w/w or 1 M/L is 1.1g/cm^3 and viscosity at 6.43% is 1.04mPa.s [74] [75]. Viscosity of water at 293.15K is 0.89mPa.s[75]. Thus, addition of 26mM or 75.8mM in 50ml of water will not vary the viscosity and density by a large extent. Quantitative means of radius estimation depending on the density, viscosity and surface tension can be performed

using equation 3.4 which was also described in section

$$r = 0.5[(\frac{6O_d\sigma_t}{\rho g})^{\frac{4}{3}} + (\frac{81\nu Q}{\pi g}) + (\frac{135Q^2}{4\pi^2 g})^{\frac{4}{5}}]^{\frac{1}{4}} \tag{3.4}$$

Orifice diameter O_d is dependent on the pore size of bronze tablet (4-20 μm), σ_t is the surface tension, ρ is the density, Q is the flow rate and ν is the viscosity. Since there is slight increment in density and viscosity, we can neglect their contribution. However, it is the surface tension that plays a major role. Upon addition of citric acid, the surface tension goes down and it reduces the bubble coalescence frequency [76]. Thus, the bubbles are smaller, slower and more spherical which results in high concentration of citric acid coated - USPIONs. The reason for suppression of aggregation can be attributed to lowered pH which appeared to have improved

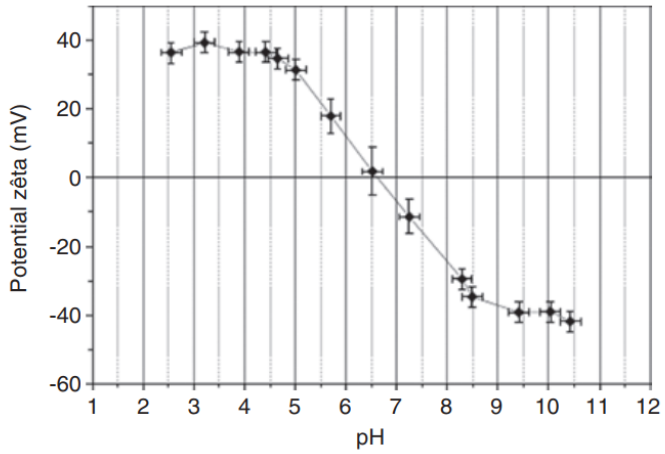

Figure 3.12: Variation in surface charge and ζ potential of IONP w.r.t. pH [68]

the ζ potential and also the stability. The net charge on the naked PdO-USPIONs in water is not known but it can be expected to exhibit near neutral or marginally -ζ given that they formed very large agglomerates in the absence of citric acid but remained suspended in the aqueous media. It can be seen from figure 3.12, ζ value associated with USPIONs increases when pH of the surrounding medium is lowered [69]. Particularly when pH is less than 4 for USPION. Similar behavior could be expected with the PdO-USPIONs in citric acid solution. pH of 26mM CA solution is 2.4 and pH of 75.8mM is 2.15 [3]. High positive charge was created over the composite NPs which increased the repulsive force.

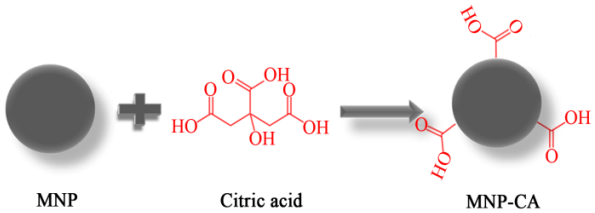

Figure 3.13: CA functionalization over PdO-USPION [73]

The presence of carboxylic groups of CA on the surface of the NPs as shown in figure 3.13 that are exposed to solvent improve the hydrophilic nature of the surface [77].DLS measurements showed very narrow size distribution with low peak. Less aggregation and individual particles were visible on TEM images. There was

[3]Concentration and pH calculations related to citric acid are provided in appendix A

hardly any deposition on the porous tablet due to better absorption efficiency and smaller NP aggregate size as it can be seen from figure 3.14

Figure 3.14: Difference in NP retention in porous tablet without (Left) and with citric acid (Right)

4

Characterization Methods

Brief description of the characterization methods used in the research, measurement steps and sample preparation procedure where necessary is provided in this chapter. The key nanoparticle properties of interest are characterized using techniques presented in table below.

Table 4.1: Characterization Methods

Property	**Technique**
Morphology	DLS, TEM, SEM
Composition	ICP-OES, SEM-EDS, XRD
Crystallinity	XRD
Magnetization	VSM, Mössbauer
Relaxation	NMR
Heating ability	MagneTherm^{TM}

4.1. Morphology

4.1.1. Dynamic Light Scattering (DLS)

Hydrodynamic size of the nanoparticles and size distribution can be detected with DLS. Hydrodynamic size involves the detection of the rate of movement of the outermost diffuse layer which was depicted in figure 3.3. The rate of movement of particles or agglomerates due to Brownian motion is influenced by nature and radius of this layer.

Simplified version of DLS setup is shown in figure 4.1, where a 633 nm HeNe laser beam with a maximum output power of 35mW is projected onto the sample. As the particles continuously diffuse in the aqueous medium at a rate depending on their size, they tend to scatter the incoming laser beam. The intensity of the signal based on scattering is picked up by the Detector. Angle of scattering measured by the system is set at 90^o using AVL Goniometer. Intensity of the signal is measured over a fixed invertal of time during which the intensity fluctuation is autocorrrelated with its original intensity signal with ALV-5000/EPP correlator. At an extremely small step duration (about the order of ns), not much variation in the signal intensity is observed since the particles would have travelled a negligible difference. The diffusion, however changes due to larger displacement over time which alters the signal intensity. Thus, as time progresses the autocorrelation of the new signal with the original signal results in the decay of the correlation signal. This decay rate and rate of

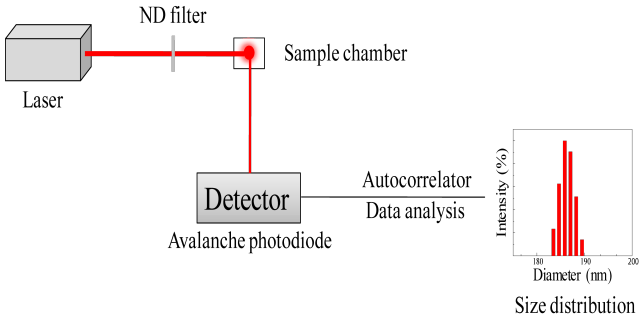

Figure 4.1: Schematic of DLS set-up [78]

intensity fluctuation varies according to the size of the particle. Decay rate is slower with larger particles and steeper with small particles. This decay rate and corresponding size is calculated using ALV-5/6000 software.

The hydrodynamic size is estimated as per equation [78]

$$R_H = \frac{kT}{6\pi\eta D} \tag{4.1}$$

where R_H is the hydrodynamic radius, k is the Boltzmann constant, η is the viscosity of the dispersion medium and D is the diffusion coefficient.

Viscosity of water is applied for the DLS measurements in this work. 2ml of the sample is filtered out using a 400nm filter into the test tube to avoid large foreign particles. The test tubes are wiped with Ethanol and Toluene is that order to remove any fingerprints and to have same refractive index when placed inside the sample holder containing Toluene. In case of high concentration, samples are diluted. Ideal range of count rate for obtaining reliable results are 300-900 kHz. The background measurement tends to be about 13 kHz. Any measurement less than 50 kHz or above 1MHz are unreliable. DLS measurements are reported in section section 5.1.1

4.1.2. Transmission Electron Microscopy (TEM)

TEM images are taken to determine the primary particle size and agglomeration structures. Thermionic-emission electron gun produces thermoelectrons by heating the tungsten cathode filament. Electrons are accelerated through the vacuum tunnel containing a high voltage setup (100-300kV), condenser lens and coil to steer and focus the electron beam using magnetic field and projected onto the specimen. Electrons transmit through the sample and depending on the nature of the specimen and thickness of the material, the intensity of the beam passing through varies which is projected onto a fluorescent screen or converted into an image. It is important to know that bulk materials tend to absorb more and thus result in darker structure.

Jeol JEM-1400 microscope is used to generate TEM images. About 0.2-0.5 μL is dropped on to Quantifoil R1.2/1.3 Cu 300 grid. The sample is allowed to dry up at room temperature. TEM images of various samples are presented in section section 5.1.2

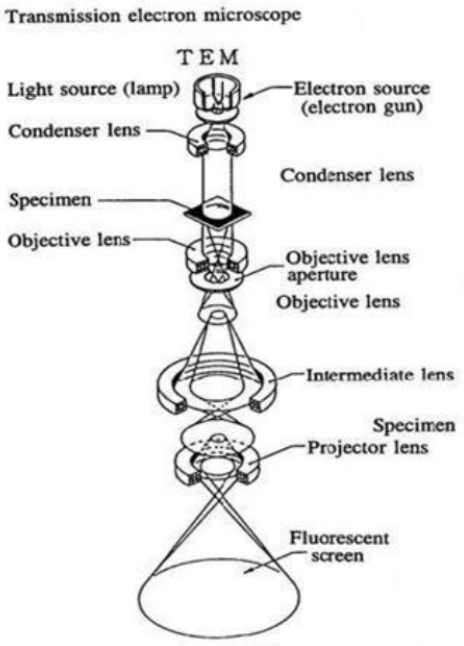

Figure 4.2: Schematic of TEM [79]

4.2. Composition

4.2.1. Inductive Coupled Plasma-Optical Emission Spectroscopy (ICP-OES)

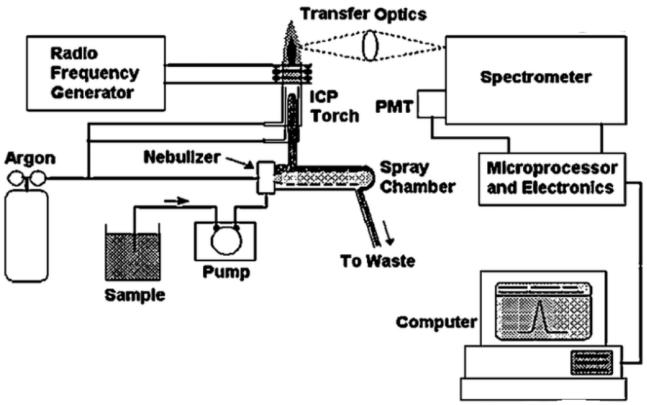

Figure 4.3: Schematic of ICP-OES instrument [80]

ICP-OES is used to measure elemental composition of the synthesized nanoparticles. This technique exploits the absorption and emission principle associated with atoms and ions of the material of interest. According to the schematic of ICP-OES system in figure 4.6, the sample is subjected to nebulization in nebulizer unit i.e., the sample in liquid form is converted to an aerosol using Argon gas/ mist which is transported to ICP torch and further into the medium containing plasma. RF coil connected to RF generator is wound around the tail of the ICP-torch. Alternating current flows through the coil leading to generation of EM fields within the torch region. Ar gas is released through ICP torch and a spark is generated resulting in stripping of electrons from atoms of Argon, further collisions, excitations, ionizations and a chain reaction leading to plasma generation. The aerosol sample is subjected excitations of atoms and ions due to high temperature and charge carriers in plasma. Both the atoms and ions of the material of interest and plasma reverts back

to ground state via photon emission. The intensity of this bright emission light is recorded with the use of PMT and processing unit. Every material has a characteristic wavelength associated with the emission and spectrometer is used to differentiate the wavelength and thereby differentiating the different elements in the sample [80].

To perform quantitative measurements, samples are subjected to acid digestion in order to breakdown the analyte. 1.5ml of Nitric acid (HNO_3) is added to 10 ml of sample. Palladium does not dissolve as readily as Iron in HNO_3. Thus, the samples Pd-Fe composites had be pre-heated in microwave to ease the disintegration process. In order to determine the concentration of the respective elements, stock solutions for calibrating the system ought to be performed. Stock solution consists of liquid samples with known concentration of the analyt. The intensity corresponding to different concentrations are determined to generate a calibration line which can be referred to in Appendix A. The detection limit with ICP-OES is in the order of 1μg/L.

In this work, PerkinElmer Optima 5300 was used to perform ICP-OES measurements. Intensity corresponding to samples were plotted against the calibration line to determine the concentration. In order to estimate the concentration required for calibration, 10 ml samples with and without citric acid were freeze dried. Additional, liquid samples were also measured. The results of the analysis are provided in section 5.2.1

4.2.2. X-ray Diffraction (XRD)

XRD is generally used to study the crystalline structure of nanoparticles preferably in powder form. Sample exposed to X-ray beam diffracts in a particular direction. X-rays are used because the wavelength is comparable to atomic size and distance between atoms. Range of angles over which the x-ray beam is diffracted and the corresponding intensity is measured which provides information about crystal structure. Composition can be determined since every element has a distinct diffraction pattern. One must bear in mind that extremely fine particles could cause broadening of peaks and low intensity.

In this research, about 5mg of Iron and Pd-Iron nanopowder, residue from the generator was used for conducting XRD measurements with PANalytical XPERT-PRO diffractormeter. This was primarily done becuase the yield from each experiment was generally low and the nanoparticles generated from addition of citric acid got clumped together into one solid mass due to excess citric acid after freeze drying the samples. Monochromator is used to avoid fluorescence upon exposure of Fe to Cu X-rays. The measuemnents are performed at angles ranage from 10 to 90^o for a duration of 8 hours. Results of these measurements can be seen in section 5.2.2

4.2.3. Scanning Electron Microscopy- Energy-Dispersive X-ray spectroscopy (SEM-EDS)

Similar to TEM microscopy system, SEM uses electron gun to produce electron beam that irradiates the specimen. The microscopy technique is pretty much like light microscopy except that we can get higher resolution due to use of electrons and wavelengnths of corresponding order. The voltage applied to accelerate electrons are far lesser compared to TEM (1 to 30kV). The main difference between SEM and TEM is that SEM records the beam scattering off the surface of nanoparticles. Depending on the density of the material and scattering angle, a contrast map and image is generated. In this work, JEOL JSM-IT100 SEM instrument is used whose schematic is depicted in figure 4.4. 0.5-1 μL is dropped on to a carbon tape glued to a gold stub. The samples are allowed to dry up over night to perform SEM imaging [81].

EDS is used to determine the elemental composition in the sample sample and elemental mapping is performed to know about the distribution of specific elements in the nanoalloy, the results of which can be seen in section section 5.2.3 [81].

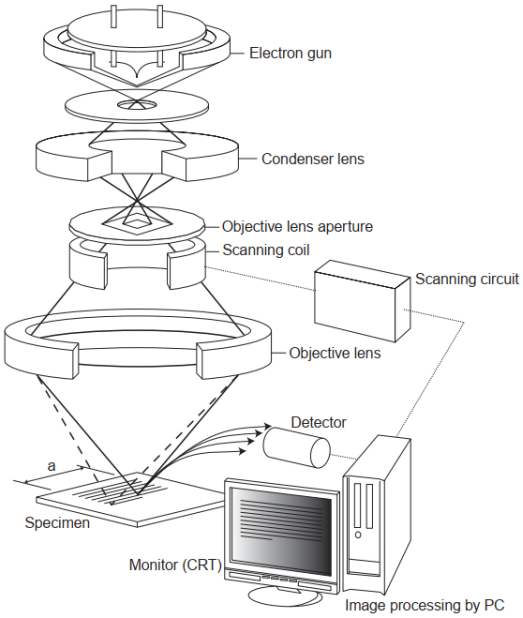

Figure 4.4: Schematic of SEM [81]

4.3. Heating Power measurement

Ability of USPIONs and PdO-USPIONs to generate heat when subjected to Alternating Magnetic Field (AMF) as described in section was investigated using MagneTherm^{TM} device. Nanoparticles could be subjected to wide range of frequencies from 50 kHz – 730 kHz and a highest field strength of 20 kA/m (25 mT). However, keeping the clinically relevant threshold values in mind, 1ml samples were placed in the hollow induction coil in the device with inducing a frequency of 250kHz and 23 mT for a duration of nearly 7 mins. Water maintained at 20^{o}C was used as a coolant to prevent the coil and device from overheating. Measurements were performed only on naked USPION and PdO-USPION samples and not the samples with citric acid due to unavailability of device. The measurement is given in section 5.3

4.4. Magnetization

4.4.1. Vibrating Sample Magnetometer (VSM)

VMS works on the principle of electromagnetic induction. Two temporary electro-magnets are connected to the power supply which develops polarity in the two magnets. When the power supply is tuned on, they generate a strong magnetic field. Water is used to cool the electromagnets. Four pick up coils are used in the system and the sample is placed at the center. If the material subjected to the field is magnetic, magnetization can be induced when exposed to the field. 1-2mg of sample is used for measurement and placed close to the magnetometer which will measure the induced magnetic moment. Quantum Design Versalab VSM device is used to obtain magnetization measurements. Magnetic field up to 3T can be generated by applied nearly 20A current to the electromagnets with this device. De-Gauss is performed to demagnetize and simultaneously apply opposing magnetic field ±3T (±30000 Oe). Measurements were conducted at 300K. For the same reasons measured in section 4.2.2, nanopowder residue from generator is used for obtaining M-B curves which are shown in section 5.4.1 [82].

4.4.2. Mössbauer Spectroscopy

Mössbauer spectroscopy works on Mössbauer effect, which encompasses recoil-free, resonant absorption and emission of γ radiation by atoms in material of interest. If there is no resonant condition mainatined in thesystem i.e., ceratin amount of absorbance will come into play. Thus, the source as to be moved to a location further away of near to the target so that recoil-free resonance condition is reestablished. These absorbance and transitions result in dip in the spectrum. Isomer Shift represents valence state depending on e^- charge density at the nucleus; Quadrapole splitting is based on interaction of interaction of material with electric field due to asymmetry in the electron configuration which is typical for suerparamagnets; and the Hyperfine magnetic field deals with the magnetic state of nanoparticles. These three form the key parameters of Mössbauer. Magnetic phase of components of iron in sample can be determined by this technique

Transmission ^{57}Fe Mössbauer spectra were collected at 300 K with a conventional constant-acceleration spectrometer using a ^{57}Co(Rh) source. Velocity calibration was carried out using an α-Fe foil. The Mössbauer spectra were fitted using the Mosswinn 4.0 program. Mössbauer requires 50mg of material. Such large quantity could be obtained only by combing material from different experiments. For USPIONs, samples from 4 experiments conducted with same setting for same duration was used and for PdO-USPIONs, 3 samples were used. Assumption made here is that the material properties are expected to remain same when similar settings were used. The spectroscopy results are given in section 5.4.3.

4.5. Relaxation Measurements

Ability of USPIONs and PdO-USPIONs to function as contrast agents is examined through Nuclear Magnetic Resonance (NMR) measurements. Magnetization recovery (T_1) along the longitudinal axis (M_z) cannot to be measured directly because it is a static process and does not induce alternating current like T_2 in the RF coil. Thus, to calculate M_z during T_1 recovery, traditionally two α pulses separated by an interval. Longer the interval, higher will be magnitude of component flipped into transverse plane. However, this is a tedious process and the system is often subjected to RF field inhomogenieties. Thus, inversion pulse trick represented by the pulse sequence diagram 4.5 is applied to ensure better signal and limit the steps. 180^o pulse is applied initially and magnetization is allowed to recover along z-axis and then a 90^o α pulse is applied to flip the recovered signal into XY plane which induces AC in the coil that provides the rate of T_1 Relaxation.

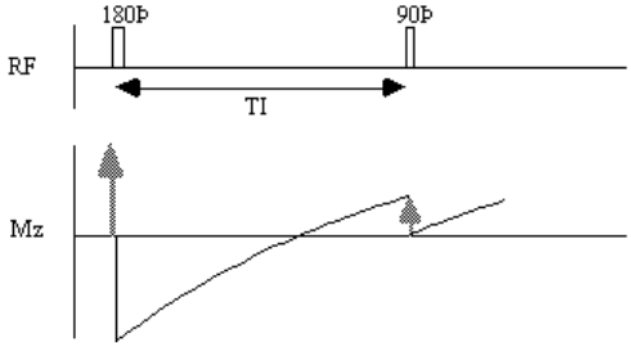

Figure 4.5: T1 inversion recovery pulse sequence

Carr-Purcell-Meiboom-Gill (CPMG) sequence [83] involves application of 90^o alpha pulse which induces free induction decay (FID) and four consequent 180^o spin echoes which shown reduction in magnitude of signal over time as a result of T_2 effect. CPMG sequence diagram is shown below.

Relaxation measurements were performed using Agilent NMR spectrometer. Static Magnetic field of 9.4T at 400 MHz was applied to the samples. Relation between measured intensity of signal and relaxation time is

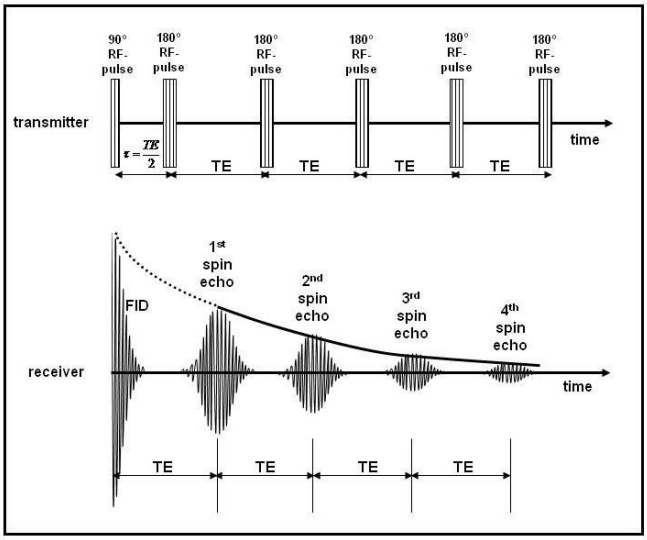

Figure 4.6: CPMG sequence

given by equation

$$Y' = B + F * exp(-X * G) \tag{4.2}$$

where G is the Relaxation time depending on whether it is T_1 or T_2 signal. Relaxivities can be calculated as per equation .

USPION (Fe-Fe) sample, samples from experiment 30 comprising of naked PdO-USPIONs (Pd-Fe), and experiment 31 also comprising of PdO-USPIONs (Pd-Fe) which were produced by reversing the electrodes (Pd as cathode and Fe as Anode), experiment 32 that involved addition of 26mM CA to generate CA coated PdO-USPIONs and experiment 33 which also produced CA capped PdO-USPIONs 75.8mM of highest concentration. 5ml of 0.5% w/v of Xanthan was centrifuged to create a homogeneous solution. Since the naked Nanoparticles have been proven to result in large agglomeration, Xanthan had to be added to the samples in the ratio of 1:4 to prevent further agglomeration. 1.6ml of Xanthan was added to 400 μL of naked PdO-USPION and 800 μL of CA capped Pd-USPIONs corresponding to exp. 32 and 33 were measured without Xanthan. Contrast agent behavior of these NPs is realized in section section 5.4.2

5

Results and Discussion

This chapter presents the results of characterization of PdO-USPIONs and USPIONs for comparison. Only key results are given in this section.

5.1. Morphology

5.1.1. Dynamic Light Scattering (DLS)

The size distribution measurement was performed on PdO nanoparticles after adjusting the pH of the water in accordance with the IEP value of PdO. It can be seen from figure 5.1a, that the size distribution is large as a result of agglomeration with the highest peak at 204 nm. Similar behavior is observed with USPIONs in figure 5.1b, except that they form relatively smaller agglomerates compared to PdO which is attributed to larger negative charge on palladium oxide NPs. Only hydrodynamic size (R_H) can be known through DLS as it is dependent on the movement of the diffuse layer around the nanoparticle. Thus, the low peak at 10nm for PdO and 9.3nm for USPION is due to combination of layer of hydroxyl and proton groups around the nanoparticle combined with extremely small aggregates. As mentioned in section 3.2, sample containing

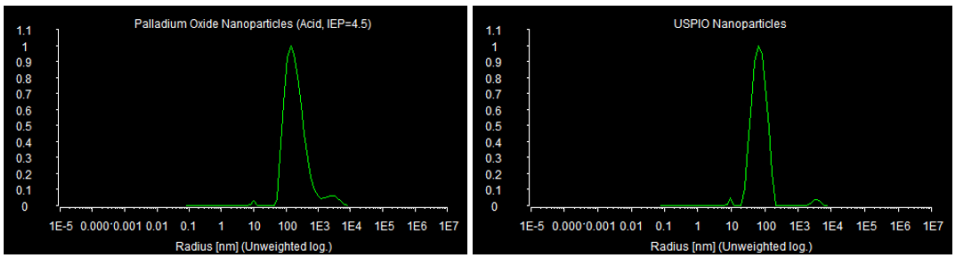

Figure 5.1: DLS measurement of a) PdO Nanoparticles (Left) and b) USPION (Right) [V=1.3kV, I=10mA, Q=1L/min]

USPIONs with hydrodynamic radius of 11.65nm and 69.6nm changed into one peak at 2172 nm as seen in the distributions given below.

Typically, viscosity value of the solvent is incorporated into the system when calculating R_H. However, as a consequence of low concentration of citric acid being added to water, no significant difference in viscosity is observed which would reflected onto R_H. Hence, viscosity of water is used for estimation. Even after diluting the sample in the ratio of 1:10, very broad distribution with peaks at 25 and 759 nm corresponding to "naked"

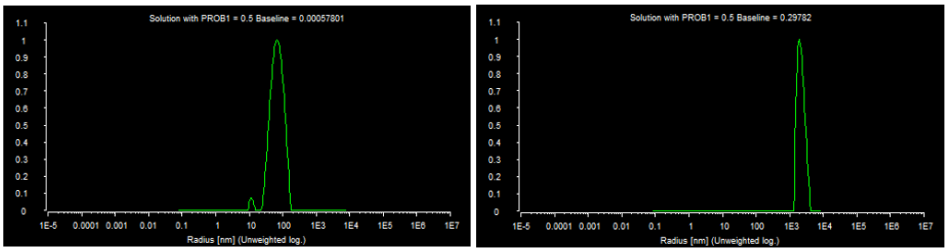

Figure 5.2: Agglomeration of USPIONs in 4 days [V=1kV, I=7mA, Q=2L/min]

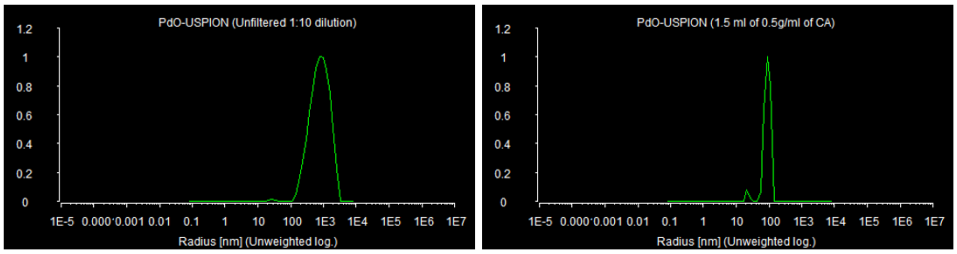

Figure 5.3: DLS measurement of a)Naked PdO-USPIONs and b) CA capped PdO-USPIONs [V=1.3kV, I=10mA, Q=1L/min]

PdO-USPION can be observed in figure 5.3a due to extensive aggregation. On the other hand figure 5.3b shows extremely narrow distribution with peaks at 22 and 89nm which is also confirmed from figure 5.4. Most of the naked PdO-USPION nanoparticles were captured on the filter and so, only unfiltered samples had to be used for DLS. But, with CA coated PdO-USPIONs, almost all of it could be filtered out for collection and measurement.

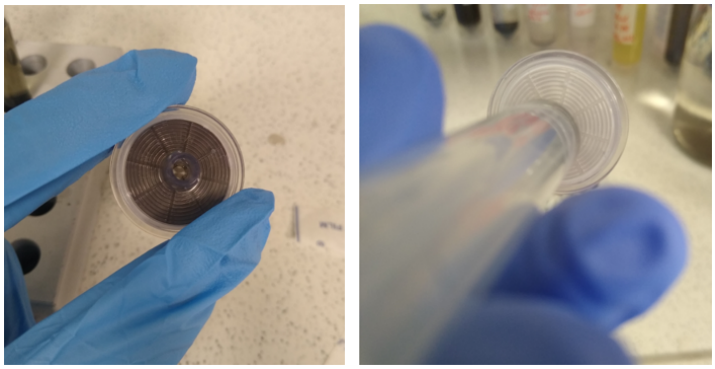

Figure 5.4: Difference in Nanoparticle capture on 400nm filter a) without and b) with CA

5.1.2. Transmission Electron Microscopy (TEM)

Primary particle size and shape of nanoparticles are determined via TEM images [1]. As mentioned in chapter 2, atomic clusters coalesce to form spherical particles because spherical structures exhibit low potential energy due to lowest surface area compared to other shapes as can be seen from images of nanoparticles below. To find the average particle size, couple of spheres marked with yellow lines were measured manually and estimated according to the scale at which the image was captured. Primary particle size of palladium oxide nanoparticles is 4nm and that of Iron oxide nanoparticle is 5nm.

CA capped PdO-USPIONs appear to be well dispersed, coated and very small structures in case of aggre-

[1] All TEM images, sizes and marked features are not subject to scale. Particle size estimations are performed on original image files.

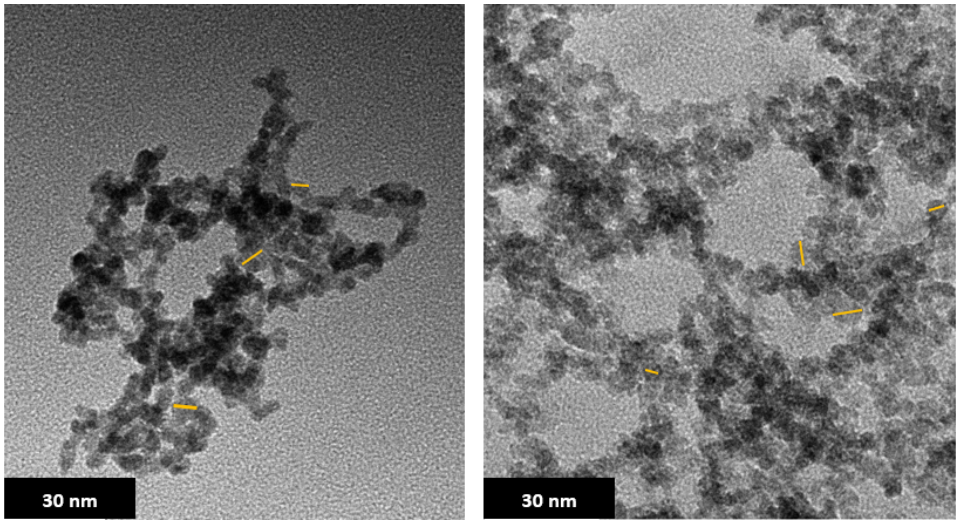

Figure 5.5: TEM image of a) PdO nanoparticles of 4nm (Left) and b) USPION of 5nm (Right)

gation which can be observed from figure 5.6b. It must also be noted that there was no indication of reduction in primary particle size due to CA. As a result of joule heating and the discharge channel that forms between

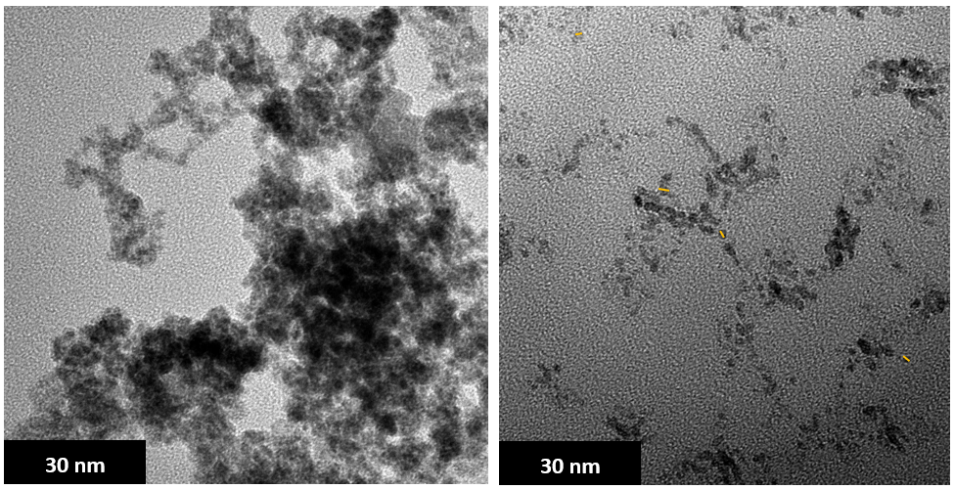

Figure 5.6: TEM image of a) Naked PdO-USPION (Left) and b) CA coated PdO-USPION (Right)

the electrodes, the material at the point of contact forms molten craters. When discharge event ceases, a recoil force is experienced by the molten material. If this force dominates the surface tension, the material is ejected leading to formation of pure elemental bulk material. Outcome of this can be witnessed in figure 5.7 and the mechanism is pictorially represented in 5.8 [20]. Large Iron particles contribute to ferromagnetic behavior. Large structures of palladium and iron appear to be darker due to increased electron beam absorption. Nevertheless, they still form a small percentage of the produced material.

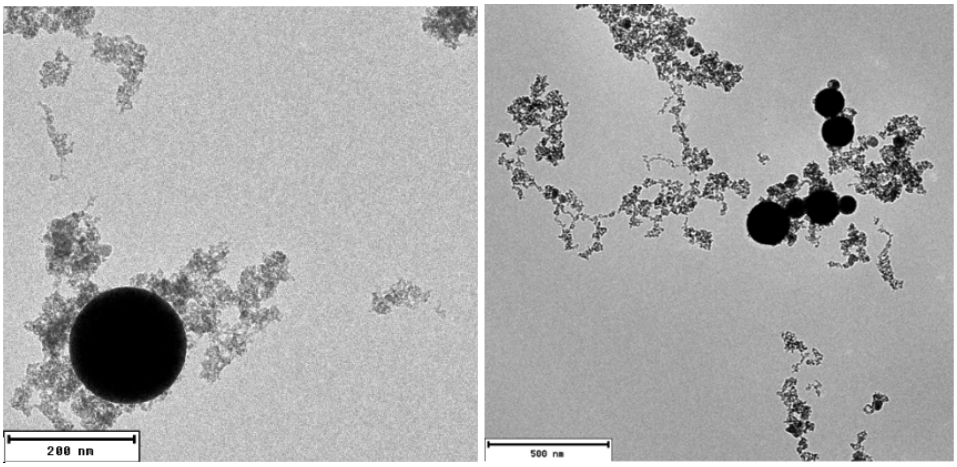

Figure 5.7: Splashed bulk particles a) 263 nm (Left) and b) 175,100,75,25 nm (Right)

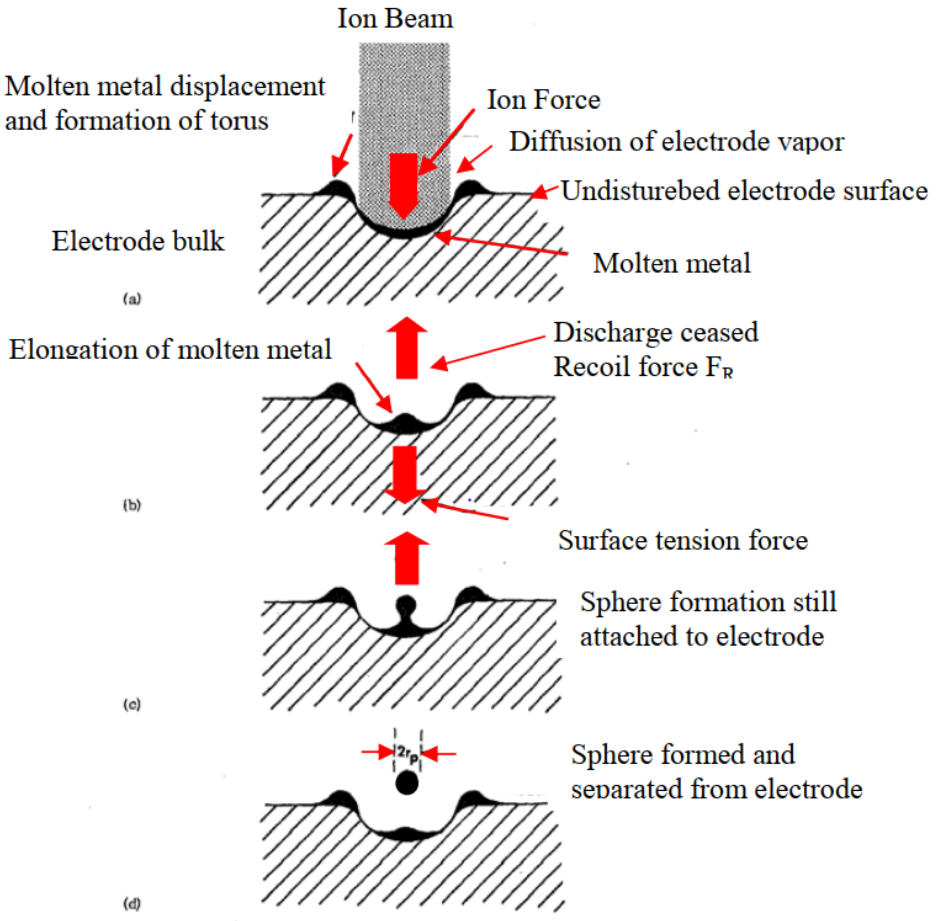

Figure 5.8: Mechanism of Bulk material formation [20]

5.2. Composition

5.2.1. Inductive Coupled Plasma-Optical Emission Spectroscopy (ICP-OES)

Samples from experiment 30,32 and 33 were subjected to freeze drying to get an estimate of the quantity being generated. However, after freeze drying, the specimens appeared to have coagulated and formed clumps. They were stuck to the surface of falcon tubes and significant material was lost which scraping them out.

Despite that, the % concentration of Fe and Pd in the samples seem to be too low. The details concerning concentrations are provided in table 5.1. Only 1.5% of Fe and 0.91% of Pd was present in the sample with CA which was expected to have the highest concentration. The remaining amount is assumed to be related to oxygen and excess of citric acid. The ratios also seem to be off compared to the concentrations detected with Nanoparticle solutions, particularly, result of exp. 30 with an very high error. Thus, ICP performed directly on microwave and acid destructed nanoparticle solutions tabulated below are considered to be more reliable results which are further used for relaxivity measurements with NMR. The concentration from experiment 32 with the use of 26mM CA is less than one would estimate because unlike other experiments that ran for a duration of 22-24 hours, production duration was only 16.5-17 hours.

Table 5.1: ICP results of PdO-USPION

Freeze Dried Samples [10ml of 50ml sample]	**Total Amount [mg]**	**Fe [mg/L]**	**Pd [mg/L]**	**Concentration [mmol/L]**
Exp. 30 [Naked]	0.4	400µg/L (1%wt)	180µg/L (0.47%wt)	8.6µmol/L
Exp. 32 CA (26mM)	22	15.4 (0.70%wt)	8.14 (0.37%wt)	0.35
Exp. 33 CA (75.8mM)	45.9	69 (1.5%wt)	41.4 (0.91%wt)	1.619
Nanoparticle Solutions		**Fe [mg/L]**	**Pd [mg/L]**	**Concentration [mmol/L]**
Exp. 30		19	18	0.469
Exp. 31 (Electrode Reversal)		25	26	0.6
Exp. 32		32	14	0.702
Exp. 33		118	44	2.5

The concentration of PdO-USPION has improved from 0.469 mmol/L to 2.5mmol/L, albeit marginally. Despite all the optimizations performed on the setup, the nanoparticles reaching the bubbling column and getting deposited appears to be still quite low.

5.2.2. X-ray Diffraction (XRD)

XRD measurement for USPION as per figure 5.9 indicates the presence of Magnetite alone. However, it can be seen from Mossbauer results that more than one oxidation state is present in the sample. No defined crystallinity was determined No oxidation of Fe-Pd or Pd nanoparticles are determined by XRD. 4.5mg of material used for conducting measurements was a residue sample from the generator and not the particles collected in bubbling column. Thus, one possible explanation could be is the presence of bulk material since the % contribution of large particles tend to increase as the electrode depletes. The X-rays could have been scattered to large extent by bulk material. The oxidation rate of Pd upon exposure to air is less. Another key reason is that, all the peak detections are performed by fitting the data to the results in the database of the XRD system used. Thus, the results are subjected to the pre-existing information too. Some of the crucial aspects to note is that the background is too high in case of both Iron and Iron-Palladium measurements. This cannot be attributed to fluorescence because of Cu and Fe since Monochromator was used to suppress the effect. Reliable information pertaining to composition and crystal structure can be obtained with XRD when particles are above 10nm. Since, the samples contain either aggregates of ultra-small nanoparticles of 5nm or extremely large bulk particles. No defined crystal structure was derived from the data.

5.2.3. Scanning Electron Microscopy- Energy-Dispersive X-ray spectroscopy (SEM-EDS)

To get an understanding about the surface of the nanoparticles and elemental distribution in the alloy, SEM-EDS is performed. Sample preparation involved drying of 0.5ml of the sample as described in section 4.2.3. Similar to the freeze dried samples used for ICP, an agglomerated structure was formed at the center of the

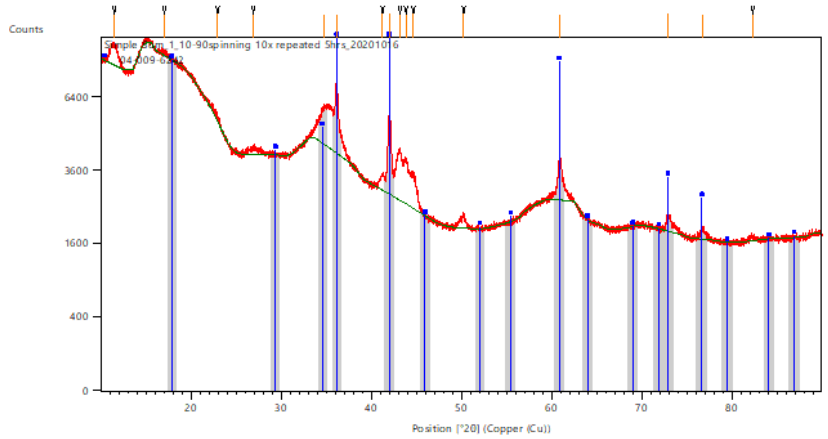

Visible	Ref. Code	Score	Compound Name	Displ.[°2θ]	Scale Fac.	Chem. Formula
■	04-009-6242	63	Iron Oxide	0,000	1,041	Fe3.776 O4

Figure 5.9: XRD Measurement of Iron Nanopowder from generator

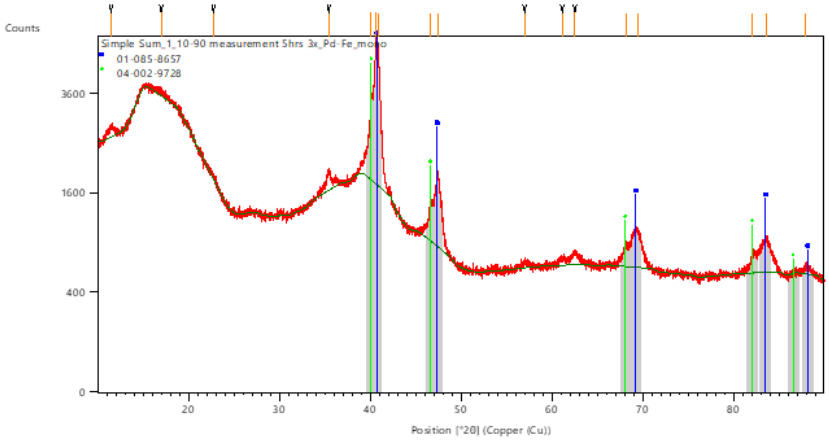

Visible	Ref. Code	Score	Compound Name	Displ.[°2θ]	Scale Fac.	Chem. Formula
■	01-085-8657	62	Iron Palladium	0,000	0,876	Fe Pd3
●	04-002-9728	61	Palladium	0,000	0,500	Pd

Figure 5.10: XRD Measurement of Palladium-Iron Nanopowder from generator

carbon tape and surface of the combined particles appeared to be fractured and of irregular shapes. One region of the agglomerate containing a bulk particle is displayed in figure 5.11. TEM image of Bulk material is only provided for reader's reference. It is not from the same sample.

After performing elemental mapping with the application of EDS, the large spherical structure attached to a surface on the agglomerate was confirmed to be Palladium. We can clearly see lack of oxygen, carbon and Iron at the location of bulk palladium structure. This is because the ease and rate of oxidation reduces as the size increases and attains bulk structure. Bulk metallic palladium is far more oxygen resistant compared to Iron [84][85].

High concentration of Palladium compared to Iron in the sample despite the use of Fe as cathode and Iron as anode is due to the presence of pure palladium particle. Increment in the concentration of Iron can

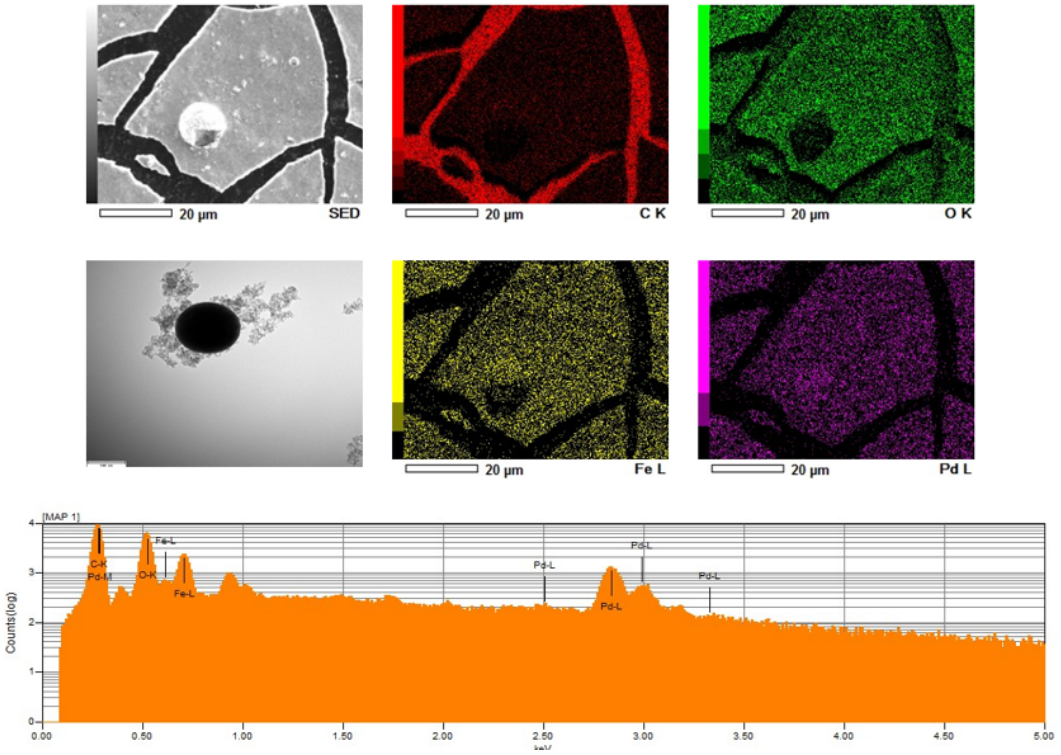

Figure 5.11: SEM-EDS of Pd) USPION sample

be seen upon use of citric acid. It must be noted that these results are specific to the sample in question.

Table 5.2: SEM-EDS measurements of Mass % of Constituent Elements

Material	Pd mass%	Fe mass%	O mass%
PdO-USPION	26.64	21.26	25.69
CA capped PdO-USPION	23.72	37.37	23.18

5.3. Heating Power Measurement

"Bare" USPIONs and PdO-USPIONs were subjected to 23mT AMF at 250kHz for a duration of 5-7 mins. Neither of the MNPs exhibited any heating ability. The increase in temperature from 23 ^{o}C to 24 ^{o}C PdO-USPION was observed at the consequent iteration. Inability of these particles to heat up is due to large agglomerations which have varied sizes and orientations of nanoparticles attached together. They tend to influence each other. We know from Neel relaxation and linear response theory that nanoparticles tend to exhibit high Specific Loss Power (SLP) depending on anisotropy and size of the individual particle. For a certain size which corresponds to Neel relaxation time, at a specific resonant frequency, SLP will reach its peak value resulting in heat generation. This however cannot be achieved if the nanoparticles are not monodispersed or are in a particular arrangement which increases anisotropy. Additionally, with ultra-small nanoparticles, large percentage of atoms are on the surface which form a magnetically dead layer due to spin canting.

Ultra-small MNPs tend to be highly unstable due to large surface to volume ratio. If one is aiming for heat generation with PdO-USPIONs, it is crucial to get them to be as well dispersed as possible. The concentration is also considerably low which also needs to be attended to. Thermal measurements could not be performed on CA capped PdO-USPIONs due to unavailability of the device by the time they were synthesized. However, from multiple other TEM images, it was observed that agglomerates of moderately large sizes were also

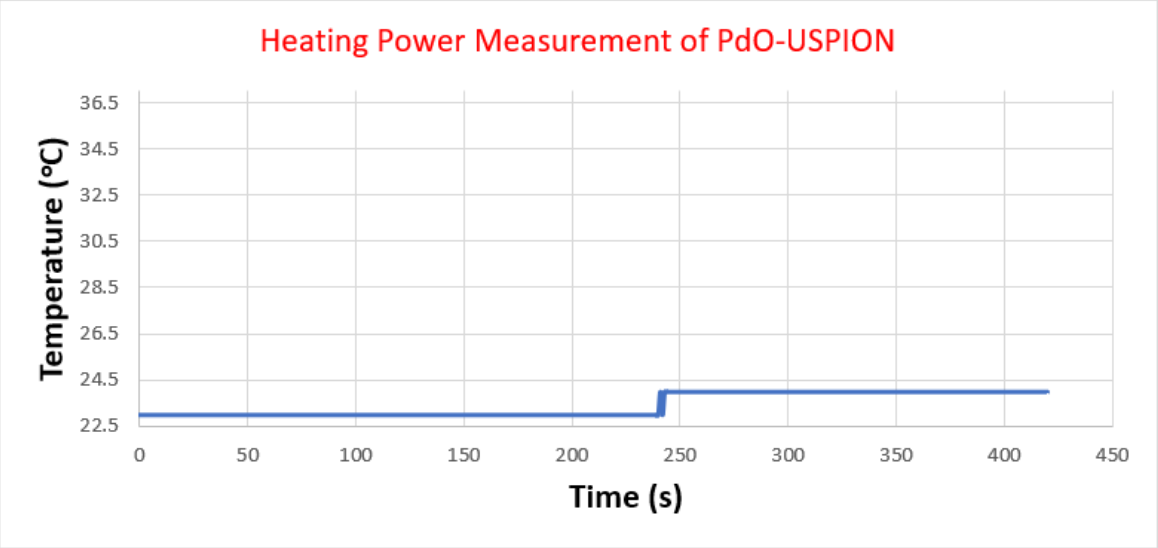

Figure 5.12: Heating performance of PdO-USPIONs when subjected to AMF

formed even through the number of monodisperse and small agglomerates were on a higher side. Not all particles or aggregates could be expected to be well coated at room temperature. Thus, there would have been less probability of them heating up either, not to mention, the concentration is still low.

5.4. Magnetic Measurements

5.4.1. Vibrating Sample Magnetometer (VSM)

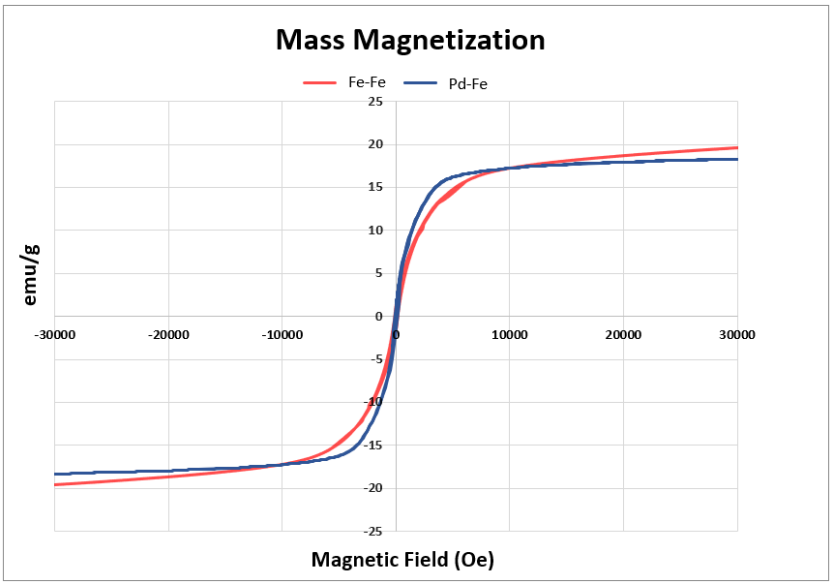

Figure 5.13: Mass Magnetization of Fe and Pd-Fe Nanoparticles

Samples that are freeze dried is not suitable for performing M-H measurements since samples in powder form as most preferable. Thus, 1.07mg of Iron Oxide and 1.47 mg of Pd-Iron oxide nanopowder from generator is used. The assumption behind using the sample from generator is that they do not significantly vary from the nanoparticles captured in water. Upon exposure to air, iron nanoparticles in the generator tend to

readily oxidize and so does palladium provided they are fine nanoparticles and not large metallic particles. The samples could have larger agglomerates and slightly higher concentration of bulk metallic particles but in the essence, has nearly same composition, structure and magnetic behavior.

From Mass magnetization measurement, it can be deduced that both Fe-Fe (oxide) and Pd-Fe (oxide) nanoparticles exhibit superparamagnetic behavior due to lack of coercivity, remnance and therefore absence of hysteresis loop. The absence of hysteresis loop in these measurements are also an indication of absence of bulk ferromagnetic structures in the sample. Thus, the results can be used as a representation of magnetization values of nanoparticles from solution. The magnetic behavior and magnetic saturation value being 16 emu/g for both the samples implies that palladium nanoparticles do not alter the magneto-crystal structure and anisotropy. Low magnetic saturation is the result of spin disorder effect observed in ultra-small magnetic nanoparticles. It is prudent to bear in mind that the ratio of Fe/Pd is not known for this specific sample and the variations in settings resulting in increase in palladium could alter the structure.

5.4.2. Relaxation Measurements

Table 5.3: NMR Measurements

Experiment	**Concentration [mmol/L]**	**R_1 [s^{-1}]**	**R_2 [s^{-1}]**	**r_1 [L/mmol*s]**	**r_2 [L/mmol*s]**	**r_2/r_1**
30 (Xanthan)	0.469	0.3733	1.978	0.043	1.8	41.86
31 (Xanthan)	0.6	0.3723	2.151	0.0335	1.69	50.44
32	0.702	4.501	9.101	5.86	12.4	2.12
33	2.5	4.767	8.289	1.75	3.159	1.8
Fe-Fe	0.41	0.34	3.06	0.053	0.79	14.9

"Bare" PdO-USPIONs from experiment 30 and 31 resulted in very large agglomerates. To prevent further coagulation and sedimentation of the particles, Xanthan has been used. Local field inhomogenieties introduced by PdO-USPIONs increase with increase in agglomeration because of high variation in the orientation and magnitude of the magnetic moments arising from clustered nanoparticles. This results in enhanced dephasing of water protons around the particles. Therefore the effect of relaxation is more pronounced with T_2 than T_1. Thus, nanoparticle aggregates in E30 and E31 exhibit high r_2/r_1 ratio functioning as T_2 contrast agents. R_2 is higher in case of sample 31 in comparison to 30 because of increase concentration of Pd due to switching of electrodes which implies larger agglomerates due to higher instability of PdO nanoparticles in water and thus higher inhomogenieties arising from USPIONs in the sample. This is also the reason why the ratio of r_2/r_1 is less with USPIONs with smaller aggregation sizes than with PdO-USPIONs.

Whereas CA coated PdO-USPIONs appear to be well dispersed with very small or no agglomeration to certain extent which increases R_1 relaxation rate. (Nearly) Monodisperse magnetic nanoparticles less than 10nm have been studied and proven to function as T_1 contrast agents. Low magnetic saturation induces weaker fields locally and availability of large unbound atoms that act as proton exchange sites at the surface of Ultra-small MNPs improve T_1 relaxation and r_2/r_1 tends to be in the ratio of 1-2. Thus, samples from 32 and 33 function with as T_1 contrast agents. As expected, exp 33 with higher concentration of citric acid and more dispersion probability, higher R_1 is observed relative to exp 32. The calculations are provided in appendix A

5.4.3. Mössbauer Spectroscopy

As described in section 4.4.2, the measurements obtained with the Fe oxide samples from the generator is a contribution from 4 samples and spectrum was fitted with contributions from magnetite contributing to ferromagnetic behavior (5%), an intermediate reduction species Fe^{2+} (most likely wüstite-FeO) which exhibits

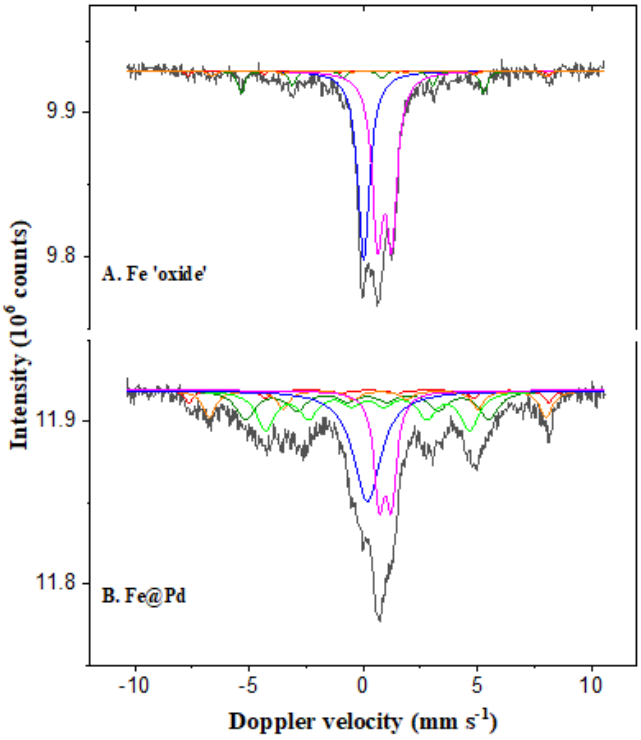

Mössbauer spectra obtained at 300 K with the Fe and Pd-Fe samples.

The Mössbauer fitted parameters of the Fe and Pd-Fe Pd samples

Sample	*IS* ($mm{\cdot}s^{-1}$)	*QS* ($mm{\cdot}s^{-1}$)	*Hyperfine field (T)*	*Γ* ($mm{\cdot}s^{-1}$)	*Phase*	*Spectral contribution (%)*
Fe	0.02	-	-	0.63	Fe^0 (SPM)[a]	34
"oxide"	0.00	-	33.0	0.37	Fe^0	10
	0.94	0.62	-	0.57	Fe^{2+}	51
	0.25	0.01	49.1	0.30	Fe^{3+} Fe_3O_4, A)	2
	0.69	0.00	45.5	0.45	$Fe^{2.5+}$ (Fe_3O_4, B)	3
Fe@Pd	0.18	-	-	1.46	Fe-Pd alloy[b] (SPM)	25
	0.18	-	33.1	1.00	Fe-Pd alloy[c]	18
	0.20	-	27.8	0.97	Fe-Pd alloy[d]	24
	0.97	0.53	-	0.55	Fe^{2+}	18
	0.25	0.01	49.0	0.45	Fe^{3+} (Fe_3O_4, A)	4
	0.69	-0.10	45.9	0.66	$Fe^{2.5+}$ (Fe_3O_4, B)	11

Experimental uncertainties: Isomer shift: I.S. ± 0.02 mm s^{-1}; Quadrupole splitting: Q.S. ± 0.02 mm s^{-1}; Line width: Γ ± 0.03 mm s^{-1}; Hyperfine field: ± 0.1 T; Spectral contribution: ± 3%; [a]Very small (<15nm) structures, superparamagnetic at room temperature; [b,c,d]Fe-Pd alloys with various Fe/Pd ratios.

Figure 5.14: Mössbauer Measurements

paramagnetic behavior and metallic Fe – bulk structures (10%) and very small superparamagnetic species (34%). Sextets provide information about the ferromagnetic spectral contribution (green and yellow). Contribution of superparamagnetic particles can be identified from the doublet in the spectrum (Pink).

The spectrum obtained with the Fe-Pd sample contained signal from Fe-Pd alloy species (small and bulk) with different Pd content. Zhang et al., [86] observed that in in $Fe_{1-x}Pd_x$ alloys, if x<0.6, ferromagnetic behavior was dominant and for larger x, paramagnetic nature was dominant, particularly with x>0.85. Mixed valence states and magnetic phases were observed for ratios in between. This behavior cannot be directly translated to PdO-USPION nanoparticles because the Pd/Fe ratios are not known and the crystal structure is

not defined too. The 3 mixed samples of Pd-Fe oxide nanoparticles appear to be synthesizing material with mixed ratios, oxidation states and magnetic behavior. Take away from the work of is that more Pd is present – the smaller the measured hyperfine field value which correlates with the results given in the figure 5.14. 25% of Fe-Pd alloy with a specific ratio tends to exhibit superparamagnetism. Fe-Pd alloys c,d are classified based on the hyperfine field, 18% is paramagnetic Fe^{2+} and the rest correspond to moderate magnetite and wüstite signals in this sample.

The results do not appear to be promising but it certainly helped to know different oxides and possibility of generating a Fe-Pd with specific setpoints to increase SPM contribution. This can be known only by increasing the yield of the system and synthesizing over long period of time so that a single sample can be used for Mössbauer which reduces the number of variables. Further, a more sensitive, accurate and non-destructive neutron activation analysis should be performed over sample to get precise information about composition and ratio without having to lose the material. XPS or HR-XRD or XRD with more accurate details must be used to know about the precise crystallinity of the Pd-Fe (oxide) alloys. Specimens generated through these ideal procedures can be used to determine exact settings and ratio needed.

6

Conclusions

This thesis investigated the possibility of synthesizing PdO-USPIONs with tunable physical and magnetic properties to function as theranostic agents. Major part of the research was dedicated to studying the influence of system parameters and optimization of the setup to improve the yield and obtain nanoparticles of narrow size distribution. Subsequent work dealt with characterization of produced nanoparticles. Conclusion made regarding the research questions after extensive experimentation and analysis of the results are as follows:

1. **What operating conditions with respect to spark energy, frequency, gas flow rate are optimum for the generation of USPION & (oxidized)Pd-USPION nanoparticles?**

   High yield was observed at highest voltage. This is in agreement with the positive electrode mass loss and spark energy relation which corresponds to highest yield at 1.3 kV. High frequencies (>500Hz) showed extensive fluctuation in the voltage settings, thus production rate is restricted due to narrow usable voltage and current range. Flow rate less than 1L/min increases the nanoparticle retention inside the generator and flow rates above 2L/min resulted in larger aerosol bubble radius which leads to decrease in diffusion and collection in solution. Thus, ideal settings are V= 1.3 kV, I= 10 mA and Q= 1 L/min.

2. **How do the parameters influence size, shape and magnetic properties of PdO, USPION and PdO-USPION alloy nanoparticles?**

   Primary size of USPION was observed to be 5nm, 4nm with PdO and 5nm with PdO-USPION. The average primary particle size did not vary with difference in set-points since, the size of the particles depend majorly on the thermal properties of the element in question. Boiling point, melting point, enthalpy of vaporization and fusion associated with palladium is higher compared to Iron thus the average primary particle size is marginally smaller. However, PdO nanoparticles tend to exhibit high negative charge when dispersed in water thus resulting in extremely large agglomerates compared to USPIONs. Agglomeration size of PdO-USPION appears to increase with increase in palladium concentration in the sample.

   Shape of the nanoparticles remained predominantly spherical which is due to homogeneous nucleation during synthesis of nanoparticles in generator. Introduction of high concentration of a foreign

element, even in an alloy has been shown in the past to alter the crystal structure and thereby varying shape of the synthesized material. However, given that the yield is far too low and since palladium has been used as anode in majority of the experiments, its contribution would have been low to cause any significant variation in morphology of the composite nanoparticle.

Mass magnetization measurement showed nearly equal magnetic saturation value of 16 emu/g. However, variation in the lower % of superparamagnetic species were reported in samples with palladium via Mossbauer spectroscopy. There are far too many uncertainties associated with these measurements to give conclusive result. Most accurate results associated with magnetic properties of the synthesized PdO-USPION and USPION is given by relaxation measurements of NMR. At highest yield settings used in the system, concentration certainly increases but so does the agglomeration which has significant effect over relaxation behavior which is answered further along these questions.

3. **Can the nanoparticles generated by spark ablation mechanism be used for Magnetic thermal ablation application?**

   Based on the current understanding and limitations of the setup, probability of generating heat for thermal ablation from USPIONs and PdO-USPIONs produced with the existing set-up is remote. This is because the yield is extremely low. Moreover, low magnetization due to spin canting does not aid in obtaining or improving heating ability.

   PdO-USPIONs tend to be highly unstable due to large surface to volume ratio and agglomerations further lower the chances of heat generation via relaxation losses. If the yield is improved significantly and monodispersed inter-metallic nanoparticles are produced, then, PdO-USPIONs stand a chance to function as thermotherapy agents. None of the "Naked" USPION and PdO-USPION samples exhibited heating ability.

4. **What is effect of surfactant over the aggregation behaviour of the generated nanoparticles? Can it improve the magnetic properties leading to improved heating performance?**

   Aggregation tendency drastically reduced upon use of citric acid as surfactant which is concluded based on the observation made from TEM images and narrow size distribution from DLS. Individual primary particles were visible on TEM images. The concentration also improved even though to a small extent from 0.47 mmol/L to 2.5 mmol/L.

5. **Can PdO-USPIONs generated be used as T_1 contrast agent?**

   PdO-USPIONs function effectively as T_1 contrast agents as the r_2/r_1 ratio associated with CA capped PdO-USPIONs were 1.8 and 2.1 which corresponds to standard ratio (1-2) corresponding to T_1 contrast agents. However, large agglomeration of USPIONs and PdO-USPIONs exhibit induce large inhomogenieties locally. When water protons diffuse along these field, they experience large dephasing effect thus increasing T_2 relaxation. Use of large agglomerates in biological environment is certainly not useful. Thus, it is essential to have the nanoparticles dispersed with narrow size distribution well in the medium.

Through this research, physical and set-up limitations associated with the system were unearthed. We have very little control over physical aspects of the system but the limitations related to the set-up certainly can be over come. With increased yield, low agglomeration combined with advantages of spark ablation technology such as low contamination probability and high ease of production could offer great potential for synthesis of application specific nanoparticles.

6.1. Future Work

Since the CA coated PdO-USPION has been proven to function as T_1 contrast agent in this research, it will be useful to conduct MRI phantom studies to evaluate their performance as contrast agents in an imaging set-up. Stability of PdO-USPIONs with surfactants over long period of must be investigated time via ζ potential measurements. Large concentrations of citric acid can dissolve ultra-small nanoparticles. Hence, small quantities were investigated in the present work. It will therefore be more prudent to experiment with other hydrophilic and biocompatible surfactants.

Use of bubbling column for collection has lead to significant loss at various stages in the device. Primary focus should be to improve the yield by modifying the set-up such that no material loss is incurred. Even though primary focus of the proposed research is thermal ablation, it will be interesting to synthesize pure radioactive Pd nanoparticles via spark ablation for brachytherapy alone. Even, if they don't function as thermo-therapy agents, they could still be used for brachytherapy and imaging applications. Radioactive Palladium nanoparticles can diffuse better in the biological environment and clearance rate and efficiency will also be larger compared to traditional radioactive ^{103}Pd seeds.

Additionally, use of tube furnaces to increase size of nanoparticles can also be explored to see if larger sized particles tend to exhibit better heating behavior. Although, a potential issue associated with this approach will be generation of particles with broad size distribution.

Bibliography

[1] V. G. T. et al., "Burden of early, advanced and metastatic breast cancer in the netherlands," *BMC Cancer*, vol. 18, no. 1, p. 262, Mar. 2018.

[2] H. E. S. et al., "Survival after lumpectomy and mastectomy for early stage invasive breast cancer: The effect of age and hormone receptor status," *Cancer*, vol. 119, no. 7, pp. 1402–1411, Apr. 2013.

[3] Z. Y. et al., "Thermal ablation versus conventional regional hyperthermia has greater anti-tumor activity against melanoma in mice by upregulating cd4+ cells and enhancing il-2 secretion," *Progress in Natural Science*, vol. 19, no. 12, pp. 1699–1704, Dec. 2009.

[4] F. D. et al., "Hyperthermia: A new cancer treatment modality," *Journal of Isfahan Medical School (I.U.M.S)*, vol. 27, no. 94, pp. 190–204, Jun. 2009.

[5] E. R. et al., "Hybrid magnetic nanoparticles for targeted delivery," *Comprehensive Biomaterials*, pp. 750–771, Dec. 2017.

[6] J. T. H. et al., "A comparison of brachytherapy techniques for partial breast irradiation," *Brachytherapy*, vol. 11, no. 13, pp. 163–175, Aug. 2011.

[7] T. N. S., "The effect of operating conditions on the spark generated au-pd nanoparticles," *International Journal of Modern Physics: Conference Series*, vol. 15, no. 8, pp. 291–298, Nov. 2009.

[8] V. A., "Nanoparticle formation by means of spark discharge at atmospheric pressure," *PhD Thesis*, 2015.

[9] R. R. et al., "Temporal investigation of a fast spark discharge in chemically inert gases," *Journal of Physics D: Applied Physics*, vol. 30, pp. 1125–1134, 1997.

[10] F. J., "Scalable spark ablation synthesis of nanoparticles: Fundamental considerations and application in textile nanofinishing," *PhD Thesis*, 2016.

[11] H. B. et al., "Enormous enhancement of van der waals forces between small silver particles," *Physical Review Letters*, vol. 48, no. 25, pp. 1734–1737, Jun. 1982.

[12] S. S. al., "Aerosol generation by spark discharge," *Journal of Aerosol Science*, vol. 19, no. 5, pp. 639–642, Oct. 1988.

[13] P. T. et al., "New developments in spark production of nanoparticles," *Advanced Powder Technology*, vol. 25, no. 1, pp. 56–70, Dec. 2014.

[14] F. J. et al., "General approach to the evolution of singlet nanoparticles from a rapidly quenched point source," *The Journal of Physical Chemistry C*, vol. 120, no. 1, pp. 621–630, Dec. 2015.

[15] K. S. et al., "Current state of atmospheric aerosol thermodynamics and mass transfer modeling: A review," *Atmosphere*, vol. 11, no. 2, p. 156, Feb. 2020.

[16] L. V. K. et al., "Theory, production and mechanism of formation of monodispersed hydrosols," *Journal of the American Chemical Society*, vol. 72, no. 11, pp. 4847–4854, Nov. 1950.

[17] D. S. A. et al., "Kinetic monte carlo simulation for homogeneous nucleation of metal nanoparticles during vapor phase synthesis," *American Institute of Chemical Engineers AIChE J*, vol. 63, no. 1, pp. 18–28, Aug. 2017.

[18] T. N. T. K. et al., "Mechanisms of nucleation and growth of nanoparticles in solution," *Chemical Reviews*, vol. 114, no. 15, pp. 7610–7630, Jul. 2014.

[19] M. A. et al., "Atomic cluster generation with an atmospheric pressure spark discharge generator," *Aerosol Science and Technology*, vol. 49, no. 10, pp. 886–894, May 2015.

[20] T. S., "Generation of nanoparticles by spark discharge," *PhD Thesis*, 2009.

[21] Z. M. R. et al., "Molecular dynamics computation of gas-phase nanoparticle sintering: A comparison with phenomenological models," *Journal of Aerosol Science*, vol. 30, no. 9, pp. 1139–1151, 1999.

[22] L. K. E. J. et al., "Energy accumulation in nanoparticle collision and coalescence processes," *Journal of Aerosol Science*, vol. 33, no. 2, pp. 357–368, 2002.

[23] M. B. O. et al., "Review of spark discharge generators for production of nanoparticle aerosols," *Aerosol Science and Technology*, vol. 46, no. 11, pp. 1256–1270, Aug. 2012.

[24] T. N. S. et al., "Generation of nanoparticles by spark discharge," *Journal of Nanoparticle Research*, vol. 11, no. 2, pp. 315–332, May 2008.

[25] F. J. et al., "Toward industrial scale synthesis of ultrapure singlet nanoparticles with controllable sizes in a continuous gas-phase process," *Scientific Reports*, vol. 5, no. 15788, Oct. 2015.

[26] H. E. et al., "The transition from spark to arc discharge and its implications with respect to nanoparticle production," *British Journal of Applied Physics*, vol. 15, no. 957, Aug. 2013.

[27] P. R. H, "Chemical engineers' handbook," in *McGraw-Hill*, 2019, p. 8.

[28] R. C. et al, "Generation of ultrafine particles by spark discharging," *Aerosol Science and Technology*, vol. 38, no. 3, pp. 228–235, Mar. 2004.

[29] J. F. L., "Electrode erosion by spark discharges. british journal of applied physics," *British Journal of Applied Physics*, vol. 1, no. 3, pp. 60–65, 1950.

[30] A. Material, "Palladium (pd) - properties, applications," *https://www.azom.com/article.aspx?ArticleID=9234*, Aug. 2013.

[31] "Thermal properties of metals, conductivity, thermal expansion, specific heat," *https://www.engineersedge.com/ propertiesofmetals.htm*,

[32] U. M. et al, "Nanoparticle formation by laser ablation," *Journal of Nanoparticle Research*, vol. 4, no. 6, pp. 499–509, Dec. 2002.

[33] F. J. et al., "Internally mixed nanoparticles from oscillatory spark ablation between electrodes of different materials," *Aerosol Science and Technology*, vol. 52, no. 5, pp. 505–514, Feb. 2018.

[34] S. A., "Industrial internship report," *VS Particle*, 2017.

[35] G. E. et al., "Bubble formation in quiescent liquids under constant flow conditions," *Chemical Engineering Science*, vol. 41, no. 1, pp. 97–105, 1986.

[36] C. A. et al., "Can bubble columns be an alternative to fibrous filters for nanoparticles collection?" *Nanofinishing of Textile Materials*, vol. 195, pp. 432–439, Nov. 2011.

[37] D. C. L., "Physics of heat generation using magnetic nanoparticles for hyperthermia," *International Journal of Hyperthermia*, vol. 29, no. 8, pp. 715–729, Oct. 2013.

[38] J. P., "Relaxivity of manganese ferrite nanoparticles," *Progress in Nuclear Magnetic Resonance Spectroscopy*, vol. 120, pp. 72–94, 2020.

[39] H. M. et al., "Design criteria of thermal seeds for magnetic fluid hyperthermia - from magnetic physics point of view, nanomaterials for magnetic and optical hyperthermia applications," *Micro and Nano Technologies*, pp. 13–39, 2019.

[40] A. E. C. et al., "Structural effects on the magnetic hyperthermia properties of iron oxide nanoparticles," *Progress in Natural Science: Materials International*, vol. 26, no. 5, pp. 440–448, Oct. 2016.

[41] N. Z. et al., "Improving the heating efficiency of iron oxide nanoparticles by tuning their shape and size," *The Journal of Physical Chemistry C*, vol. 122, no. 4, pp. 2367–2381, Jan. 2012.

[42] M. J. et al., "Inductive thermal effect of ferrite magnetic nanoparticles," *Materials*, vol. 12, no. 19, p. 3208, Sep. 2019.

[43] P. et al., "Water-soluble iron oxide nanocubes with high values of specific absorption rate for cancer cell hyperthermia treatment," *ACS Nano*, vol. 6, no. 4, pp. 080–3091, Apr. 2012.

[44] T. S. et al., "Size-dependent heating of magnetic iron oxide nanoparticles," *ACS Nano*, vol. 11, no. 7, pp. 6808–6816, Jun. 2017.

[45] D. A. et al., "Size-dependent properties of magnetic iron oxidenanocrystals," *Nanoscale*, vol. 3, no. 1, pp. 225–232, Nov. 2010.

[46] M. J. et al., "Size-dependent magnetic and inductive heating properties of fe3o4 nanoparticles: Scaling laws across the superparamagnetic size," *Phys. Chem. Chem. Phys.*, vol. 20, no. 18, pp. 12 879–12 887, Apr. 2018.

[47] H. R. et al., "Size-sorted anionic iron oxide nanomagnets as colloidal mediators for magnetic hyperthermia," *Journal of the American Chemical Society*, vol. 129, no. 9, pp. 2628–2635, Feb. 2007.

[48] J. M. et al., "Physical limits of pure superparamagnetic fe3o4 nanoparticles for a local hyperthermia agent in nanomedicine," *Applied Physics Letters*, vol. 100, no. 9, p. 092 406, Mar. 2012.

[49] S. S. C. et al., "Combining magnetic hyperthermia and dual t1/t2 mr imaging using highly versatile iron oxide nanoparticles," *Dalton Transactions*, vol. 12, no. 48, pp. 3883–3892, Feb. 2019.

[50] X. L. e. a. Liu, "Optimization of surface coating on fe3o4 nanoparticles for high performance magnetic hyperthermia agents," *Journal of Material Chemistry*, vol. 17, no. 22, pp. 8235–8244, Mar. 2012.

[51] S. H. et al., "Tunable high aspect ratio iron oxide nanorods for enhanced hyperthermia," *J. Phys. Chem. C*, vol. 120, no. 18, pp. 10 086–10 093, Apr. 2016.

[52] K. A. et al., "Tuning the magnetic properties of nanoparticles," *International Journal of Molecular Sciences*, vol. 14, no. 8, pp. 15 977–16 009, Jul. 2013.

[53] S. A. et al., "Coxfe3–xo4 nanocubes for theranostic applications: Effect of cobalt content and particle size," *Chemistry of Materials*, vol. 28, no. 6, pp. 1769–1780, Feb. 2016.

[54] N. e. a. Spaldin, "Magnetic materials: Fundamentals and applications," *Cambridge University Press: Cambridge*, 2010.

[55] M. J. et al., "Magnetic and hyperthermia properties of coxfe3-xo4 nanoparticles synthesized via cation exchange," *Chemistry of Materials*, vol. 8, no. 5, p. 056 725, Jan. 2018.

[56] M. Y. et al., "Precisely tuning the contrast properties of znxfe3-xo4 nanoparticles in magnetic resonance imaging by controlling their doping contents and sizes," *Chemistry of Materials*, vol. 31, no. 18, pp. 7255–7264, Aug. 2019.

[57] J. J. et al., "Critical enhancements of mri contrast and hyperthermic effects by dopant-controlled magnetic nanoparticles," *Angewandte Chemie*, vol. 48, no. 7, pp. 1234–1238, Feb. 2009.

[58] J. B. et al., "Spin echo magnetic resonance imaging. journal of magnetic resonance imaging," *International Journal of Pharmaceutics*, vol. 37, no. 4, pp. 805–817, Mar. 2013.

[59] K. G. et al., "Recent advances in superparamagnetic iron oxide nanoparticles (spions) for in vitro and in vivo cancer nanotheranostics," *International Journal of Pharmaceutics*, vol. 496, no. 2, pp. 191–218, Dec. 2015.

[60] P. J. L. et al., "Medical imaging signals and systems: Second edition," *Pearson Prentice Hall Bioengineering*, 2005.

[61] L.-R. L. M., "Basic mr relaxation mechanisms and contrast agent design," *Journal of Magnetic Resonance Imaging*, vol. 42, no. 3, pp. 545–565, May 2015.

[62] L. R. et al., "Paramagnetic metal complexes as water proton relaxation agents for nmr imaging: Theory and design," *Chemical Reviews*, vol. 87, no. 5, pp. 901–927, Oct. 1987.

[63] K. B. et al., "Large-scale synthesis of uniform and extremely small-sized iron oxide nanoparticles for high-resolutiont1magnetic resonance imaging contrast agents," *Journal of the American Chemical Society*, vol. 133, no. 32, pp. 12 624–12 631, Jun. 2011.

[64] Z. L. et al., "Ultrasmall water-soluble metal-iron oxide nanoparticles as t1-weighted contrast agents for magnetic resonance imaging," *Physical Chemistry Chemical Physics*, vol. 14, no. 8, p. 2631, 2012.

[65] B. Y. et al., "Magnetic iron oxide nanoparticles as t1 contrast agents for magnetic resonance imaging," *Journal of Materials Chemistry C*, vol. 6, no. 6, pp. 1280–1290, Jan. 2018.

[66] I. M. et al., "Silica-coated super-paramagnetic iron oxide nanoparticles (spionps): A new type contrast agent of t1 magnetic resonance imaging (mri)," *Journal of Materials Chemistry B*, vol. 26, no. 3, pp. 5172–5181, May 2015.

[67] T. D., "Optimization of spark ablation setup: Analysis of produced iron-oxide nanoparticles in a water-based liquid," *BSc thesis*, 2020.

[68] W. A. et al., "Functionalization strategies and dendronization of iron oxide nanoparticles," *Nanotechnology Review*, vol. 4, no. 6, pp. 581–293, Mar. 2015.

[69] "Zeta potential - an introduction in 30 minutes," *Malvern Instruments Limited*, 2015.

[70] K. D., "Stabilization of colloids," *https://www.substech.com/dokuwiki/doku.php?id=stabilization*$_o f_c olloids$, Dec. 2013.

[71] M. R. et al., "From colloidal particles to supported catalysts: A comprehensive study of palladium oxide hydrosols deposited on alumina," in *Preparation of Catalysts VII*, 1998, pp. 49–51.

[72] G. S. et al., "Synthesis of carboxyl-modified fe3o4@sio2 nanoparticles and their utilization for the remediation of cadmium and nickel from aqueous solution," *The Chilean Chemical Society*, vol. 62, no. 3, pp. 3588–3592, Sep. 2017.

[73] C. E. et al., "Citrate capped superparamagnetic iron oxide nanoparticles used for hyperthermia therapy," *Biomedical Science and Engineering*, vol. 5, pp. 715–719, Dec. 2012.

[74] E. ToolBox, "Density of aqueous solutions of organic acids," *https://www.engineeringtoolbox.com/density-aqueous-solution-formic-lactic-oxalic-acetic-citric-acid-concentration-d*$_1$953.$html$, 2017.

[75] S. A. I. et al., "Modelling of the thermophysical properties of citric acid aqueous solutions. density and viscosity," *Annals, Food Science and Technology*, vol. 15, no. 1, pp. 193–202, Apr. 2014.

[76] C. H. et al., "Hydrodynamics and mass transfer in bubble column: Influence of liquid phase surface tension," *Chemical Engineering Science*, vol. 62, no. 24, pp. 7378–7390, Dec. 2007.

[77] D. A. M. et al., “Simple rapid stabilization method through citric acid modification for magnetite nanoparticles,” *Scientific Reports*, vol. 10, no. 10793, Jul. 2020.

[78] S. J., “Dynamic light scattering: A practical guide and applications in biomedical sciences,” *Biophysical Reviews*, vol. 8, no. 4, pp. 409–427, 2016.

[79] S. Pennycook, “Scanning transmission electron microscopy for nanostructure characterization,” *Biophysical Reviews*, vol. 2, p. 6, 2006.

[80] B. B. et al., “Concepts, instrumentation and techniques in inductive couples plasma-optical emission spectrometry,” *PerkinElmer*, 2004.

[81] Manual, “Scanning electron microscope a to z: Basic knowledge for using the sem,” *JOEL Ltd*,

[82] “Versalab user manual,” *Quantum Design*, 2004.

[83] C. S., “Functional mri : Methods and applications,” *University of Nottingham, PhD Thesis*, 1997.

[84] B. B. et al., “Oxidation, reduction, and reactivity of supported pd nanoparticles: Mechanism and microkinetics,” *Journal of Physical Chemistry C*, vol. 111, no. 2, pp. 938–949, Dec. 2006.

[85] B. A. L. et al., “In situ formation of surface and bulk oxides in small palladium nanoparticles,” *Chemical Communications*, vol. 86, no. 56, pp. 13 097–13 100, Sep. 2020.

[86] Z. S. L. et al., “Photoemission and mossbauer effect studies of sputter-deposited fe-pd alloys,” *Basic Solid State Physics*, vol. 182, no. 2, pp. 421–427, Apr. 1994.

A

Calibrations and Calculations

A.1. Calibration lines of Fe (All emission wavelengths)

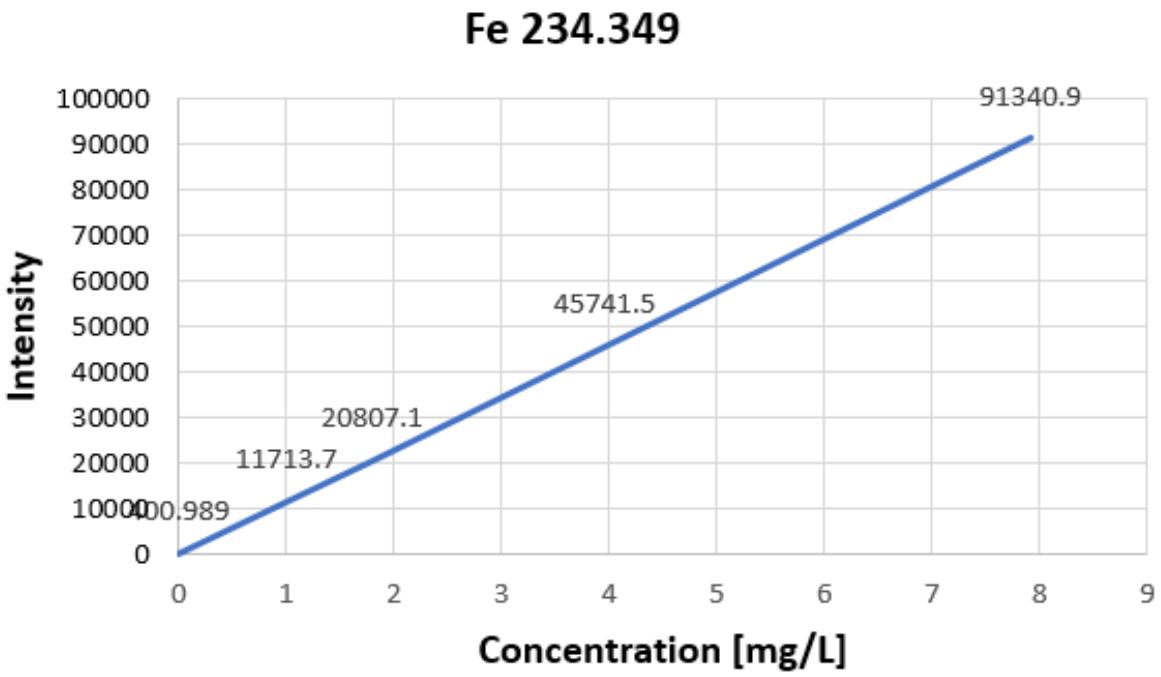

Figure A.1: Fe234.349 calibration

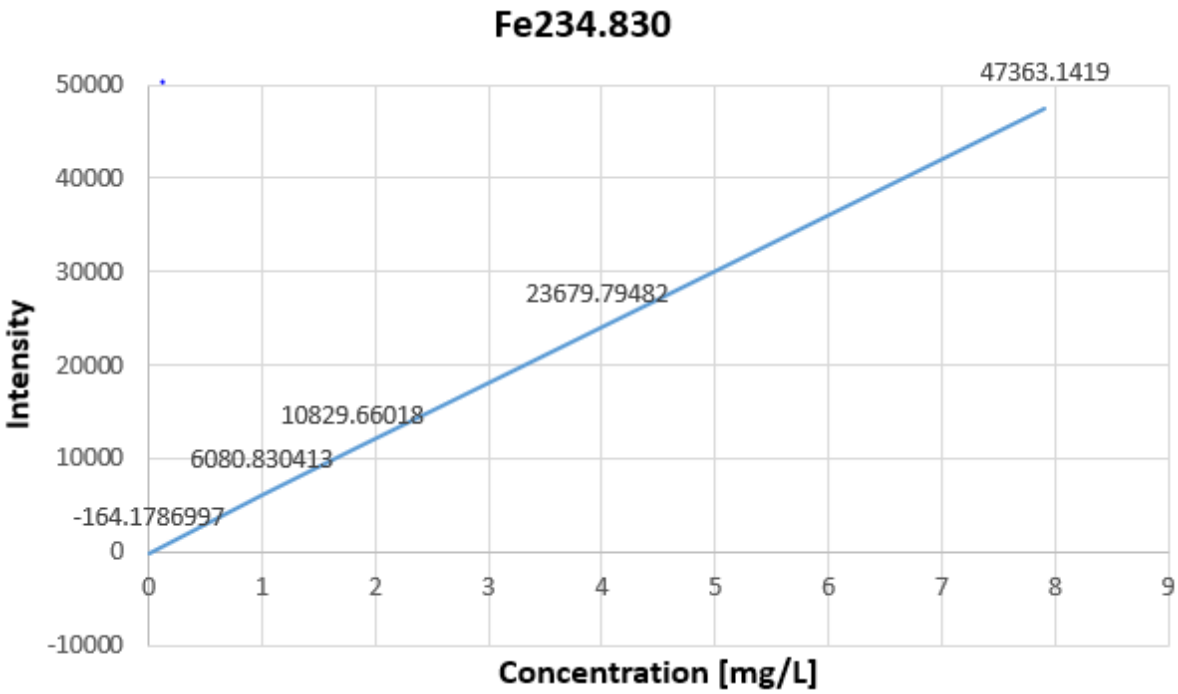

Figure A.2: Fe234.830 calibration

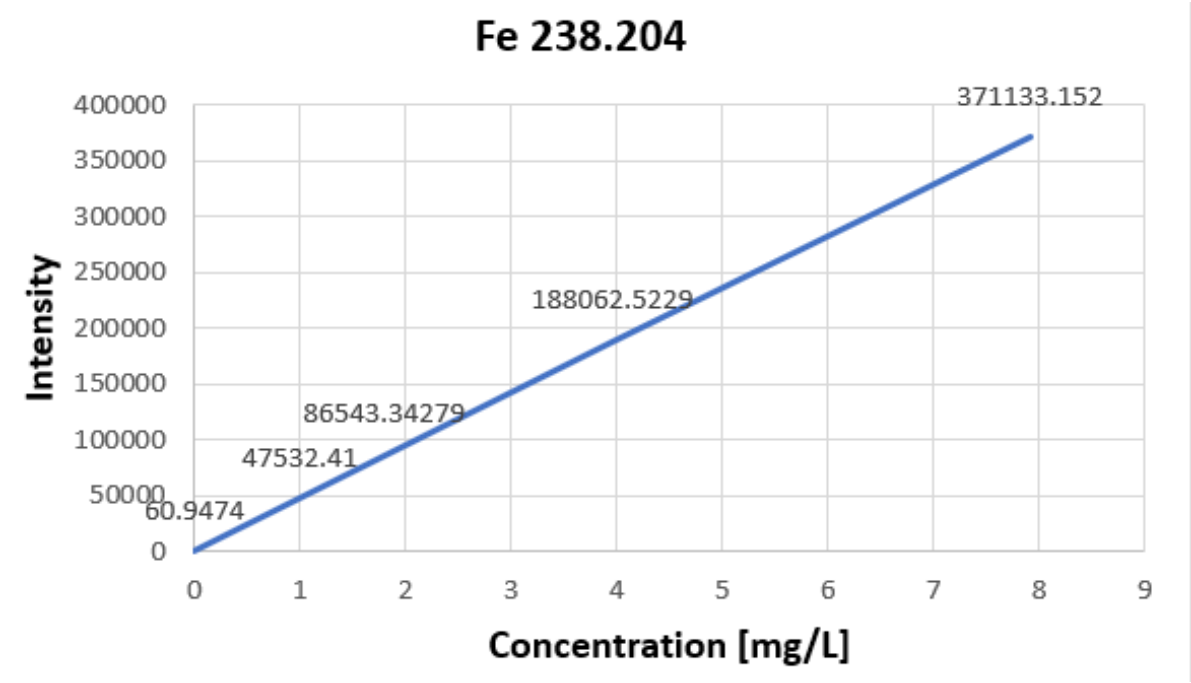

Figure A.3: Fe238.204 calibration

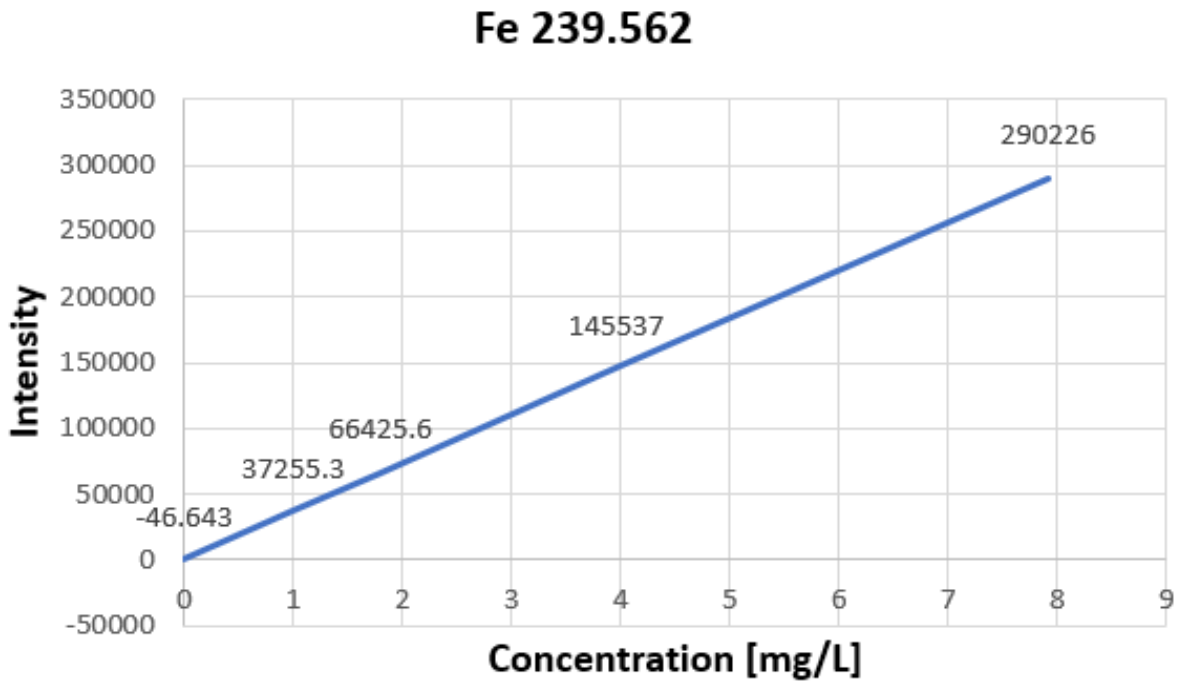

Figure A.4: Fe239.562 calibration

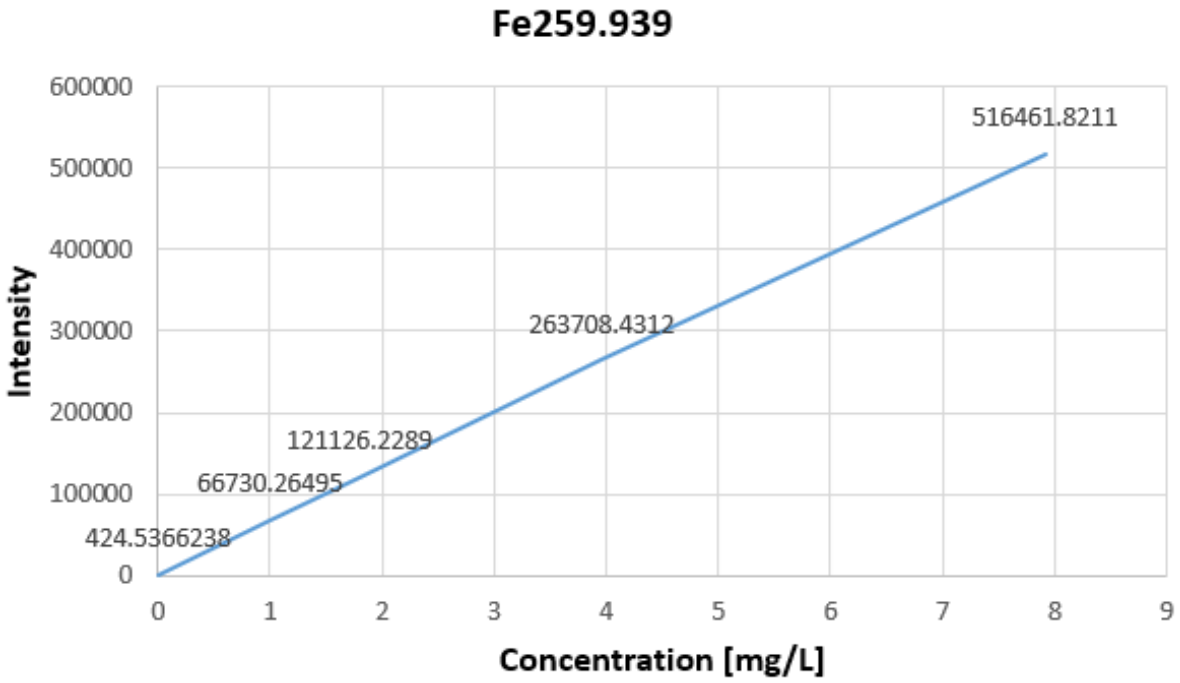

Figure A.5: Fe259.939 calibration

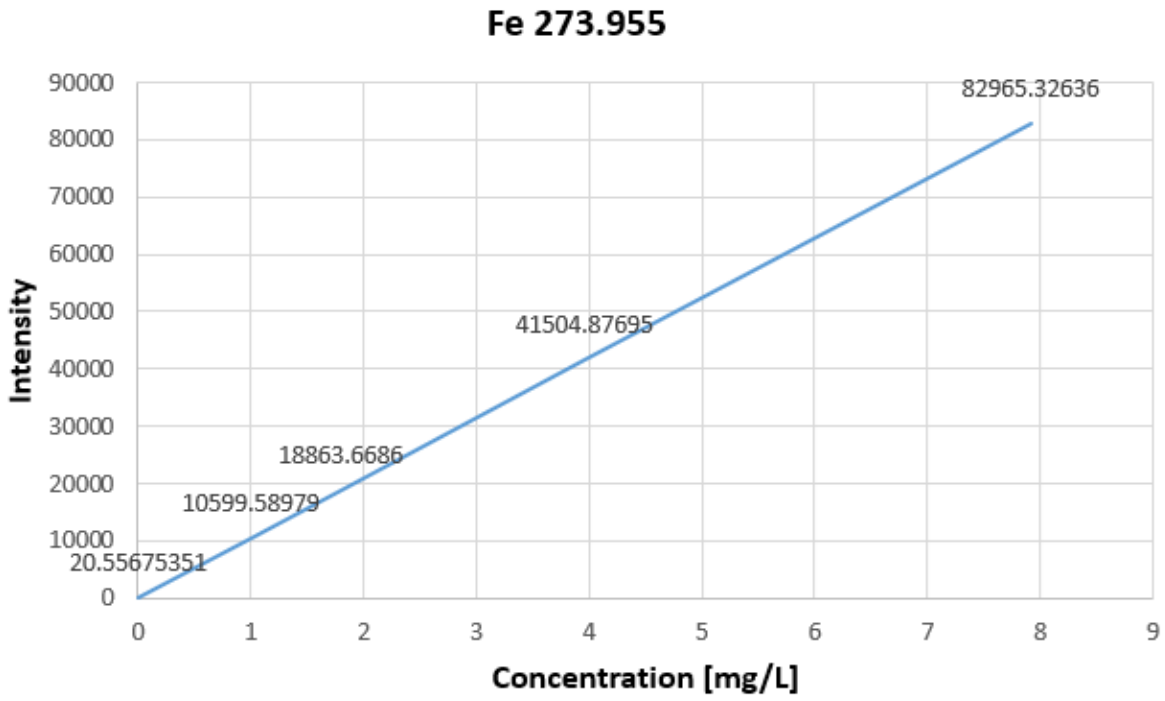

Figure A.6: Fe273.955 calibration

A.2. Calibration lines of Pd (All emission wavelengths)

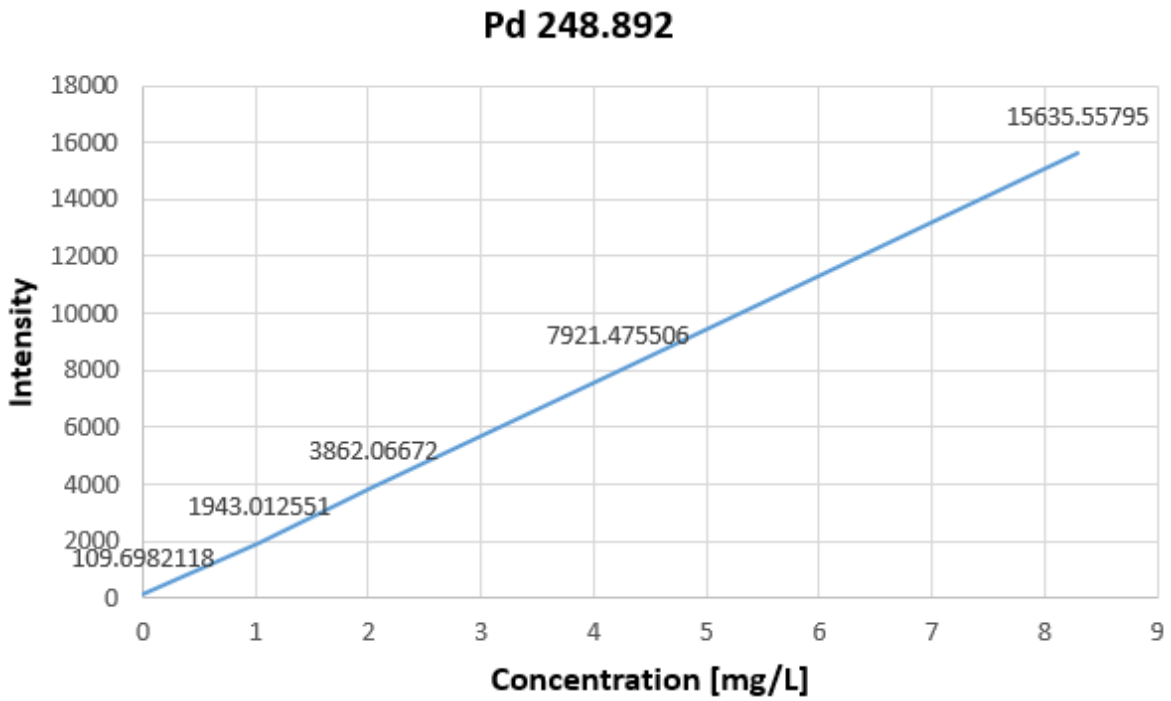

Figure A.7: Pd248.892 calibration

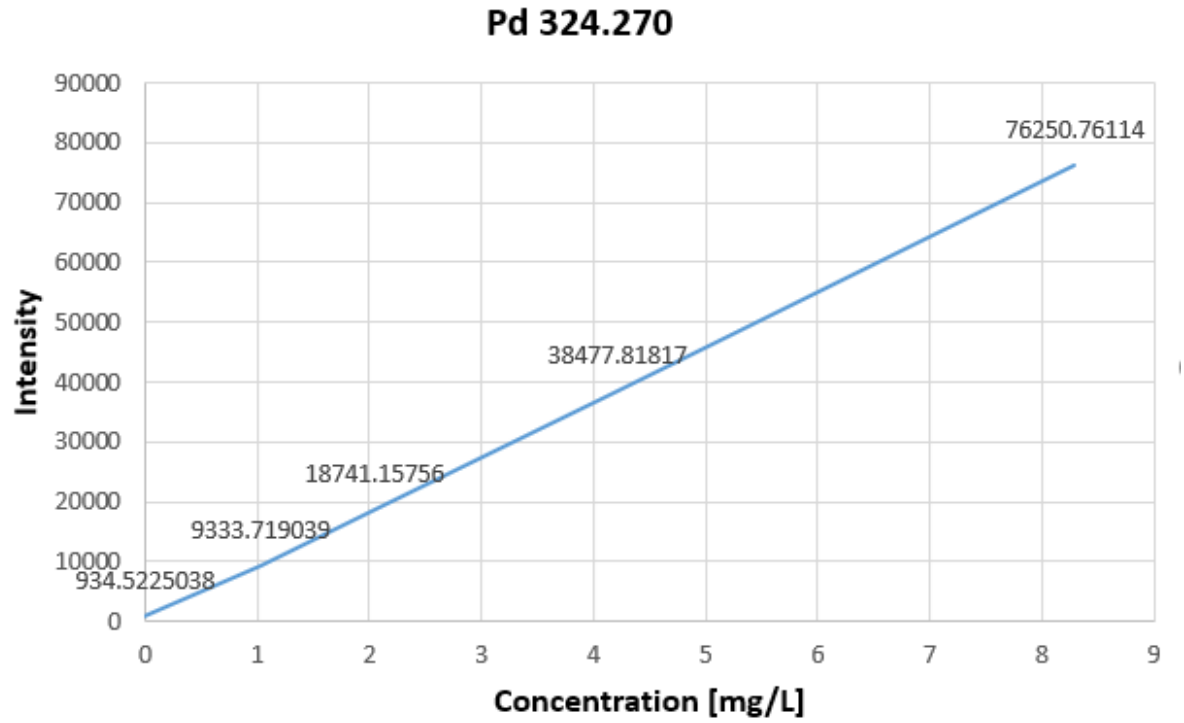

Figure A.8: Pd324.270 calibration

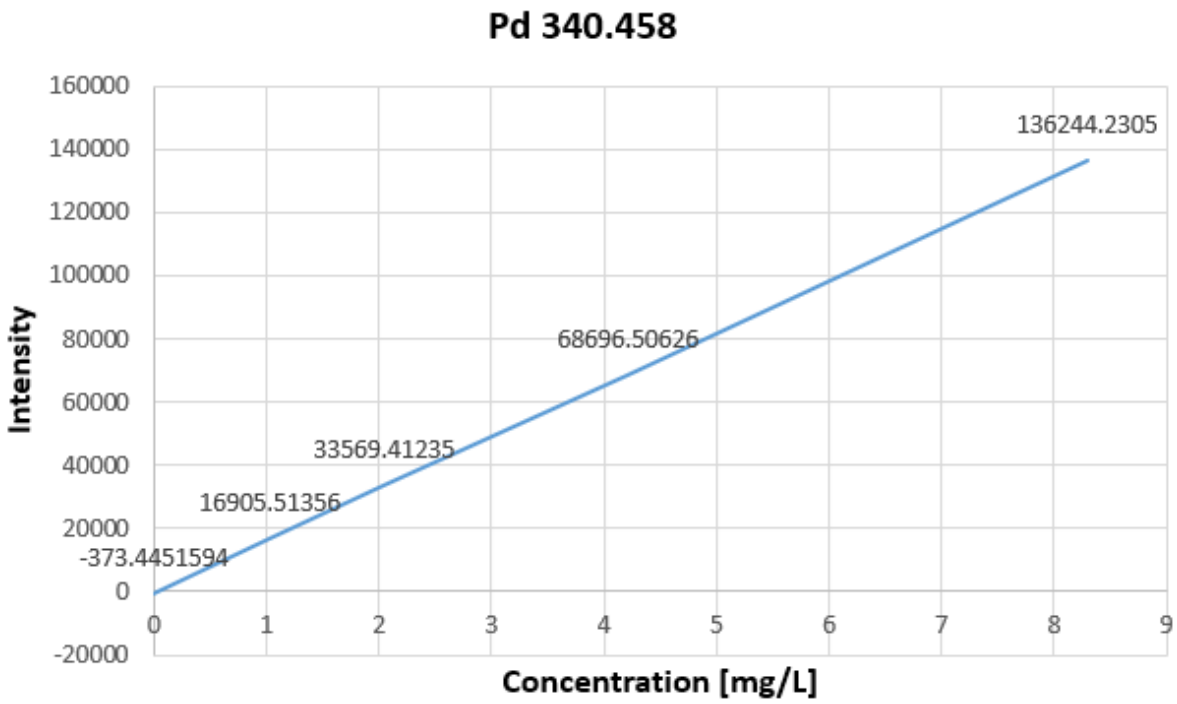

Figure A.9: Pd340.458 calibration

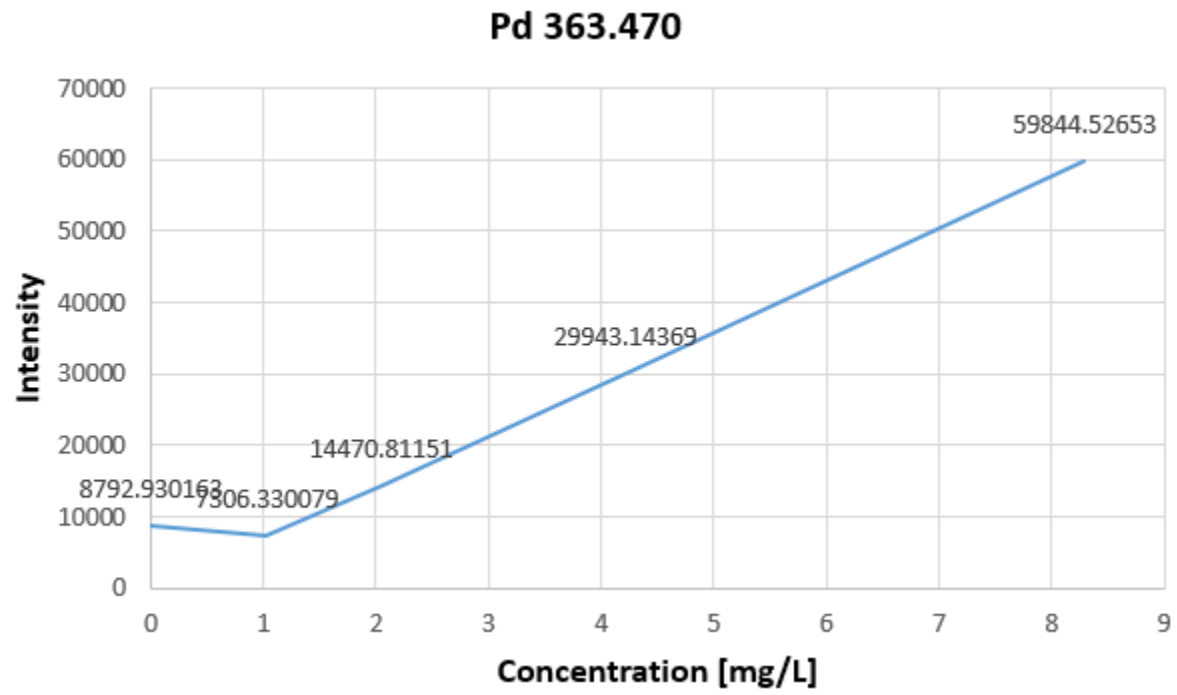

Figure A.10: Pd363.470 calibration

A.3. Concentration and pH Calculations of Citric Acid

A.3.1. Citric acid solution for experiment 32

0.5% w/v of citric acid solution was prepared in 50 ml of Milli-q water. Formula of citric acid: $C_6H_8O_7$ Molecular Weight: 192.124 g/mol

$$Concentration[mM] = \frac{Mass[g]}{M.Wt[g/mol] * Vol[ml]} = \frac{0.25}{[192.124]X[50]} \tag{A.1}$$

$$Concentration = 26mMin50mlofMQwater \tag{A.2}$$

To calculate pH, only ka_1 of citric acid is used ka_1 of citric acid = 7.1x 10^{-4}

$$ka_1 = \frac{x^2}{C-x} \tag{A.3}$$

$$7.1x10^{-4} = \frac{x^2}{26mM-x} \tag{A.4}$$

On solving the quadratic equation:

$$X = +0.003956 \tag{A.5}$$

$$X = -0.004666 \tag{A.6}$$

pKa can't be negative so the negative solution is discarded

$$pH = -log(0.003956) \tag{A.7}$$

$$pH = 2.4 \tag{A.8}$$

A.3.2. Citric acid solution for experiment 33

10 ml of citric acid solution with concentration of 0.5 g/ml is prepared. Of which, 1.5 ml is added to 50ml MQ water in the bubbling column. Approximately 0.75g of citric acid will be present in 1.5 ml of solution.

$$Concentration[mM] = \frac{Mass[g]}{M.Wt[g/mol] * Vol[ml]} = \frac{0.75}{[192.124]X[51.5]} \tag{A.9}$$

$$Concentration = 75.8mMin51.5mlofMQwater \tag{A.10}$$

To calculate pH, only ka_1 of citric acid is used ka_1 of citric acid = 7.1x 10^{-4}

$$ka_1 = \frac{x^2}{C-x} \tag{A.11}$$

$$7.1x10^{-4} = \frac{x^2}{75.8mM-x} \tag{A.12}$$

On solving the quadratic equation:

$$X = +0.006989 \tag{A.13}$$

$$X = -0.0076996 \tag{A.14}$$

pKa can't be negative so the negative solution is discarded

$$pH = -log(0.006989) \tag{A.15}$$

$$pH = 2.15 \tag{A.16}$$

A.4. NMR Calculations

A.4.1. Controls

Water

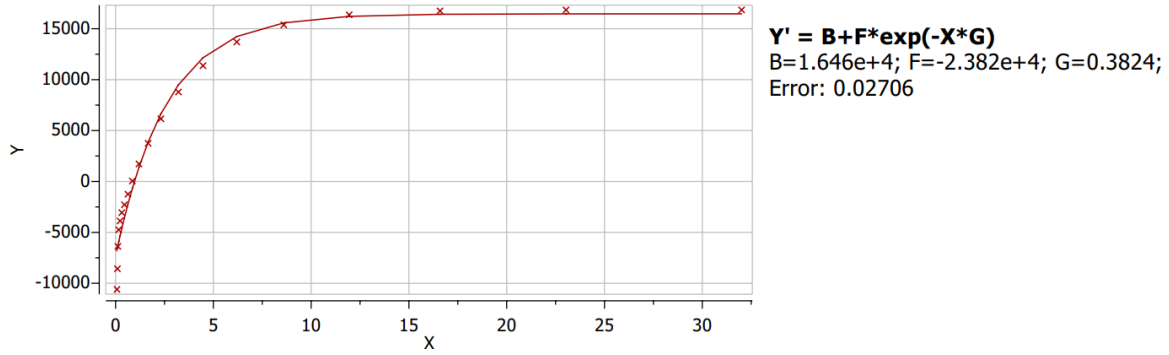

Figure A.11: T_1 relaxation of water

$R_1 = 0.3824$ $R_2 = 0.3906$

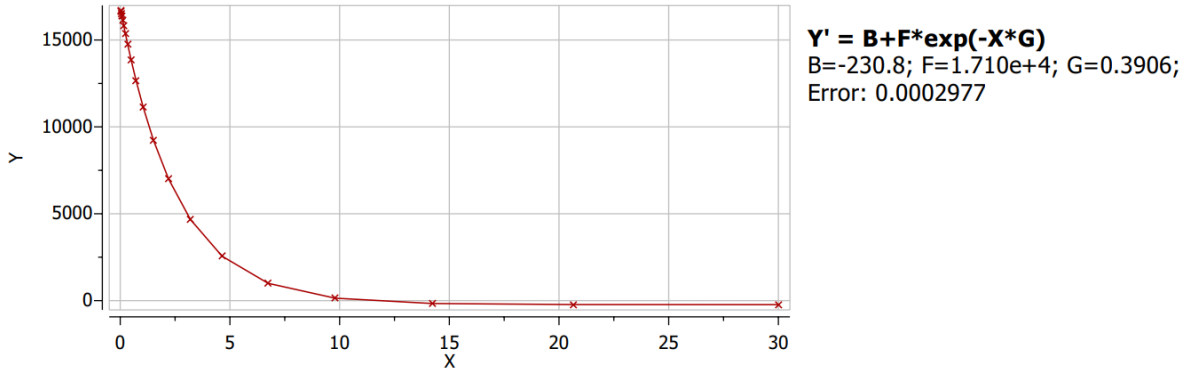

Figure A.12: T_2 relaxation of water

Xanthan

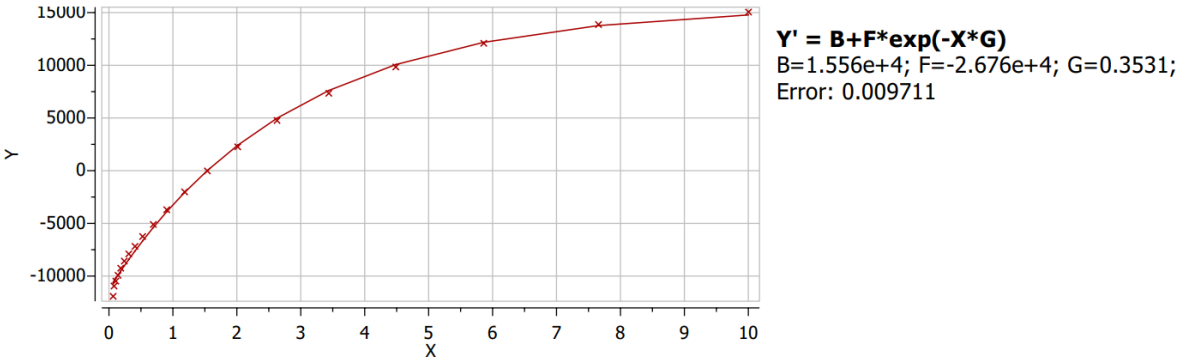

Figure A.13: T_1 relaxation of Xanthan

$R_1 = 0.3531$ $R_2 = 1.132$

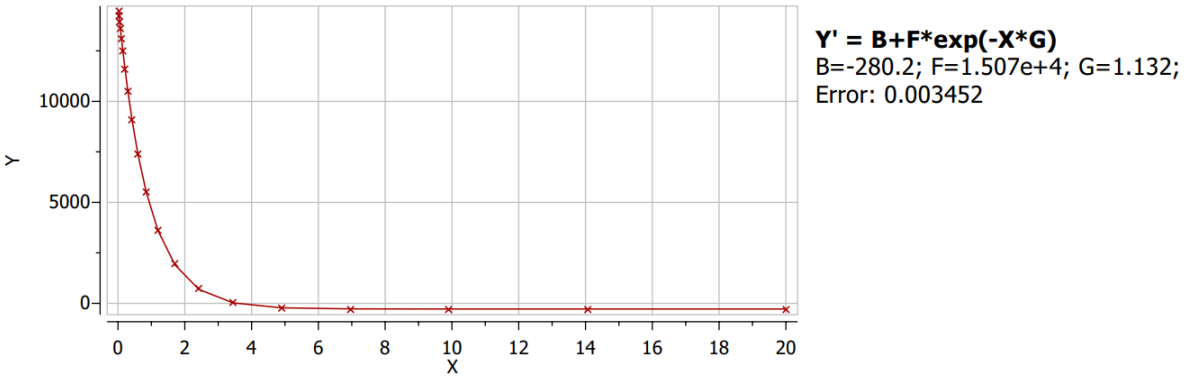

Figure A.14: T_2 relaxation of Xanthan

A.4.2. Relaxation measurements of E30

Sample - "Naked" PdO-USPION with Fe as cathode an Pd as Anode Concentration (C) = 0.469 mmol/L

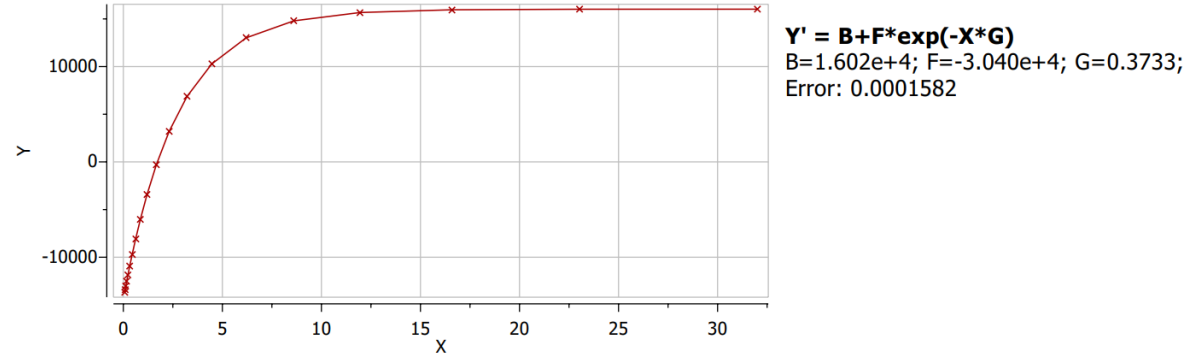

Figure A.15: E30-T_1

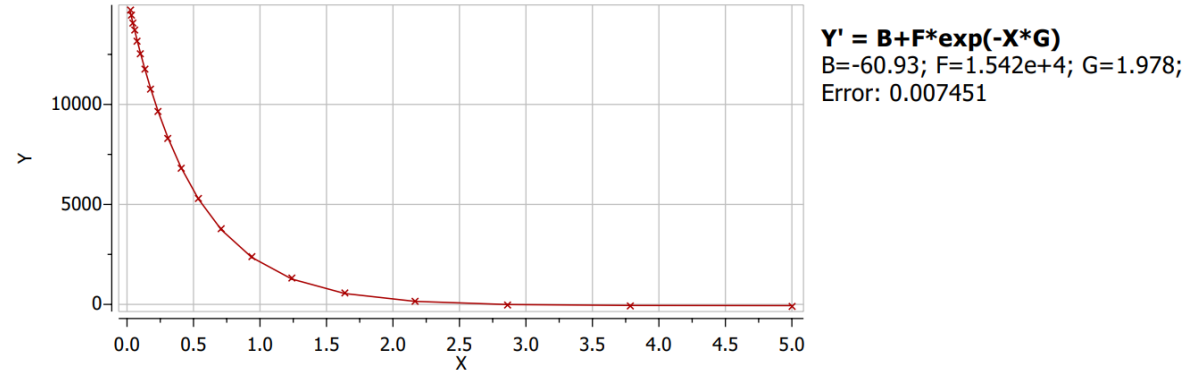

Figure A.16: E30-T_2

$$r_1 = \frac{R_{E30,1} - R_{Xanthan,1}}{C} \tag{A.17}$$

$$r_1 = \frac{0.3733 - 0.3531}{0.469} \tag{A.18}$$

$$r_1 = 0.043 L/mmol.s \tag{A.19}$$

$$r_2 = \frac{R_{E30,2} - R_{Xanthan,2}}{C} \tag{A.20}$$

$$r_2 = \frac{1.978 - 1.132}{0.469} \tag{A.21}$$

$$r_2 = 1.8 L/mmol.s \tag{A.22}$$

$$\frac{r_2}{r_1} = 41.86 \tag{A.23}$$

A.4.3. Relaxation measurements of E31

Sample - "Naked" PdO-USPION with Fe as Anode an Pd as Cathode Concentration (C) = 0.6 mmol/L

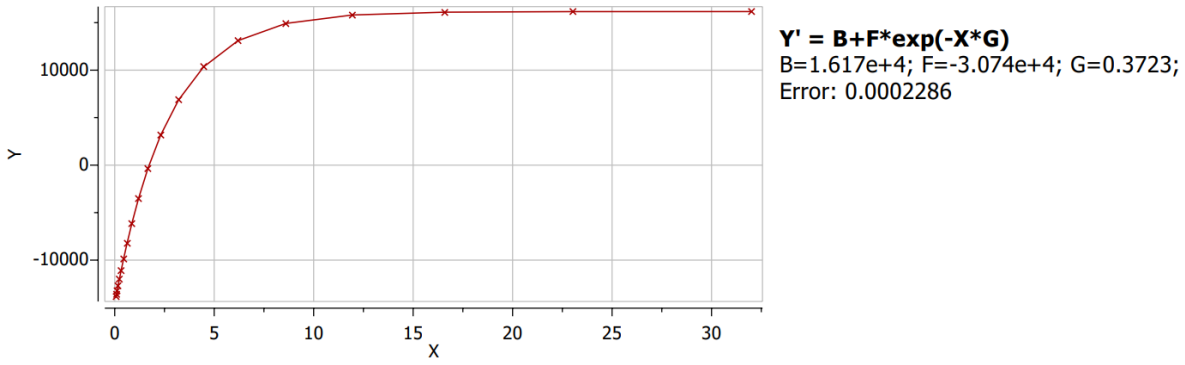

Figure A.17: E31-T_1

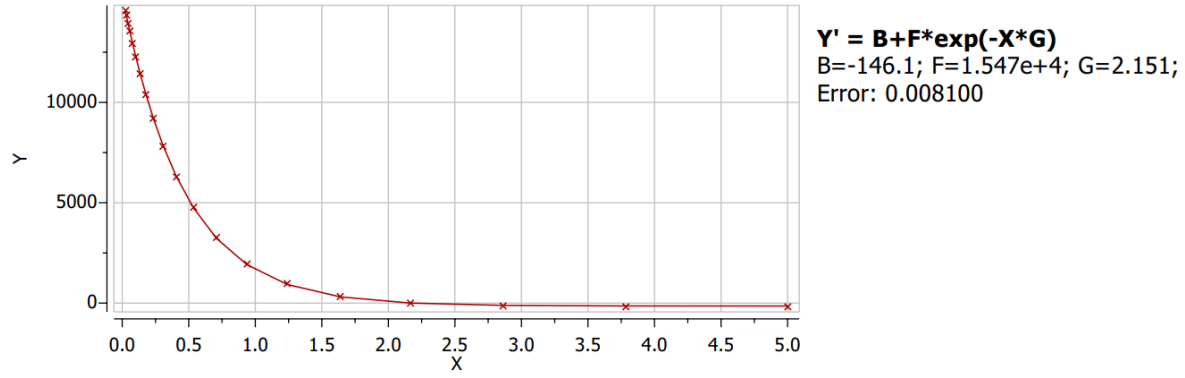

Figure A.18: E31-T_2

$$r_1 = \frac{R_{E31,1} - R_{Xanthan,1}}{C} \tag{A.24}$$

$$r_1 = \frac{0.3723 - 0.3531}{0.6} \tag{A.25}$$

$$r_1 = 0.0335 L/mmol.s \tag{A.26}$$

$$r_2 = \frac{R_{E31,2} - R_{Xanthan,2}}{C} \tag{A.27}$$

$$r_2 = \frac{2.151 - 1.132}{0.6} \tag{A.28}$$

$$r_2 = 1.69 L/mmol.s \tag{A.29}$$

$$\frac{r_2}{r_1} = 50.44 \tag{A.30}$$

A.4.4. Relaxation measurements of E32

Sample - 26mM CA coated PdO-USPION with Fe as cathode an Pd as Anode Concentration (C) = 0.702 mmol/L

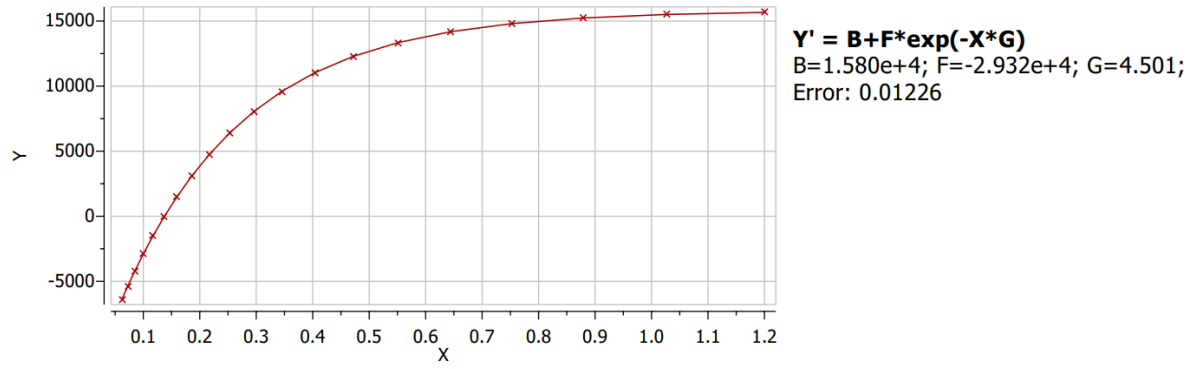

Figure A.19: E32-T_1

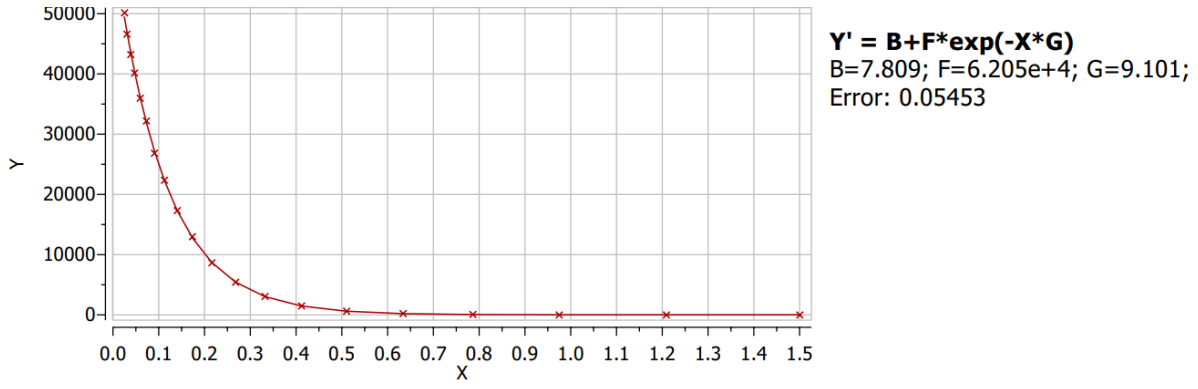

Figure A.20: E32-T_2

$$r_1 = \frac{R_{E32,1} - R_{Water,1}}{C} \tag{A.31}$$

$$r_1 = \frac{4.501 - 0.3824}{0.702} \tag{A.32}$$

$$r_1 = 5.86 L/mmol.s \tag{A.33}$$

$$r_2 = \frac{R_{E32,2} - R_{Water,2}}{C} \tag{A.34}$$

$$r_2 = \frac{9.101 - 0.3906}{0.702} \tag{A.35}$$

$$r_2 = 12.40 L/mmol.s \tag{A.36}$$

$$\frac{r_2}{r_1} = 2.1 \tag{A.37}$$

A.4.5. Relaxation measurements of E33

Sample - 75.8mM CA coated PdO-USPION with Fe as cathode an Pd as Anode Concentration (C) = 2.5 mmol/L

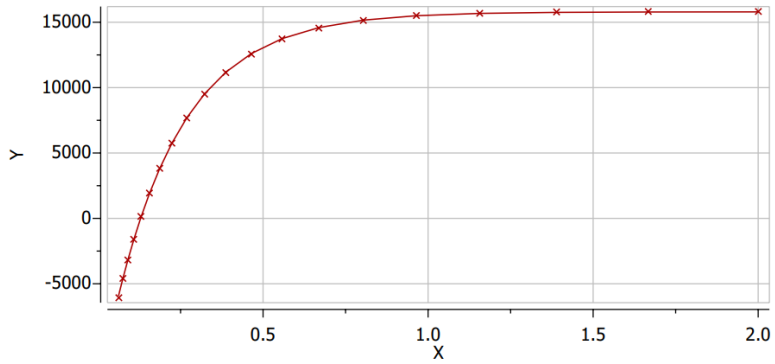

Figure A.21: E33-T_1

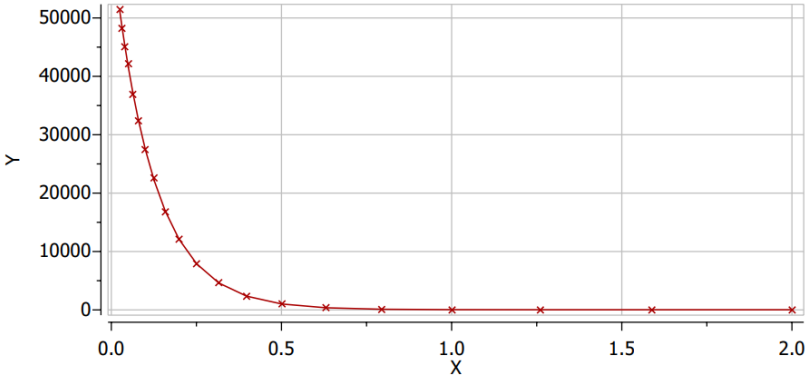

Figure A.22: E33-T_2

$$r_1 = \frac{R_{E33,1} - R_{Water,1}}{C} \tag{A.38}$$

$$r_1 = \frac{4.767 - 0.3824}{0.702} \tag{A.39}$$

$$r_1 = 1.75 L/mmol.s \tag{A.40}$$

$$r_2 = \frac{R_{E33,2} - R_{Water,2}}{C} \tag{A.41}$$

$$r_2 = \frac{8.289 - 0.3906}{0.702} \tag{A.42}$$

$$r_2 = 3.1593 L/mmol.s \tag{A.43}$$

$$\frac{r_2}{r_1} = 1.8 \tag{A.44}$$